Aus dem Institut für Medizinische Mikrobiologie und Krankenhaushygiene
(Geschäftsführender Direktor: Prof. Dr. Michael Lohoff)
des Fachbereichs Medizin der Philipps-Universität Marburg

Die Bedeutung des Lymphozyten-Transkriptionsfaktors Interferon regulierender Faktor 4 in der Entstehung von präB Zell Leukämien der Maus

Kumulative Dissertation zur Erlangung des Doktorgrades der Medizin
(Dr. med.)

Dem Fachbereich Medizin
Der Philipps-Universität Marburg
Vorgelegt von

Dennis Das Gupta
Aus Tönisvorst

Marburg, 2022

Angenommen vom Fachbereich Medizin der Philipps-Universität Marburg am 29.09.2022

Gedruckt mit Genehmigung des Fachbereiches

Dekanin: Prof. Dr. Denise Hilfiker-Kleiner

Referent: Prof. Dr. Michael Lohoff

Korreferent: Prof. Dr. Oliver Rick

Für die Ungewissheit

1. Inhaltsverzeichnis

2. Abkürzungsverzeichnis

AICE	AP-1-IRF4 *composite elements*
AID	*activation induced cytidine deamidase*
AP-1	*activator family member 1*
BATF	*basic leucine zipper transctiprion factor 1*
BCP-ALL	*B cell progenitor acute lymphoblastic leukemia*
BZR	B-Zell Rezeptor
CAE	Chloracetat Esterase
CD	*cluster of differentiation*
CLP	*common lymphoid progenitor*
CRLF2	*cytokine receptor like factor 2*
CTLA4	*cytotoxic T-lymphocyte associated protein 4*
CXCL12	CXC-Motiv Chemokin 12
CXCR4	CXC-Motiv Chemokin Rezeptor 4
eGFP	*enhanced green fluorescent protein*
FoxP3	*forkhead box P3*
Gclc	Glutamat-Cystein-Ligase
GOF	*gain-of-function*
Ig	Immunglobulin
IKZF1	*IKAROS family zinc finger 1*
IL-7	Interleukin 7
IL-7R	Interleukin 7 Rezeptor
IPEX	*Immune dysregulation, polyendocrinopathy, enteropathy, and X-linked inheritance*
IRF4	Interferon-regulierender Faktor 4
JAK	Januskinase
KO	*knock-out*
LPS	Lipopolysaccharid
MACS	*magnetic activated cell sorting*
MSZ	mesenchymale Stromazelle
NK-Zellen	*natural-killer* Zellen
PAX5	*paired box 5*
Ph^+	Philadelphia-Chromosom positiv
pMSCV	Murines Stammzellvirus
RAG1/2	*recombination activating genes 1/2*
SPF	*specific pathogen free*
STAT	*signal transducer of activated T cells*
Teff	T Effektor Zelle
TF	Transkriptionsfaktor
TLSP	*thymic stromal lymphopoetin*
Treg	T regulatorische Zelle
TSLPR	*thymic stromal lymphopoetin* Rezeptor
VpreB	*V-set preB cell surrogate light chain*
wt	Wildtyp
X-SCID	*X-linked severe combined immunodeficiency disease*
ZNS	zentrales Nervensystem

3. Einleitung

Das Immunsystem der Wirbeltiere kann eingeteilt werden in einen angeborenen und einen adaptiven Schenkel. Während es die Rolle des angeborenen Immunsystems ist, die Erkennung konservierter Zielstrukturen auf körperfremden biologischen Entitäten wie Viren und Bakterien zu erkennen und eine breit gerichtete erste Immunantwort zu generieren, dient das adaptive System dazu, mit Hilfe spezifischer Rezeptoren eine im Kontakt mit dem Fremd-Agens fein adjustierte und genaue Immunantwort zu generieren. Wichtiger Bestandteil dieses Schenkels des Immunsystems ist zudem die Etablierung eines über die Dauer bestehenden immunologischen Gedächtnisses. Auch wenn neuere Befunde eine engere Verzahnung beider Schenkel darstellen, behält das ursprüngliche dichotome Modell eine Bedeutung in der Erklärung von Immunantworten.

3.1 B-Zell Entwicklung

Zelluläre Akteure des adaptiven Immunsystems sind die B- und T-Lymphozyten, die sich aus gemeinsamen lymphoiden Vorläufer-(=„*Progenitor*“-) Zellen im Knochenmark herausbilden. Während die T-Zell Reifung und Selektion nach der gemeinsamen Vorentwicklung in einem spezialisierten Organ, dem Thymus, stattfindet, vollzieht sich die Reifung und Selektion der B-Zellen fast vollständig im Knochenmark. Während T Zellen als Träger einer zellvermittelten Immunität wirken, besteht die Hauptaufgabe der B Zellen in der Produktion von antigen-spezifischen löslichen Antikörpern.

Das Knochenmark besteht aus einem losen Verband aus knochen-, knorpel- und gefäßbildenden Stromazellen, zwischen denen Nester an hämatopoietischen Zellen verschiedener Entwicklungsreihen eingepasst sind. Dort differenzieren sich Abkömmlinge langlebiger hämatopoetischer Stammzellen früh in myeloisch- oder lymphatisch-determinierte Progenitorzellen. Mit jedem Schritt der Differenzierung verliert die jeweilige Zelle dabei Stammzelleigenschaften.(Hardy and Hayakawa, 2001) Lange Zeit konnte keine eindeutige Nische der B-Zell Entwicklung definiert werden. Die Verwendung von Reporter-Mäusen, die Fluoreszenzmarker unter dem Promoter zentraler Differenzierungsmarker exprimieren, gemeinsam mit der Entwicklung einer Technik zur Aufarbeitung von nicht de-kalzifizierten Knochenmarkschnitten (Kawamoto filmtechnik) führte zur Identifizierung von Chemokin $CXCL12^{+}$ Interleukin (IL-)7^{+} mesenchymalen Stromazellen (MSZs) als zentrale

Nischenbildner der B-Zell Entwicklung.(Fistonich et al., 2018; Kawamoto, 2003; Lim et al., 2017; Tokoyoda et al., 2004) Diese diffus über die gesamt Knochenmarksarchitektur verteilten MSZs sind entscheidend für die B-Zell Entwicklung, indem sie den Wachstumsfaktor IL-7 produzieren.(Barata et al., 2019; Fistonich et al., 2018; Hara et al., 2012)

Die Entwicklung von B-Zellen im Knochenmark verläuft in klar definierten, sequentiellen Entwicklungsstadien, die eine feine Balance aus Zellteilung und Differenzierung bewirken.(Hardy and Hayakawa, 2001) Die Komplexität der einzelnen Entwicklungsschritte ergibt sich dabei aus einer genetischen Besonderheit der Lymphozyten: während die Grundstruktur der Gene für die zentralen Immunrezeptoren des T-Zell- und des B-Zell-Rezeptors (BZR) in der Keimbahn kodiert ist, führen Rekombinationen auf genomischer Ebene während der Differenzierung zur Etablierung eines umfassenden Spektrums somatisch variabler Rezeptorketten auf der Oberfläche reifer Lymphozyten. Gegenüber dem klaren evolutionären Vorteil dieses statistischen Präventionsprinzips steht die Gefahr der Generierung eines Rezeptors, der körpereigene Strukturen erkennt – mit der Gefahr von Autoimmunerkrankungen. Um letztere Gefahr einzuschränken, ist die B-Zellentwicklung physiologischerweise eine strikt reglementierte Entwicklungsabfolge, bei der autoimmune Rezeptoren typischerweise eliminiert werden.

Die Stadien der B-Zell Entwicklung wurden anhand von Oberflächenmarkern untersucht und definiert.(Hardy et al., 1991; Osmond et al., 1998) Auch wenn bis heute keine gänzlich einheitliche Nomenklatur der Stadien besteht, ist die Klassifikation, die Hardy und Kollegen definierten, eine häufig verwendete Einteilung.(Hardy and Hayakawa, 2001; Hardy et al., 1991) Die genannte, auch in dieser Arbeit verwendete Klassifikation, basiert auf der Stadien-abhängigen Expression von B220 (die B Zell spezifische Isoform des „Protein Tyrosin Phosphatase Rezeptors Typ C“ CD45), CD43 (Leukosialin), CD24 (HSA), BP-1 (glutamyl-Aminopeptidase A, CD249) und der membrangebundenen µ-schweren Kette des Immunglobulin M (sIgµ, = BZR).

3.2 Der präB-Zell Rezeptor Checkpoint

Aus einer gemeinsamen lymphoiden Vorläuferzelle (*common lymphoid progenitor*, CLP) entwickelt sich unter der Wirkung des B-Zell spezifischen Transkriptionsfaktors (TF) paired box 5 (PAX5) die prä-proB-Zelle.(Thévenin et al., 1998) Diese stellt die erste, auf die B-Zell Entwicklungslinie festgelegte Zelldifferenzierung dar.(Fuxa and Busslinger, 2007; Schebesta et al., 2007) Zellen, die weiterhin Stammzellmarker wie CD43 auf der Oberfläche exprimieren bei gleichzeitig beginnender Expression von B-Zell Markern, werden als proB-Zellen bezeichnet. ProB-Zellen exprimieren den IL-7 Rezeptor (IL7-R), bestehend aus der IL-7Rα Kette und der *common gamma-chain* (γc) auf ihrer Oberfläche und proliferieren IL-7 abhängig.(Wei et al., 2000) In diesem Stadium erfolgt die somatische Rekombination der schweren Kette (Immunglobulin µ, Igµ) des BZR.(Geier and Schlissel, 2006) *Recombination activating genes* (RAG1/2) bewirken die zum Teil fehleranfällige Veknüpfung von verschiedenen V-, D- und J- Genregionen am Igµ Genlocus. Zellen, die eine erfolgreiche Rekombination von VDJ Elementen der Igµ Kette vollzogen haben, treten in den präB-Zell checkpoint ein: zytoplasmatisch erfolgt die Assemblierung des präB-Zell Rezeptors (präBZR), bestehend aus der Igµ schweren Kette und einer invarianten stellvertretenden leichten Kette (ψL). psiL ist dabei ein Heterodimer aus den Genprodukten *Igll1* (λ5, CD179b) und *Vpreb1/2* (VpreB1/2).(Mårtensson et al., 2010) Der assemblierte präBZR wird auf der Oberfläche der präB-Zellen exprimiert und induziert nach einer kurzen Phase der Zellteilung ein Verlassen des Zellzyklus, sowie die Rekombination der leichten Ketten. Zellen in diesem Stadium werden aufgrund der verringerten Zellgröße nach Verlassen des Zellzykluses auch kleine präB Zellen genannt.(Mårtensson et al., 2010) Ein zentrales Effektormolekül des präBZRs, ist der TF „Interferon-regulierende Faktor 4“ (IRF4),(Johnson et al., 2008; Ma et al., 2006) der zudem vielfältige Funktionen in T Zellen entfaltet.(Huber and Lohoff, 2014; Lohoff and Mak, 2005) Transkriptionelle Wirkungen von IRF4 in präB-Zellen sind unter anderem ein Zellzyklusarrest, sowie die Re-Expression der Rekombinationsmaschinerie (RAG1/2).(Lu et al., 2003) Zudem konnte gezeigt werden, dass IRF4 selbst als Pionier-Faktor daran beteiligt ist, das Chromatin am Igκ Leichtkettenlocus zu entkondensieren, um die Rekombination dieses Locus zu ermöglichen.(Johnson et al., 2008; Ma et al., 2006) Die beschriebenen Funktionen werden zum Teil redundant auch von dem IRF Familienmitglied IRF8 übernommen. IRF4/IRF8 Doppel-KO Mäuse zeigen entsprechend keine Entwicklung über den präBZR checkpoint hinaus.(Lu, 2008; Lu et al., 2003; Pang et al., 2016; Shukla and Lu, 2014)

Die Frage nach der Auslösung des präBZR-Signalweges ist hierbei interessanterweise nicht abschließend geklärt: Der ursprünglichen Vorstellung einer autonomen, Liganden unabhängigen Verlinkung mehrerer Rezeptoreinheiten stehen Daten zu einem Knochenmark-exprimierten Gangliosid gegenüber, das in der Zellkultur eine präBZR-Bindung und dadurch Zell-Stimulation bewirken kann.(Vettermann et al., 2006) Allerdings ist die Möglichkeit einer autonomen Signalinduktion ohne Beteiligung eines Liganden auch nicht abschließend ausgeschlossen: Beide Bestandteile der ψL besitzen endständige „*unique regions*“ (UR), die als bewegliche Aminosäureketten aus dem präBZR hervorragen und potentiell für eine Ligandenbindung oder Autoaggregation zur Verfügung stehen.(Ohnishi and Melchers, 2003)

Sobald die leichte Kette (Igκ oder Igλ) rekombiniert ist, wird das Heterodimer aus Igμ und Igκ/Igλ auf der Zelloberfläche als BZR exprimiert und die Zellen verlassen als Folge einer Synchronisation von chemotaktischen Signalen das Knochenmark, um ihre Funktionen als reife B Zellen in der Peripherie aufzunehmen.(Fistonich et al., 2018)

3.3 Vergleich der Funktionen des IL-7 Rezeptors mit denen des TLSP Rezeptors

Der oben genannte IL-7R vermittelt bei Ligandenbindung die Phosphorylierung von JAK1 und JAK3 und die Aktivierung der „*signal transducer of activated T cells“* (STAT) TFs. Interessanterweise existiert auf präB Zellen zusätzlich zum IL-7R ein weiterer Rezeptorkomplex, der die IL-7Rα Kette beinhaltet: Der *thymic stromal lymphopoetin* (TSLP) Rezeptor ist ebenfalls ein Heterodimer, bestehend aus der IL-7Rα Kette und dem „*cytokine receptor like factor 2“* (CRLF2).(Park et al., 2000) Während die IL-7Rα Kette und das Zytokin IL-7 in Mäusen absolut notwendig sind für eine produktive B Zell Entwicklung,(Freeden-Jeffry et al., 1995; Peschon et al., 1994) scheint dies beim Menschen nicht der Fall zu sein; *Loss-of-function* Mutationen im menschlichen IL-7R Signalweg führen zur Immunschwäche-Erkrankung „X-linked severe combined immunodeficiency disease“ (X-SCID), bei der sich T- und NK-Zellen nicht ausbilden können. B Zell-Zahlen sind bei dieser Erkrankung jedoch nicht beeinträchtigt.(Puel et al., 1998) In Menschen, jedoch nicht in Mäusen, fungiert TSLP daher vermutlich als redundantes Zytokin zu IL-7. Der TSLPR unterscheidet sich vom IL-7R

mechanistisch dadurch, dass JAK1 und JAK2 an Stelle von JAK1 und JAK3 die Signaltransduktion vermitteln.(Park et al., 2000)

3.4 Die „B-Zell Vorläufer akut lymphoblastische Leukämie“ (BCP-ALL)

Der geschilderte Ablauf von aufeinanderfolgenden Differenzierungsschritten ist anfällig für maligne Entartung. Die sogenannte „B Zell Vorläufer akute lymphoblastische Leukämie“ (BCP-ALL) ist eine hochaggressive neoplastische Erkrankung, die aus veränderten B-Zell Vorläuferzellen hervorgeht.(Longo et al., 2015) Dem Inzidenzgipfel im Kindesalter, der mit einer hohen Heilungschance verbunden ist, stehen ein vergleichsweise selteneres Auftreten der BCP-ALL im Erwachsenenalter gegenüber, welches jedoch mit einer deutlich schlechteren Prognose verbunden ist.(Roberts, 2018)

Es existiert ein weites Spektrum an bekannten ursächlichen Onkogenen für die BCP-ALL. Durch neuere Methoden wie Transkriptom-Profiling werden in aktuellen Phänotypisierungsstudien auch weiterhin neue Subformen beschrieben und definiert.(Li et al., 2018) Auf diese Art wurde mit der *Ph-like* Leukämie eine Leukämie-Subform mit typischem BCR-ABL (Ph^+) Transkriptom bei fehlendem biologischen Nachweis eines BCR-ABL Fusiononkogens neu definiert.(Roberts et al., 2017; Tasian et al., 2017) Die *Ph-like* Leukämie zeichnet sich vielmehr durch Fusionen und Mutationen von anderen Kinase- und Rezeptormolekülen aus.(Roberts et al., 2014) Die häufigsten Alterationen betreffen den *Thymic stromal lymphopoietin* (TSLP) Rezeptor (*TSLPR/CRLF2*). Weitere Mutationen betreffen darüber hinaus die Januskinase 2 (*JAK2*), sowie verwandte Gene vor allem des IL-7 Signalweges (*Il7R, JAK1, JAK3, RAS*). Typisch sind weiterhin der Verlust von bekannten ALL Tumorsuppressoren wie dem Transkriptionsfaktor Ikaros (*IKZF1*).(Mullighan et al., 2009)

3.5 Transkriptionelle Regulation von T-Effektor- und T-regulatorischen $CD4^+$ T-Zellen.

Funktionell sind innerhalb der $CD4^+$ T-Zellen zwei wesentliche Zelltypen zu unterscheiden: T-Effektorzellen (T_{eff}) und die zahlenmäßig selteneren T-regulatorischen (T_{reg}) Zellen. Für den ersten Zelltyp, der in Form pro-inflammatorischer T-Zellen Träger zellvermittelter Immunität ist, ist elementar wichtig, dass ein Signal über den T-Zell Rezeptor –ähnlich wie beim oben beschriebenen präB-Zell Rezeptor– in der Lage ist, den Transkriptionsfaktor

IRF4 zu induzieren.(Huber and Lohoff, 2014; Mittrücker et al., 1997) IRF4 entfaltet auch in T-Zellen vielfältige Aufgaben: je nach T-Helferzelldifferenzierungsprogramm, werden unterschiedliche Bindungspartner von IRF4 induziert, die seine Funktion leiten und modulieren. Die *Activator protein-1* (AP-1) Familien Mitglieder *basic leucine zipper transcription factor* (BATF) und *jun proto-oncogene* (JUN) sind prominente Beispiele für Bindungspartner von IRF4, die IRF4 an sogenannte *AP-1-IRF4 composite elements* (AICE) in Promotorregionen rekrutieren.(Li et al., 2012) *Irf4*$^{-/-}$ Mäuse zeigen daher starke Einschränkungen im T_{eff} Kompartiment.(Brüstle et al., 2007; Lohoff et al., 2002)

T_{reg} Zellen können in Abgrenzung zu T_{effs} durch die Expression eines weiteren Kooperationspartners von IRF4 identifiziert werden: dem Subtyp-spezifischen TF *forkhead box P3* (FoxP3).(Fontenot and Rudensky, 2005; Zheng et al., 2009) Die Funktion von T_{regs} ist die Suppression von T_{effs} unter anderem durch (1.) die Produktion von inhibitorischen Zytokinen (u.a. TGF-β, IL-10), (2.) die Expression des hochaffinen IL-2 Rezeptors, der wie ein molekularer Schwamm die Konzentration von freiem IL-2 am Ort einer T-Zell Antwort limitieren und somit die Teff-Expansion begrenzen kann, sowie (3.) durch die Expression von ko-inhibitorischen Molekülen *wie cytotoxic T-lymphocyte associated protein 4* (CTLA4), die im Rahmen direkter Zell-Interaktion die T-Zell Aktivierung beschränken können.(Shevach, 2009) Die korrekte Funktion von FoxP3^{+} CD4^{+} T-Zellen ist unabdingbar für die Verhinderung überschießender Immunreaktionen. Eindrücklich ist dies ersichtlich durch die Entwicklung der schweren systemischen Autoimmunerkrankung IPEX (Immundysregulation, Polyendokrinopathie, Enteropathie, X-vermittelte Vererbung), die bei Patient:innen auf Mutationen in dem auf Chromosom X kodierten FoxP3 Gen zurückzuführen ist.(Gambineri et al., 2003)

3.6 Ziele der Arbeit

Im Rahmen der vorliegenden Arbeit wurde zunächst die spontane Entwicklung einer BCP-ALL in *Irf4*$^{-/-}$ Mäusen beschrieben und die Leukämiezellen wurden näher charakterisiert. In der Folge sollten sowohl die zugrundeliegenden präleukämischen Alterationen untersucht werden, die *Irf4*$^{-/-}$ Mäuse für die Entwicklung einer BCP-ALL prädestinierten, wie auch die sekundären somatischen Veränderungen, die im Rahmen der Leukämieentstehung entstanden. Da *Irf4*$^{-/-}$ Mäuse eine eingeschränkte, aber grundsätzlich produktive B Zell

Entwicklung aufweisen,(Mittrücker et al., 1997) wurde von der Hypothese einer sekundär somatisch entstehenden Leukämie ausgegangen, deren Grundzüge im *Irf4*$^{-/-}$ Genotyp kodiert liegen. Da auch bei der BCP-ALL beim Menschen sekundäre somatische Mutationen zunächst eine klonale B-Zell Entwicklung begünstigen und in der Folge eine vollständige leukämische Transformation bewirken können, sollten zuletzt die gewonnenen Erkenntnisse mit dem Krankheitsspektrum beim Menschen verglichen werden.

Parallel sollten Techniken der Transkriptionsfaktor-Überexpression, die im Rahmen der oben genannten Experimente zum Einsatz kamen, auf Fragestellungen in T_{reg} Zellen angewandt werden.

4. Zusammenfassung publizierter Ergebnisse

4.1 IRF4 Defizienz in Mäusen resultiert in einer präleukämischen B Zell Entwicklung

Das Gupta, D. *et al.* IRF4 deficiency vulnerates B-cell progeny for leukemogenesis via somatically acquired Jak3 mutations conferring IL-7 hypersensitivity. *Cell Death Differ* 1–14 (2022) doi:10.1038/s41418-022-01005-z.

Da *Irf4*$^{-/-}$ Mäuse im Alter von > 150 Tagen mit einer Inzidenz von 17,5 % eine letale leukämische Erkrankung ausgehend von B220^{+}sIgμ^{-} frühen B Zell Vorläufern entwickelten (Fig. 1a-h), sollte zunächst die B Zell Entwicklung in klinisch gesunden *Irf4*$^{-/-}$ Mäusen mit wt Mäusen verglichen werden. Unter Anwendung der Hardy Klassifikation(Hardy and Hayakawa, 2001; Hardy et al., 1991) wurde ein vermehrtes Vorkommen von Fr. C präB-I Zellen festgestellt (Fig. 2a-c). In *in vitro* Kulturen zeigten *Irf4*$^{-/-}$ Vorläuferzellen zudem eine deutlich erhöhte Proliferationsantwort auf IL-7 Exposition (Fig. 2d). IL-7 führte zudem zur Unterdrückung der weiteren Differenzierung jenseits des präBZR Checkpoints in *Irf4*$^{-/-}$ Knochenmarkszellen (Fig. 2d-h).

Bereits in gesunden *Irf4*$^{-/-}$ Mäusen konnten darüber hinaus B Zell Vorläufer in erhöhter Frequenz in der Peripherie detektiert werden (Fig. 2i). Um zu untersuchen, ob diesem verfrühten Austritt aus dem Knochenmark eine verringerte Adhäsion an die IL-7 produzierende Stroma-Nische zugrunde liegt, wurden zunächst *Il7*^{eGFP} Reportermäuse(Hara et al., 2012) mit *Irf4*$^{-/-}$ Mäusen verpaart. *Il7*^{eGFP} *Irf4*$^{+/+}$ Mäuse dienten als Kontrolle. An Knochenmark-Kryoschnitten entsprechend der Kawamoto-Filmtechnik(Kawamoto, 2003) wurde sodann der mittlere Abstand von B220^{+}CD2^{-} B Zell Vorläufern zu den GFP exprimierenden IL-7 produzierenden Stromazellen gemessen. Es zeigte sich ein im Mittel größerer Abstand der beschriebenen Zellpopulation zu der designierten Stroma-Nische in *Irf4*$^{-/-}$ gegenüber *Irf4*$^{+/+}$ Knochenmärkern (Fig. 2j-m).

Da die Interaktion von B Zell Vorläufern mit KM-Stromazellen zentral über die chemotaktische Wirkung von CXCL12 am CXCR4 Rezeptor auf der Oberfläche der B Zell Vorläufer vermittelt wird, untersuchten wir die Expressionsstärke von CXCR4 auf der Oberfläche von Hardy Fr. A-D Zellen in *Irf4*$^{-/-}$ und wt Mäusen. *Irf4*$^{-/-}$ Hardy Fr. A-D Zellen zeigten eine deutlich verminderte Expression von CXCR4 (Fig. 2n), im Einklang mit publizierten Transkriptom-Daten.(Johnson et al., 2008) Zuletzt wurde die funktionelle Relevanz der reduzierten CXCR4 Expression in Boyden-Kammer Experimenten untersucht:

Hierbei zeigten MACS aufgereinigte Fr. A-D Zellen aus *Irf4*$^{-/-}$ Mäus-Knochenmärkern im Vergleich zu wt Kontrollzellen eine deutlich verringerte Migration als Antwort auf rekombinantes CXCL12 (Fig. 2o).

In der Zusammenschau bedeutet der Verlust von IRF4 in der B Zell Entwicklung folglich die Etablierung eines präleukämischen Zustandes, der sich zentral durch zwei Charakteristika definiert:
(1.) *Irf4*$^{-/-}$ B Zell Vorläufer zeigen eine deutlich verringerte Tendenz der Differenzierung jenseits des präBZR Checkpoints und eine deutlich potenzierte proliferative Antwort auf IL-7.
(2.) *Irf4*$^{-/-}$ B Zell Vorläufer sind aufgrund verringerter Expression des Chemokinrezeptors CXCR4 schwächer adhärent an die designierte Knochenmarknische, erhalten dadurch weniger Zugang zu IL-7 und verlassen zusätzlich bereits in gesunden Mäusen vermehrt als unreife Zellen das Knochenmark.

4.2 *Irf4*$^{-/-}$ Leukämien zeigen eine erhöhte IL-7 Sensitivität durch rekurrierende *Jak3* Mutationen

Die Analyse der B Zell Entwicklung in *Irf4*$^{-/-}$ Mäusen hatte eine deutlich erhöhte Proliferation bei funktionell weitgehender Blockade der Differenzierung unter kontinuierlicher IL-7 Exposition ergeben. Die so behandelten Zellen verhielten sich *in vitro* analog zu vollständig transformierten *Irf4*$^{-/-}$ Leukämiezellen. Daher wurden verschiedene *Irf4*$^{-/-}$ Maus-Leukämieproben auf das Vorhandensein von somatischen Mutationen im IL-7 Signalweg untersucht. Exom-Sequenzierungen ergaben, dass unter den wenigen Genen, die in allen drei getesteten *Irf4*$^{-/-}$ Leukämien gleichermaßen alteriert waren, *Jak3* vertreten war (Fig. 3a-c). JAK3 und JAK1 sind die beiden direkten Signalmoleküle, die in der Folge von Ligandenbindung an den IL-7 Rezeptors phosphoryliert und somit aktiviert werden. Sanger Sequenzierungen von weiteren *Irf4*$^{-/-}$ Leukämieproben erbrachten weitere *Jak3* Punktmutationen. Um die funktionellen Auswirkungen dieser Mutationen auf den IL-7 Signalweg zu testen, wurden die JAK3 Mutanten durch *site-directed mutagenesis* mit Hilfe der wt *Jak3* Sequenz generiert und unter Benutzung des murinen Stammzell Virus (pMSCV) Expressionssystems in Form von Retroviren in *Irf4*$^{-/-}$ präB Zell Kulturen überexprimiert. Ein JAK3-wt Konstrukt sowie der entsprechende Leervektor dienten als Kontrollen. Die JAK3 Mutanten konnten keine IL-7 Unabhängigkeit in präB Zellen bewirken, wohl aber eine bis

um den Faktor 10^3 erhöhte Sensitivität für IL-7 (Fig. 3g, sFig. 3). Die *Jak3* Mutationen können somit als *gain-of-function* (GOF) Mutationen klassifiziert werden und stellen eine wahrscheinliche Erklärung für die maligne Transformation der *Irf4*$^{-/-}$ präleukämen B Zell Vorläufer dar. Sie erlauben den Tumorzellen offenkundig das Überleben auch unter IL-7-limitierten Bedingungen.

Strukturvorhersagen durch den α-fold Algorithmus(Jumper et al., 2021; Varadi et al., 2021) zeigten eine auffällige Ähnlichkeit der in den *Irf4*$^{-/-}$ Leukämie beschriebenen *Jak3* Mutationen mit rekurrierenden *JAK2* Mutationen in der humanen *Ph-like* Leukämie Subgruppe (Fig. 4b-f): sowohl R653 in JAK3, wie auch die korrespondierende Aminosäure R683 in JAK2 liegen in der jeweiligen Pseudokinase Domäne, die regulierend auf die Funktion der Kinasedomäne wirkt. Beide Aminosäuren stehen in physischem Kontakt mit T844 in JAK3, bzw. T875 in JAK2 – Beide Threonine befinden sich in der Kinasedomäne des jeweiligen Proteins. R683 Mutationen sind die häufigsten Punktmutationen in *JAK2* in der menschlichen Ph-like ALL, während T875 Mutationen ebenfalls beschrieben sind.(Herold et al., 2016) Da JAK3 als Signalmolekül des IL-7 Rezeptors und JAK2 als Signalmolekül des TSLP Rezeptors fungieren (Fig. 4a), erschien es möglich, dass die Unterschiede in der betroffenen Kinase auf eine unterschiedliche Funktion der Zytokine bei Menschen und Mäusen zurückzuführen sind. Während bei menschlichen B Zell Vorläufern in der Literatur eine vergleichbare Proliferation unter IL-7 und TSLP beschrieben ist,(Milford et al., 2016) zeigten *Irf4*$^{-/-}$ B Zell Vorläufer eine deutlich erhöhte Proliferation mit IL-7 im Vergleich zu TSLP. Dies könnte erklären, warum die Mausleukämie präferentiell *Jak3* Mutationen aufweist, während in der menschlichen Ph-like ALL demgegenüber häufiger die korrespondierenden *JAK2* Mutationen nachgewiesen werden.

4.3 IRF4 Re-Expression induziert die Differenzierung von vollständig transformierten Leukämiezellen

Da die beschriebenen Maus-Leukämien auf der Basis einer vorbestehenden IRF4 Deletion entstanden waren, wurde getestet, wie vollständig transformierte *Irf4*$^{-/-}$ Leukämiezellen auf die Re-Expression von IRF4 regieren würden. Viruspartikel, die für IRF4 und den Transduktionsmarker GFP (green fluorescent protein) oder nur für GFP alleine kodieren, wurden genutzt, um aus *Irf4*$^{-/-}$ Leukämien generierte Zelllinien (T8, T11) zu transduzieren.

Die Re-Expression von IRF4 induzierte dabei Apoptose in den Zelllinien (Fig. 5a). Zudem wurde der Verlust von λ5, als Surrogatmarker für das Vorhandensein des präBZR auf der Oberfläche der Zellen, festgestellt (Fig. 5b-c). RNA Sequenzierungen von IRF4 re-exprimierenden T8 und T11 Zellen belegten auf transkriptioneller Ebene die Herunterregulierung der präBZR Bestandteile, sowie Signalweg-Signaturen, die eine Ausdifferenzierung der Leukämiezellen jenseits des präB-I Phänotypes belegten (Fig.5d-h). Somit führt die Re-Expression von IRF4 auch in vollständig transformierten Leukämiezellen zu der physiologischerweise durch IRF4 induzierten Differenzierung.

4.4 Ruxolitinib-Behandlung bewirkt eine Verringerung leukämischer Infiltration in solide Organe

Da *Irf4*$^{-/-}$ Leukämien JAK Mutationen aufwiesen, wurde zunächst *in vitro* das Ansprechen der Leukämiezelllinien auf die pharmakologische Blockade von JAKs untersucht. Mehrere aus *Irf4*$^{-/-}$ Leukämien generierte Zelllinien (T8, T11) konnten durch Ruxolitinib, einen bereits beim Menschen eingesetzten JAK1/2 Inhibitor abgetötet werden. Theoretisch ist die Wirkung eines JAK1/2 Inhibitors auf JAK3-mutierte Leukämiezellen dadurch zu erklären, dass JAK3-mediierte Signale auf die Funktion des Kooperationspartners JAK1 angewiesen sind.(Haan et al., 2011) Experimente, die Ruxolitinib in Kombinationen mit anderen anti-leukämischen Medikamenten testeten, ergaben deutlich synergistische Effekte bei Kombinationen mit Dexamethason. Diese Kombinationstherapie wurde in einem nächsten Schritt *in vivo* getestet. 12 Tage nach der intraperitonealen Injektion von *Irf4*$^{-/-}$ Leukämiezellen in wt Mäuse, wurde das Vorhandensein einer Leukämie über eine Blutentnahme aus Schwanzblut dokumentiert und eine Induktionstherapie mit Dexamethason eingeleitet (Fig. 6a). Nach 7 Tagen Dexamethason-Gabe über das Trinkwasser zeigte sich reproduzierbar eine deutliche Reduktion der Leukämielast im Blut auf unter 5 % Blasten im Lymphozytengate (Fig. 6b-c). Im Anschluss erfolgte eine Konsolidierungstherapie mit Ruxolitinib per oraler Gavage im Vergleich zur Lösungsmittel Kontrolle.

Die Therapie mit Ruxolitinib hatte dabei keinen signifikanten Einfluss auf das Wiederansteigen der Blastenfrequenz im peripheren Blut (Fig. 6c). Dem gegenüber konnte dennoch ein klarer Überlebensvorteil für Mäuse dokumentiert werden, die mit Ruxolitinib behandelt worden waren (Fig. 6d). Das verlängerte Überleben korrelierte auch mit klinischen

Unterschieden: Während Kontroll-gavagierte Mäuse mit Fortschreiten des Versuches zunehmende, reversible Lähmungen der Hinterläufe entwickelten, wurde dieses Phänomen durch die Gavage mit Ruxolitinib unterdrückt (Fig. 6e). Histologische Analysen von Transversalschnitten der Lendenwirbelsäule ergaben eine deutliche intraspinale Infiltration mit Blasten bei Kontroll-gavagierten Mäusen. Mäuse, die mit Ruxolitinib behandelt worden waren, zeigten hingegen weniger Lähmungen und wiesen eine stark reduzierte intraspinale Infiltration auf (Fig. 6f-h). Darüber hinaus ergaben Analysen von Leberschnitten eine deutliche Reduktion der periportalen Blasteninfiltration unter Ruxolitinib-Therapie (Fig. 6k-l). Diese Befunde kontrastierend bestätigten CAE Färbungen des Knochenmarks derselben Mäuse die Ergebnisse der Blutuntersuchungen in der Hinsicht, dass Ruxolitinib keinen wesentlichen Einfluss auf die Leukämielast im hämatopoetischen Kompartiment entfaltete (Fig. 6i-j). Somit wurde konstatiert, dass Ruxolitinib bei Verwendung als Konsolidierungs-Medikament einen Überlebensvorteil bewirkte, der in Zusammenhang stand mit einer spezifischen Reduktion der Organinfiltration, ohne eine systemisch anti-neoplastische Wirkung zu entfalten.

4.5 Generierung von FoxP3 kodierenden Retroviren für Rekonstitutionsexperimente in Treg Zellen

Kurniawan, H. *et al.* Glutathione Restricts Serine Metabolism to Preserve Regulatory T Cell Function. *Cell Metab* **31**, 920-936.e7 (2020).

Da die Re-Expression von IRF4 in *Irf4*$^{-/-}$ Leukämien physiologische Differenzierungs-Prozesse re-initiieren konnte, wurde eine ähnliche Fragestellung für Glutamat-Cystein-Ligase (*Gclc*) defiziente T_{regs} entworfen, die eine deutlich verringerte immunsuppressive Kapazität zeigten: Da *Gclc*$^{-/-}$ T_{regs} verringerte Expressionsstärken des T_{reg} Master-Regulator TFs FoxP3 aufwiesen (Fig. 4B-C), wurde untersucht, ob die Re-Expression von FoxP3 zu einer Normalisierung der Funktion der mutierten T_{reg} Zellen führen könne. Hierfür wurden analog zu Punkt 4.3 Viruspartikel generiert, die für den TF FoxP3 kodieren, um *Gclc*$^{-/-}$ T_{regs} zu infizieren. Unter FoxP3 Überexpression normalisierten sich die suppressive Kapazität der *Gclc*$^{-/-}$ T_{regs} (Fig. 6G), sowie die metabolischen Alterationen, die mit der *Gclc*-Defizienz einhergingen (Fig.6 H-K). Somit konnte geschlossen werden, dass *Gclc*-Defizienz in T_{regs} über eine verringerte FoxP3 Expression zu einer verringerten T_{reg} Funktionalität führt.

4.6 technischer Beitrag: Probenentnahme und -Asservierung für Antigen-spezifische $CD4^+$ T-Zell Analysen

Romero-Olmedo, A. J. *et al.* Induction of robust cellular and humoral immunity against SARS-CoV-2 after a third dose of BNT162b2 vaccine in previously unresponsive older adults. *Nat Microbiol* **7**, 195–199 (2022).

Romero-Olmedo, A. J. *et al.* Dynamics of humoral and T-cell immunity after three BNT162b2 vaccinations in adults older than 80 years. *Lancet Infect Dis* (2022) doi:10.1016/s1473-3099(22)00219-5.

Das SARS-CoV2 Virus hatte zum Zeitpunkt der Promotionsarbeit eine pandemische Ausbreitung erreicht und verursachte eine hohe gesellschaftliche Erkrankungslast. Als Nebenprojekt sollte deshalb der zeitliche Verlauf antigen-spezifischer T-Zell Antworten auf die neuen mRNA basierten Vakzine gegen das SARS-CoV 2 Virus untersucht werden. Die Probengewinnung erfolgte zu definierten Zeitpunkten vor und nach der Impfung mit dem von BioNtech/Pfizer hergestellten Impfstoff BNT162b2. Über Dichtegradientenzentrifugation wurde die Leukozytenfraktion von den roten Blutkörperchen getrennt. Anschließend wurden die Zellen stimuliert mit Peptid-Bruchstücken des Spike Proteins von SARS-CoV2. Als Negativkontrolle dienten unstimulierte Zellen, als Positivkontrolle dienten Zellen, die mit dem T-Zell Superantigen Staphylokokken Enterotoxin B stimuliert wurden.

5. Diskussion

Die BCP-ALL ist eine Erkrankung präferenziell des Kindesalters mit einem zweiten Erkrankungsgipfel im hohen Erwachsenenalter.(Longo et al., 2015; Malard and Mohty, 2020) Eine besondere Gruppe an Patient:innen stellen die Adoleszenten und jungen Erwachsenen dar. Innerhalb dieser Gruppe sinkt das mittlere zu prognostizierende Überleben bei Diagnosestellung drastisch ab.(Katz et al., 2015) Genetische Untersuchungen konstatierten zudem eine deutlich abweichende Erkrankungsbiologie mit mehr Mutationen und einem distinkten Spektrum an Treibermutationen und Genfusionen. Innerhalb dieser Patientengruppe nimmt auch die Inzidenz der *Ph-like* Leukämie zu, einer Leukämieform, die im Kindesalter im Vergleich dazu deutlich unterrepräsentiert ist.(Roberts, 2018) Die Entstehungsmechanismen und die Biologie der BCP-ALLs im Erwachsenenalter bleiben bislang weitgehend unverstanden. Umfang dieser Arbeit ist die Dokumentation und mechanistische Untersuchung von spontanen aber repräsentativen BCP-ALL in älteren *Irf4*$^{-/-}$ Mäusen, die potentiell auf ähnliche Leukämie-induzierende Prozesse im Menschen hinweisen können.

IRF4 wurde bereits in früheren Arbeiten als Tumorsuppressor in der frühen B Zell Entwicklung charakterisiert.(Acquaviva et al., 2008; Lu, 2008; Lu et al., 2003; Pang et al., 2016) Die erste dokumentierte tumorsuppressive Wirkung von IRF4 war die Reduktion der Proliferation von BCR-ABL transformierten B Zell Vorläufern in Überexpressionsversuchen.(Acquaviva et al., 2008) Zudem wurde in verschiedenen Doppel-KO Mausmodellen mit IRF4 Deletion (*Irf4/Spib, Irf4/Irf8* Doppel-KO) das Auftreten von Leukämien mit hoher Frequenz festgestellt.(Pang et al., 2016) Die hier beschriebene Originalarbeit unterscheidet sich zu diesen Arbeiten in der Hinsicht, dass das mechanistische Verständnis des präleukämischen Zustandes einer IRF4-defizienten B Zell Entwicklung erweitert wurde. Hierbei ist vor allen Dingen für die translationelle Bedeutung der Ergebnisse zu berücksichtigen, dass *Irf4*$^{-/-}$ Mäuse im Gegensatz zu den bereits beschriebenen Doppel-KO Modellen eine eingeschränkte, aber noch produktive B Zell Entwicklung aufweisen.(Mittrücker et al., 1997) Somit erlaubt der Einzel-KO das Nachvollziehen einer Leukämieentstehung ausgehend von einer zunächst nur subklinisch alterierten B Zell Entwicklung. Die in *Irf4*$^{-/-}$ Mäusen somit im Vergleich zu Doppel-KO Mäusen seltener und später auftreten Leukämien stellen deshalb ein genaueres Modell der Leukämieentstehung im Menschen dar.

5.1. Präleukämie in *Irf4*$^{-/-}$ Mäusen

IRF4 Verlust führte zu einer verringerten Adhäsion von B-Zell Vorläufern an die designierte Entwicklungsnische im Knochenmark, sowie zu einer deutlich reduzierten Differenzierung jenseits des präBZR Checkpoints. Beide Mechanismen charakterisieren einen präleukämischen Zustand. Die Rolle des Differenzierungsblockes ergibt sich dabei eindrücklich aus der damit verbundenen IL-7 Hypersensitivität und dem erhöhten proliferativen Potential. Die Rolle der reduzierten Adhärenz an die Knochenmarknische ist weniger direkt. *In vitro* konnte gezeigt werden, dass das Neutralisieren von IL-7 in Kultur, sowie die Exposition von *Irf4*$^{-/-}$ präB Zellen gegenüber LPS zur Induktion von *Activation induced cytidine deamidase* (AID) führen, einem mutagenen Enzym, das physiologischerweise in der Affinitätsmaturierung von Antikörpern im Rahmen der Keimzentrumsreaktion von B-Zellen Cytosin zu Thymin Mutationen in Immunglobulingenen einführt.(Noia and Neuberger, 2002; Petersen-Mahrt et al., 2002) Interessanterweise zeigen die Exomsequenzierungen von *Irf4*$^{-/-}$ Leukämien einen Überhang an C zu T Nukleobasen-Transitionen. Zudem waren fünf von sechs detektierten Punktmutationen im JAK3 Gen C zu T Transitionen. Diese Ergebnisse favorisieren ein Modell, in dem ein verfrühtes Auswandern von B-Zell Vorläufern aus dem Knochenmark zu einer ektopen Expression von AID führen kann und somit einen mutagenen Prozess begünstigen kann. Dieses Modell wird zudem unterstützt von publizierten Arbeiten an *Pax5*$^{+/-}$ Mäusen: In diesem Leukämie-Modell führte das Überführen von Mäusen aus einer *specific pathogen free* (SPF) Haltung in eine mikrobiologisch weniger strikt eingeschränkte Tierhaltung zu einer deutlichen Erhöhung der Leukämiefrequenz.(Vicente-Dueñas et al., 2020) Diese wegweisende Studie konnte somit einen eindrücklichen Hinweis auf die Rolle infektiöser Stimuli für die Leukämogenese geben. In einer anderen Studie konnte bereits in wt präB Zellen gezeigt werden, dass eine IL-7 Restriktion zur Induktion von AID führt.(Swaminathan et al., 2015) Die hier beschriebene und mechanistisch untersuchte reduzierte KM-Adhäsion stellt eine wahrscheinliche Ursache sowohl für eine IL-7 Restriktion als auch für die Exposition gegenüber Pathogen-Bestandteilen für präleukämische B-Zell Vorläufer dar und ist somit eine naheliegende Erklärung für die Initiation mutagener Prozesse durch ektope AID-Expression.

5.2 Leukämie in *Irf4*$^{-/-}$ Mäusen

Die Entstehung von Leukämien in *Irf4*$^{-/-}$ Mäusen war verlässlich begleitet vom Auftreten von *Jak3* Mutationen. Interessanterweise ergab der Vergleich der JAK2 und JAK3 primär- bis tertiär-Strukturen Aufschluss über wichtige Ähnlichkeiten zwischen dem beschriebenen Mausmodell einer BCP-ALL und der *Ph-like* ALL beim Menschen. Potentiell erklärt sich die Differenz der betroffenen Januskinase zwischen Maus und Mensch durch die differenzielle und evolutionär abgewandelte Wirkung der Zytokine TSLP und IL-7. Das im Rahmen dieser Arbeit dargestellte, effektivere Proliferieren von *Irf4*$^{-/-}$ präB Zellen unter IL-7 im Vergleich zu TSLP erhärtet diese Hypothese.

Wichtig ist in diesem Zusammenhang die Feststellung, dass eine Überexpression von JAK3 Mutanten in primären *Irf4*$^{-/-}$ präleukämischen präB-I Zellen nicht zu einer Zytokin-Unabhängigkeit führte, sondern lediglich die Sensitivität deutlich erhöhte. Da im menschlichen JAK2 sehr ähnliche Mutationen an den entsprechenden, konservierten Aminosäuren auftreten, ist eine Übersetzung dieser Beobachtung auf menschliche JAK2 mutierte Zellen wahrscheinlich. Diese Übertragung stellt auch eine attraktive Erklärung dar, warum in menschlichen *Ph-like* ALL Zellen JAK2 Mutationen und CRLF2 Rearrangements gemeinsam auftreten.(Roberts et al., 2014) CRLF2-Mutationen könnten somit noch einen additiven Effekt zu JAK2 Mutationen entfalten. Unter Einbeziehung publizierter biochemischer und biomechanischer Informationen über den IL-7 Rezeptor(McElroy et al., 2012) wurde von mir ein Modell für die Funktionsweise der JAK Mutanten abgeleitet. Zentral für das von uns postulierte Verständnis ist die Tatsache, dass sowohl in menschlicher, wie auch in muriner BCP-ALL mit JAK Mutationen typischerweise die in räumlicher Nähe stehenden R653/R683, sowie T844/T875 Aminosäuren mutiert sind.(Herold et al., 2016) Die beiden Aminosäuren befinden sich in hochkonservierten Regionen der JAKs im Bereich einer Schnittstelle von Kinase- und Pseudokinasedomäne. Innerhalb der JAK-Familienmitglieder scheint die Pseudokinase eine hemmende Wirkung auf die Kinasedomäne zu entfalten.(Lupardus et al., 2014) Mutationen innerhalb der Schnittstelle können also, wenn sie zu einer Herabsetzung der Kinase-Pseudokinase Interaktion führen, eine Enthemmung der Enzymaktivität bedeuten. Um zu erklären, warum es dennoch nicht zu einer IL-7 Unabhängigkeit kommt, ist zu beachten, dass der IL-7 Rezeptor aus IL-7R α und der γ-Kette prä-assembliert auf der Zelloberfläche vorliegt.(McElroy et al., 2012) Die Bindung des Zytokins führt zu einer Konformationsänderung beider Ketten, die intrazellulär

mit JAK1 und JAK3 interagieren. Erst diese Konformationsänderung führt dazu, dass JAK1 und JAK3 in räumliche Nähe zueinander gebracht werden und sich gegenseitig phosphorylieren können. Dieser erste Schritt ist notwendig für das Auslösen der weiteren IL-7 Signalkaskade. Das Lösen der Kinasedomäne von der Pseudokinase wäre ein von dieser Konformationsänderung komplett losgelöster, zweiter Prozess. Fügt man beide Prozess-Gleichgewichte modelhaft zusammen (Fig. 8 in der Publikation), so ergibt sich eine naheliegende Erklärung, warum die JAK Mutationen nicht zu einer IL-7 Unabhängigkeit führen können, wohl aber einer deutlichen Verbesserung der IL-7 Sensitivität in IL-7 restriktierten Bedingungen.

Diese Zusammenhänge sind von Relevanz für die menschliche Erkrankung, da sie die Möglichkeit aufzeigen, dass zumindest ein Teil der menschlichen *Ph-like* Leukämien ebenfalls keine vollkommene Zytokin-Unabhängigkeit aufweist. Diese Möglichkeit deutet somit auf einen potentiellen Therapieansatz, nämlich die systemische Neutralisierung von IL-7/TSLP.

5.3 Leukämietherapie im IRF4-Deletionsmodell

Die JAK abhängige Pathogenese der *Irf4*$^{-/-}$ Leukämien veranlasste die Testung von JAK Inhibitoren als mögliche Therapeutika. Die Therapie von Leukämie-tragenden Mäusen mit Ruxolitinib, einem JAK1/2 Inhibitor, der im Rahmen hämatologischer Erkrankung wie den myeloproliferativen Neoplasien bereits am Menschen eingesetzt wird,(Verstovsek et al., 2012) führte entgegen der Ergebnisse aus *in vitro* Vorexperimenten zwar zu einem Überlebensvorteil, jedoch nicht zu einer detektierbaren Reduktion der Leukämielast im Blut. Dennoch konnte mit der Reduktion der Organinfiltration ein histologisches Korrelat für die verbesserte klinische Situation der Mäuse gefunden werden. Theoretisch bestehen zwei Möglichkeiten, wie dieser Effekt zustande kommen kann: einerseits könnte Ruxolitinib eine Organ-spezifische antineoplastische Wirkung entfalten und zum Absterben von Leukämiezellen spezifisch in Organen wie ZNS oder Leber führen. Andererseits könnte Ruxolitinib die Infiltration von Leukämiezellen in die Organe von vorne herein unterbinden. Die Unterscheidung beider Möglichkeiten ist nicht trivial und konnte in der vorliegenden Arbeit nicht abschließend erreicht werden. Die Analyse von Proben direkt im Anschluss an die Induktionstherapie mit Dexamethason ergab jedoch eine bereits bestehende, marginale

Infiltration mit Leukämie-Zellen, die auch in der Folge durch Ruxolitinib nicht eradiziert werden konnte. Dieser Befund deutet eher auf eine Verhinderung der Infiltration durch Ruxolitinib hin. Zudem ergaben *in vitro* Experimente mit Ruxolitinib, dass *Irf4*$^{-/-}$ Leukämiezellen unter sub-lethaler Ruxolitinib Behandlung die Expression von CD29 (Integrin β1) auf der Oberfläche reduzieren. Da Integrin β1 Heterodimere wichtige Assoziationsmoleküle darstellen, die den Eintritt in viele Organe vermitteln,(Altevogt et al., 1995) stellt dieser Befund eine potenzielle (wenn auch funktionell nicht belastbare) Erklärung für die beobachteten Ruxolitinib Wirkungen *in vivo* dar.

Der translationale Wert der beschriebenen Beobachtungen ergibt sich aus der Tatsache, dass die ZNS-Infiltration bei menschlicher BCP-ALL eine ernste Komplikation ist und historisch eine der wichtigsten Rezidiv-Manifestationen darstellt.(Krishnan et al., 2010) In aktuellen klinischen Therapieprotokollen ist daher die ZNS Bestrahlung oder die direkte Applikation von Chemotherapeutika in den Spinalkanal der Standard. Auch wenn diese Maßnahmen hoch wirksam sind in der Reduktion der sogenannten *meningeosis leukaemica* (i.e. der zentralnervösen Infiltration der Hirnhäute durch Leukämiezellen), so ist die Einschränkung der Lebensqualität durch die angeführten Therapiemaßnahmen immens. Zudem birgt vor allem die ZNS Bestrahlung das Risiko von Sekundärmalignitäten im höheren Lebensalter, die schwer zu therapieren sind und ein hohes Sterberisiko bedeuten.

5.4 Ausblick

Die in dieser Arbeit geschilderten Ergebnisse lassen sich einordnen in aktuelle Bemühungen, die Biologie und die Entstehung von BCP-ALL in Erwachsenen zu verstehen. Obwohl der Initialbefund der spontanen Leukämogenese nicht das Ergebnis einer gezielten Modellierung von menschlicher Leukämie war, konnten über die Charakterisierung der entstehenden malignen Erkrankung wichtige Verbindungen zur menschlichen Erkrankung hergestellt werden. Hieraus ergibt sich die Möglichkeit, dass sich auch Beobachtungen des präleukämen Zustandes im Mausmodel auf die menschliche Situation übertragen lassen. Biologische Modelle für präleukäme Zustände sind selten aber wichtig in der Erforschung der Krankheitsursachen, da diese Zustände aufgrund ihrer subklinischen Effekte beim Menschen nicht entdeckt werden. Für die Untersuchung der Entstehung klonaler Hämatopoiese und das Nachvollziehen von somatischen Mutationen und deren

Auswirkungen werden somit auch in der Zukunft vor allem Tiermodelle herangezogen werden müssen. Hier bietet das beschriebene *Irf4*$^{-/-}$ Modell wichtige Ansatzpunkte.

Die Beschreibung und Untersuchung der wiederkehrenden JAK Mutationen als onkogene Treiber der beschriebenen Mausleukämie brachten die *Ph-like* Leukämie beim Menschen in den Fokus der Betrachtungen. Auch bei dieser Form der Leukämie sind Kinase-Alterationen, wie zum Beispiel Mutationen in Januskinasen häufig. Die *Ph-like* Leukämie wurde zunächst auf der Ebene von Transkriptom-Daten definiert als eine Leukämieform, die transkriptionell sehr ähnlich wie eine BCR-ABL tragende (Ph^{+}) Leukämie imponiert, selbst aber BCR-ABL negativ ist. Die Ursachen hierfür sind weiterhin unklar. Vermutet werden kann, dass BCR-ABL und die onkogenen Treiber der *Ph-like* Leukämie ähnliche Signalwege dominieren. Eine interessante und bislang wenig beachtete Hypothese ist aber auch die Möglichkeit, dass beide onkogenen Signale die Fixierung an der gleichen B-Zell Differenzierungsstufe bewirken. In diesem Licht ist es auffällig, dass die *Irf4*$^{-/-}$ Leukämien aus dem Differenzierungszustand der präB-I Zellen hervorgehen. Im Mausmodell wäre es daher von Interesse herauszufinden, welchen Differenzierungsstand eine Transformation von B Zell Vorläufern mit BCR-ABL konserviert. Die genannte zweite Hypothese würde zudem eine zentrale Rolle für IRF4 auch in der BCR-ABL induzierten BCP-ALL möglich machen, da zu untersuchen wäre, wie BCR-ABL der unter physiologischen Bedingungen durch IRF4 vermittelten Differenzierung entgegenwirkt.

In der Zusammenschau wird durch die vorliegende Arbeit ein wichtiges biologisches Modell der BCP-ALL charakterisiert und analysiert. Die Ergebnisse helfen einerseits dabei Aspekte der *Ph-like* ALL zu verstehen, werfen andererseits aber auch neue, allgemeinere Fragen zur BCP-ALL auf.

6. Zusammenfassung

6.1. Deutsch

Die Entwicklung der B-Zellen im Knochenmark erfolgt unter fein-dirigierter zell-intrinsischer und extrinsischer Kontrolle. Veränderungen dieser Kontrollmechanismen bergen die Gefahr einer Entartung von Stamm- und Progenitorzellen im Sinne einer akuten lymphoblastischen B Zell Progenitor Leukämie.

Ziel der vorliegenden Arbeit war es, die Ursachen einer spontan entstehenden leukämischen Erkrankung in *Irf4*$^{-/-}$ Mäusen zu charakterisieren. Zunächst wurden die präleukämischen Veränderungen der *Irf4*$^{-/-}$ B-Zell Entwicklung untersucht. Zentral zeigten sich eine eingeschränkte Differenzierung von Progenitorzellen jenseits des präBZR-checkpoints, sowie eine Reduktion der Knochen-marksadhärenz durch eingeschränkte Sensitivität für den chemotaktischen Faktor CXCL12. Zudem wurde die ektope Expression des mutagenen Enzymes AID beobachtet. *Irf4*$^{-/-}$ Leukämien zeichneten sich durch rekurrierende somatische *Jak3* Mutationen aus. Diese bewirkten eine erhöhte IL-7 Sensitivität, jedoch keine vollständige Zytokin-Unabhängigkeit der Leukämiezellen. Eine Behandlung von Mäusen mit *Irf4*$^{-/-}$ Leukämien mit dem JAK-Inhibitor Ruxolitinib ergab eine präferenzielle Wirkung auf die Infiltration von soliden Organen durch Leukämiezellen, ohne eine systemische Wirkung auf die Leukämielast im Blut oder im Knochenmark. Von translationaler Bedeutung ist hierbei die Verringerung einer meningeosis leukaemica, die sich klinisch an einer Reduktion von Lähmungssymptomen im Mausmodell zeigte.

Der Vergleich der so charakterisierten *Irf4*$^{-/-}$ Leukämie mit dem menschlichen Krankheitsspektrum ergab eine große Ähnlichkeit mit der BCP-ALL Subform der *Ph-like* ALL. Da bei dieser Erkrankung bislang wenig bekannt ist über die Pathomechanik ihrer Entstehung, sind die in der vorliegenden Arbeit dargelegten Hinweise aus dem Mausmodell von hoher Relevanz für das Krankheitsverständnis.

In einem zweiten Teil der Arbeit wurden Techniken der Transkriptionsfaktor-Überexpression genutzt, um durch Re-Expression von FoxP3 die Reversibilität verringerter suppressiver Kapazitäten von mutierten T_{regs} zu untersuchen.

6.2 Englisch

B cell development in the bone marrow is the result of a tightly regulated interplay of intrinsic and extrinsic control mechanisms. Disruptions in this system can give rise to the development of B cell progenitor acute lymphoblastic leukemia.

The aim of the present work was to characterise the causes of a spontaneous leukemic disease in *Irf4*$^{-/-}$ mice. To this end, preleukemic alterations in the B cell progeny of healthy *Irf4*$^{-/-}$ mice was investigated. Both an impaired differentiation beyond the preBCR checkpoint as well as reduced adhesion to the bone marrow niche as a result of decreased sensitivity to the chemotactic factor CXCL12 was observed. Both phenomena induced unchecked expression of the mutagenic enzyme AID. *Irf4*$^{-/-}$ leukemia was characterised by recurrent *Jak3* mutations, resulting in enhanced IL-7 sensitivity without granting complete cytokine independency to leukemia cells. Treating mice with established *Irf4*$^{-/-}$ leukemia with the JAK-inhibitor Ruxolitinib resulted in the preferential reduction of leukemia infiltration into solid organs without a systemic effect on the leukemic burden in peripheral blood or bone marrow. Especially the reduction in leukemic meningeosis marked by clinical reductions in paralysis symptoms, is to be noted as of high translational importance. Comparisons between the thus characterised *Irf4*$^{-/-}$ leukemia and the human disease spectrum yielded a striking resemblance to the Ph-like BCP-ALL entity. As, to this date, little is known about the causative pathomechanisms behind the disease, the insights portrayed in the present work might be of importance for our understanding of Ph-like BCP-ALL.

In parallel, techniques for the overexpression of transcription factors were employed to address the potential reversibility of decreased suppressive capacities observed in mutated T_{regs}.

7. Literaturverzeichnis

Acquaviva, J., Chen, X., and Ren, R. (2008). IRF-4 functions as a tumor suppressor in early B-cell development. Blood *112*, 3798–3806. https://doi.org/10.1182/blood-2007-10-117838.

Altevogt, P., Hubbe, M., Ruppert, M., Lohr, J., Hoegen, P. von, Sammar, M., Andrew, D.P., McEvoy, L., Humphries, M.J., and Butcher, E.C. (1995). The alpha 4 integrin chain is a ligand for alpha 4 beta 7 and alpha 4 beta 1. J Exp Medicine *182*, 345–355. https://doi.org/10.1084/jem.182.2.345.

Barata, J.T., Durum, S.K., and Seddon, B. (2019). Flip the coin: IL-7 and IL-7R in health and disease. Nat Immunol *20*, 1584–1593. https://doi.org/10.1038/s41590-019-0479-x.

Brüstle, A., Heink, S., Huber, M., Rosenplänter, C., Stadelmann, C., Yu, P., Arpaia, E., Mak, T.W., Kamradt, T., and Lohoff, M. (2007). The development of inflammatory TH-17 cells requires interferon-regulatory factor 4. Nat Immunol *8*, 958–966. https://doi.org/10.1038/ni1500.

Fistonich, C., Zehentmeier, S., Bednarski, J.J., Miao, R., Schjerven, H., Sleckman, B.P., and Pereira, J.P. (2018). Cell circuits between B cell progenitors and IL-7+ mesenchymal progenitor cells control B cell developmentCell circuits control B cell development. J Exp Medicine *215*, 2586–2599. https://doi.org/10.1084/jem.20180778.

Fontenot, J.D., and Rudensky, A.Y. (2005). A well adapted regulatory contrivance: regulatory T cell development and the forkhead family transcription factor Foxp3. Nat Immunol *6*, 331–337. https://doi.org/10.1038/ni1179.

Freeden-Jeffry, U. von, Vieira, P., Lucian, L.A., McNeil, T., Burdach, S.E., and Murray, R. (1995). Lymphopenia in interleukin (IL)-7 gene-deleted mice identifies IL-7 as a nonredundant cytokine. J Exp Medicine *181*, 1519–1526. https://doi.org/10.1084/jem.181.4.1519.

Fuxa, M., and Busslinger, M. (2007). Reporter Gene Insertions Reveal a Strictly B Lymphoid-Specific Expression Pattern of Pax5 in Support of Its B Cell Identity Function. J Immunol *178*, 3031–3037. https://doi.org/10.4049/jimmunol.178.5.3031.

Gambineri, E., Torgerson, T.R., and Ochs, H.D. (2003). Immune dysregulation, polyendocrinopathy, enteropathy, and X-linked inheritance (IPEX), a syndrome of systemic autoimmunity caused by mutations of FOXP3, a critical regulator of T-cell homeostasis. Curr Opin Rheumatol *15*, 430–435. https://doi.org/10.1097/00002281-200307000-00010.

Geier, J.K., and Schlissel, M.S. (2006). Pre-BCR signals and the control of Ig gene rearrangements. Semin Immunol *18*, 31–39. https://doi.org/10.1016/j.smim.2005.11.001.

Haan, C., Rolvering, C., Raulf, F., Kapp, M., Drückes, P., Thoma, G., Behrmann, I., and Zerwes, H.-G. (2011). Jak1 Has a Dominant Role over Jak3 in Signal Transduction through γc-Containing Cytokine Receptors. Chem Biol *18*, 314–323. https://doi.org/10.1016/j.chembiol.2011.01.012.

Hara, T., Shitara, S., Imai, K., Miyachi, H., Kitano, S., Yao, H., Tani-ichi, S., and Ikuta, K. (2012). Identification of IL-7–Producing Cells in Primary and Secondary Lymphoid Organs Using IL-7–GFP Knock-In Mice. J Immunol *189*, 1577–1584. https://doi.org/10.4049/jimmunol.1200586.

Hardy, R.R., and Hayakawa, K. (2001). B cell development pathways. Annu Rev Immunol *19*, 595–621. https://doi.org/10.1146/annurev.immunol.19.1.595.

Hardy, R.R., Carmack, C.E., Shinton, S.A., Kemp, J.D., and Hayakawa, K. (1991). Resolution and characterization of pro-B and pre-pro-B cell stages in normal mouse bone marrow. J Exp Medicine *173*, 1213–1225. https://doi.org/10.1084/jem.173.5.1213.

Herold, T., Schneider, S., Metzeler, K., Neumann, M., Hartmann, L., Roberts, K.G., Konstandin, N.P., Greif, P.A., Bräundl, K., Ksienzyk, B., et al. (2016). Philadelphia chromosome-like acute lymphoblastic leukemia in adults have frequent IGH-CRLF2 and JAK2 mutations, persistence of minimal residual disease and poor prognosis. Haematologica *102*, haematol.2015.136366. https://doi.org/10.3324/haematol.2015.136366.

Huber, M., and Lohoff, M. (2014). IRF4 at the crossroads of effector T-cell fate decision. Eur J Immunol *44*, 1886–1895. https://doi.org/10.1002/eji.201344279.

Johnson, K., Hashimshony, T., Sawai, C.M., Pongubala, J.M.R., Skok, J.A., Aifantis, I., and Singh, H. (2008). Regulation of immunoglobulin light-chain recombination by the transcription factor IRF-4 and the attenuation of interleukin-7 signaling. Immunity *28*, 335–345. https://doi.org/10.1016/j.immuni.2007.12.019.

Jumper, J., Evans, R., Pritzel, A., Green, T., Figurnov, M., Ronneberger, O., Tunyasuvunakool, K., Bates, R., Žídek, A., Potapenko, A., et al. (2021). Highly accurate protein structure prediction with AlphaFold. Nature *596*, 583–589. https://doi.org/10.1038/s41586-021-03819-2.

Katz, A.J., Chia, V.M., Schoonen, W.M., and Kelsh, M.A. (2015). Acute lymphoblastic leukemia: an assessment of international incidence, survival, and disease burden. Cancer Cause Control *26*, 1627–1642. https://doi.org/10.1007/s10552-015-0657-6.

Kawamoto, T. (2003). Use of a new adhesive film for the preparation of multi-purpose fresh-frozen sections from hard tissues, whole-animals, insects and plants. Arch Histol Cytol *66*, 123–143. https://doi.org/10.1679/aohc.66.123.

Krishnan, S., Wade, R., Moorman, A.V., Mitchell, C., Kinsey, S.E., Eden, T.O.B., Parker, C., Vora, A., Richards, S., and Saha, V. (2010). Temporal changes in the incidence and pattern of central nervous system relapses in children with acute lymphoblastic leukaemia treated on four consecutive Medical Research Council trials, 1985–2001. Leukemia *24*, 450–459. https://doi.org/10.1038/leu.2009.264.

Li, J.-F., Dai, Y.-T., Lilljebjörn, H., Shen, S.-H., Cui, B.-W., Bai, L., Liu, Y.-F., Qian, M.-X., Kubota, Y., Kiyoi, H., et al. (2018). Transcriptional landscape of B cell precursor acute lymphoblastic leukemia based on an international study of 1,223 cases. Proc National Acad Sci *115*, 201814397. https://doi.org/10.1073/pnas.1814397115.

Li, P., Spolski, R., Liao, W., Wang, L., Murphy, T.L., Murphy, K.M., and Leonard, W.J. (2012). BATF–JUN is critical for IRF4-mediated transcription in T cells. Nature *490*, 543–546. https://doi.org/10.1038/nature11530.

Lim, V.Y., Zehentmeier, S., Fistonich, C., and Pereira, J.P. (2017). A Chemoattractant-Guided Walk Through Lymphopoiesis From Hematopoietic Stem Cells to Mature B Lymphocytes. Adv Immunol *134*, 47–88. https://doi.org/10.1016/bs.ai.2017.02.001.

Lohoff, M., and Mak, T.W. (2005). Roles of interferon-regulatory factors in T-helper-cell differentiation. Nat Rev Immunol *5*, 125–135. https://doi.org/10.1038/nri1552.

Lohoff, M., Mittrücker, H.-W., Prechtl, S., Bischof, S., Sommer, F., Kock, S., Ferrick, D.A., Duncan, G.S., Gessner, A., and Mak, T.W. (2002). Dysregulated T helper cell differentiation in the absence of interferon regulatory factor 4. Proc National Acad Sci *99*, 11808–11812. https://doi.org/10.1073/pnas.182425099.

Longo, D.L., Hunger, S.P., and Mullighan, C.G. (2015). Acute Lymphoblastic Leukemia in Children. New Engl J Medicine *373*, 1541–1552. https://doi.org/10.1056/nejmra1400972.

Lu, R. (2008). Interferon regulatory factor 4 and 8 in B-cell development. Trends Immunol *29*, 487–492. https://doi.org/10.1016/j.it.2008.07.006.

Lu, R., Medina, K.L., Lancki, D.W., and Singh, H. (2003). IRF-4,8 orchestrate the pre-B-to-B transition in lymphocyte development. Gene Dev *17*, 1703–1708. https://doi.org/10.1101/gad.1104803.

Lupardus, P.J., Ultsch, M., Wallweber, H., Kohli, P.B., Johnson, A.R., and Eigenbrot, C. (2014). Structure of the pseudokinase–kinase domains from protein kinase TYK2 reveals a mechanism for Janus kinase (JAK) autoinhibition. Proc National Acad Sci *111*, 8025–8030. https://doi.org/10.1073/pnas.1401180111.

Ma, S., Turetsky, A., Trinh, L., and Lu, R. (2006). IFN Regulatory Factor 4 and 8 Promote Ig Light Chain κ Locus Activation in Pre-B Cell Development. J Immunol *177*, 7898–7904. https://doi.org/10.4049/jimmunol.177.11.7898.

Malard, F., and Mohty, M. (2020). Acute lymphoblastic leukaemia. Lancet *395*, 1146–1162. https://doi.org/10.1016/s0140-6736(19)33018-1.

Mårtensson, I.-L., Almqvist, N., Grimsholm, O., and Bernardi, A.I. (2010). The pre-B cell receptor checkpoint. Febs Lett *584*, 2572–2579. https://doi.org/10.1016/j.febslet.2010.04.057.

McElroy, C.A., Holland, P.J., Zhao, P., Lim, J.-M., Wells, L., Eisenstein, E., and Walsh, S.T.R. (2012). Structural reorganization of the interleukin-7 signaling complex. Proc National Acad Sci *109*, 2503–2508. https://doi.org/10.1073/pnas.1116582109.

Milford, T.M., Su, R.J., Francis, O.L., Baez, I., Martinez, S.R., Coats, J.S., Weldon, A.J., Calderon, M.N., Nwosu, M.C., Botimer, A.R., et al. (2016). TSLP or IL-7 provide an IL-7Rα signal that is critical for human B lymphopoiesis. Eur J Immunol *46*, 2155–2161. https://doi.org/10.1002/eji.201646307.

Mittrücker, H.-W., Matsuyama, T., Grossman, A., Kündig, T.M., Potter, J., Shahinian, A., Wakeham, A., Patterson, B., Ohashi, P.S., and Mak, T.W. (1997). Requirement for the Transcription Factor LSIRF/IRF4 for Mature B and T Lymphocyte Function. Science *275*, 540–543. https://doi.org/10.1126/science.275.5299.540.

Mullighan, C.G., Su, X., Zhang, J., Radtke, I., Phillips, L.A.A., Miller, C.B., Ma, J., Liu, W., Cheng, C., Schulman, B.A., et al. (2009). Deletion of IKZF1 and Prognosis in Acute Lymphoblastic Leukemia. New Engl J Medicine *360*, 470–480. https://doi.org/10.1056/nejmoa0808253.

Noia, J.D., and Neuberger, M.S. (2002). Altering the pathway of immunoglobulin hypermutation by inhibiting uracil-DNA glycosylase. Nature *419*, 43–48. https://doi.org/10.1038/nature00981.

Ohnishi, K., and Melchers, F. (2003). The nonimmunoglobulin portion of λ5 mediates cell-autonomous pre-B cell receptor signaling. Nat Immunol *4*, 849–856. https://doi.org/10.1038/ni959.

Osmond, D.G., Rolink, A., and Melchers, F. (1998). Murine B lymphopoiesis: towards a unified model. Immunol Today *19*, 65–68. https://doi.org/10.1016/s0167-5699(97)01203-6.

Pang, S.H.M., Minnich, M., Gangatirkar, P., Zheng, Z., Ebert, A., Song, G., Dickins, R.A., Corcoran, L.M., Mullighan, C.G., Busslinger, M., et al. (2016). PU.1 cooperates with IRF4 and IRF8 to suppress pre-B-cell leukemia. Leukemia *30*, 1375–1387. https://doi.org/10.1038/leu.2016.27.

Park, L.S., Martin, U., Garka, K., Gliniak, B., Santo, J.P.D., Muller, W., Largaespada, D.A., Copeland, N.G., Jenkins, N.A., Farr, A.G., et al. (2000). Cloning of the Murine Thymic Stromal Lymphopoietin (Tslp) ReceptorFormation of a Functional Heteromeric Complex Requires Interleukin 7 Receptor. J Exp Medicine *192*, 659–670. https://doi.org/10.1084/jem.192.5.659.

Peschon, J.J., Morrissey, P.J., Grabstein, K.H., Ramsdell, F.J., Maraskovsky, E., Gliniak, B.C., Park, L.S., Ziegler, S.F., Williams, D.E., Ware, C.B., et al. (1994). Early lymphocyte expansion is severely impaired in interleukin 7 receptor-deficient mice. J Exp Medicine *180*, 1955–1960. https://doi.org/10.1084/jem.180.5.1955.

Petersen-Mahrt, S.K., Harris, R.S., and Neuberger, M.S. (2002). AID mutates E. coli suggesting a DNA deamination mechanism for antibody diversification. Nature *418*, 99–104. https://doi.org/10.1038/nature00862.

Puel, A., Ziegler, S.F., Buckley, R.H., and Leonard., W.J. (1998). Defective IL7R expression in T-B+NK+ severe combined immunodeficiency. Nat Genet *20*, 394–397. https://doi.org/10.1038/3877.

Roberts, K.G. (2018). Genetics and prognosis of ALL in children vs adults. Hematology Am Soc Hematology Educ Program *2018*, 137–145. https://doi.org/10.1182/asheducation-2018.1.137.

Roberts, K.G., Li, Y., Payne-Turner, D., Harvey, R.C., Yang, Y.-L., Pei, D., McCastlain, K., Ding, L., Lu, C., Song, G., et al. (2014). Targetable kinase-activating lesions in Ph-like acute lymphoblastic leukemia. New Engl J Medicine *371*, 1005–1015. https://doi.org/10.1056/nejmoa1403088.

Roberts, K.G., Yang, Y.-L., Payne-Turner, D., Lin, W., Files, J.K., Dickerson, K., Gu, Z., Taunton, J., Janke, L.J., Chen, T., et al. (2017). Oncogenic role and therapeutic targeting of ABL-class and JAK-STAT activating kinase alterations in Ph-like ALL. Blood Adv *1*, 1657–1671. https://doi.org/10.1182/bloodadvances.2017011296.

Schebesta, A., McManus, S., Salvagiotto, G., Delogu, A., Busslinger, G.A., and Busslinger, M. (2007). Transcription Factor Pax5 Activates the Chromatin of Key Genes Involved in B Cell Signaling, Adhesion, Migration, and Immune Function. Immunity *27*, 49–63. https://doi.org/10.1016/j.immuni.2007.05.019.

Shevach, E.M. (2009). Mechanisms of Foxp3+ T Regulatory Cell-Mediated Suppression. Immunity *30*, 636–645. https://doi.org/10.1016/j.immuni.2009.04.010.

Shukla, V., and Lu, R. (2014). IRF4 and IRF8: governing the virtues of B lymphocytes. Frontiers Biology *9*, 269–282. https://doi.org/10.1007/s11515-014-1318-y.

Swaminathan, S., Klemm, L., Park, E., Papaemmanuil, E., Ford, A., Kweon, S.-M., Trageser, D., Hasselfeld, B., Henke, N., Mooster, J., et al. (2015). Mechanisms of clonal evolution in childhood acute lymphoblastic leukemia. Nat Immunol *16*, 766–774. https://doi.org/10.1038/ni.3160.

Tasian, S.K., Loh, M.L., and Hunger, S.P. (2017). Philadelphia chromosome–like acute lymphoblastic leukemia. Blood *130*, 2064–2072. https://doi.org/10.1182/blood-2017-06-743252.

Thévenin, C., Nutt, S.L., and Busslinger, M. (1998). Early Function of Pax5 (BSAP) before the Pre-B Cell Receptor Stage of B Lymphopoiesis. J Exp Medicine *188*, 735–744. https://doi.org/10.1084/jem.188.4.735.

Tokoyoda, K., Egawa, T., Sugiyama, T., Choi, B.-I., and Nagasawa, T. (2004). Cellular Niches Controlling B Lymphocyte Behavior within Bone Marrow during Development. Immunity *20*, 707–718. https://doi.org/10.1016/j.immuni.2004.05.001.

Varadi, M., Anyango, S., Deshpande, M., Nair, S., Natassia, C., Yordanova, G., Yuan, D., Stroe, O., Wood, G., Laydon, A., et al. (2021). AlphaFold Protein Structure Database: massively expanding the structural coverage of protein-sequence space with high-accuracy models. Nucleic Acids Res https://doi.org/10.1093/nar/gkab1061.

Verstovsek, S., Mesa, R.A., Gotlib, J., Levy, R.S., Gupta, V., DiPersio, J.F., Catalano, J.V., Deininger, M., Miller, C., Silver, R.T., et al. (2012). A double-blind, placebo-controlled trial of ruxolitinib for myelofibrosis. New Engl J Medicine *366*, 799–807. https://doi.org/10.1056/nejmoa1110557.

Vettermann, C., Herrmann, K., and Jäck, H.-M. (2006). Powered by pairing: The surrogate light chain amplifies immunoglobulin heavy chain signaling and pre-selects the antibody repertoire. Semin Immunol *18*, 44–55. https://doi.org/10.1016/j.smim.2006.01.001.

Vicente-Dueñas, C., Janssen, S., Oldenburg, M., Auer, F., González-Herrero, I., Casado-García, A., Isidro-Hernández, M., Raboso-Gallego, J., Westhoff, P., Pandyra, A.A., et al. (2020). An intact gut microbiome protects genetically predisposed mice against leukemia. Blood *136*, 2003–2017. https://doi.org/10.1182/blood.2019004381.

Wei, C., Zeff, R., and Goldschneider, I. (2000). Murine Pro-B Cells Require IL-7 and Its Receptor Complex to Up-Regulate IL-7Rα, Terminal Deoxynucleotidyltransferase, and cμ Expression. J Immunol *164*, 1961–1970. https://doi.org/10.4049/jimmunol.164.4.1961.

Zheng, Y., Chaudhry, A., Kas, A., deRoos, P., Kim, J.M., Chu, T.-T., Corcoran, L., Treuting, P., Klein, U., and Rudensky, A.Y. (2009). Regulatory T-cell suppressor program co-opts transcription factor IRF4 to control TH2 responses. Nature *458*, 351–356. https://doi.org/10.1038/nature07674.

8. Anhang

8.1 Lebenslauf

Dennis Das Gupta

geb. 20.03.1996
Bismarckstr. 30, 35037 Marburg

+49 1573 2237652 • dennisdasgupta@icloud.com

Arbeitserfahrung

seit Feb. 2021	**Wissenschaftlicher Mitarbeiter** Institut für Medizinische Mikrobiologie und Krankenhaushygiene Philipps-Universität • Marburg • Projektstelle zur Erforschung von präleukämischen B-Zell Alterationen im Mausmodell anhand zu etablierender Labormethoden wie der *in situ* Fluoreszenz-Mikroskopie von murinem Knochenmark • Laborbetreuung einer medizinischen Promotionsarbeit

Ausbildung

seit 10/2017	**Promotion** Institut für Medizinische Mikrobiologie und Krankenhaushygiene Philipps-Universität • Marburg • Titel: „Die Bedeutung des Transkriptionsfaktors IRF4 und des IL-7 Signalweges in der Entstehung von präB-Zell Leukämien der Maus“ • Doktorvater: Prof. M. Lohoff • Mildred-Scheel Stipendium der Deutschen Krebshilfe • FELASA Tierversuchskunde • Dissertation und Disputation ausstehend

10/2013 – 12/2020	**Studium der Humanmedizin**
	Medizinische Fakultät, Philipps-Universität • Marburg
	• Gesamtnote: sehr gut (1,33) – M1 sehr gut, M2 gut, M3 sehr gut
	• Praktisches Jahr:
	  • Anästhesie: Charité Campus Mitte Berlin (*Prof. C. Spies*)
	  • Innere Medizin: RdI TU München (*Prof. R. M. Schmid, Prof. F. Bassermann*)
	  • Chirurgie: Uniklinikum Marburg (*Prof. D. K. Bartsch, Prof. S. Ruchholtz*)

08/2005 – 07/2013	**Abitur** Arndt-Gymnasium, Krefeld (heute Arendt-Gymnasium)

Lehre und Engagement

2018	**Studentisches Mitglied Fachbereichsrat** Medizinische Fakultät, Philipps-Universität • Marburg
2015 – 2017	**Studentischer Tutor** Institut für Physiologische Chemie, Philipps-Universität • Marburg • Leitung einer Vorlesungsreihe zur M1-Vorbereitung • Preis der Lehre des Fachbereichs

Auslandserfahrung

2018 (4 Wochen)	**Famulatur** Princess Margaret Cancer Centre, UHN Toronto (*Dr. Cescon, Dr. Bedard*)
2016 (4 Wochen)	**Famulatur** St. Francis Buluba Hospital, Uganda

Veröffentlichungen

2020	Kurniawan, H., Franchina, D. G., Guerra, L., Bonetti, L., Baguet, L. S.-, Grusdat, M., Schlicker, L., Hunewald, O., Dostert, C., Merz, M. P., Binsfeld, C., Duncan, G. S., Farinelle, S., Nonnenmacher, Y., Haight, J., **Das Gupta, D.**, Ewen, A., Taskesen, R., Halder, R., Chen, Y., Jäger, C., Ollert, M., Wilmes, P., Vasiliou, V., Harris, I. S., Knobbe-Thomsen, C. B., Turner, J. D., Mak, T. W., Lohoff, M., Meiser, J., Hiller, K. & Brenner, D. Glutathione Restricts Serine Metabolism to Preserve Regulatory T Cell Function. *Cell Metab* 31, 920-936.e7 (2020).
2022	Romeo-Olmedo, A.J., Schulz, A.R., Hochstätter, S., **Das Gupta, D.**, Virta, I., Hirseland, H., Staudenraus, D., Camara, B., Münch, C., Hefter, V., Sapre, S., Krähling, V., Müller-Kräuter, H., Widera, M., Mei, H.E., Keller, C., Lohoff, M. Induction of robust cellular and humoral immunity against SARS-CoV-2 after a third dose of BNT162b2 vaccine in previously unresponsive older adults. *Nat Microbiol* 7, 195–199 (2022).
	Das Gupta, D., Paul, C., Samel, N., Bieringer, M., Staudenraus, D., Marini, F., Raifer, H., Hansal, L., Menke, L., Camara, B., Roth, E., Daum, P., Wanzel, M., Mernberger, M., Nist, A., Bauer, U.-M., Helmprobst, F., Buchholz, M., Roth, K., Bastian, L., Hartman, A.M., Baldus, C., Ikuta, K., Neubauer, A., Burchert, Jäck, H.-M., A., Klein, M., Bopp, T., Stiewe, T., Pagenstecher, A. & Lohoff, M. IRF4 deficiency vulnerates B cell progeny for leukemogenesis via somatically acquired *Jak3* mutations conferring IL-7 hypersensitivity. *Cell Death Differ* 1–14 (2022) doi:10.1038/s41418-022-01005-z.

Auszeichnungen und Stipendien

2019	Ettal Spring School of Immunology Posterpreise • 1. Preis Teilnehmerjury • 1. Preis Professorenjury
2018	Deutschlandstipendium
2016	Mildred Scheel Doktoranden Stipendium der Deutschen Krebshilfe
	Reisestipendium des Alumni Marburg e.V.
	Preis für hervorragende Lehre am Fachbereich Medizin Vorlesungen in Biochemie

Sonstiges

Sprachen
Deutsch (Muttersprache), Englisch (fließend), Französisch (gut)

Skills
Labor (Zellkultur, primäre Immunzellen, in vivo Mausexperimente, FACS, Mikroskopie, Molekularbiologie), R

Interessen
Lesen, Wandern, Klettern, Kultur, analoge Fotografie

8.2 Verzeichnis der akademischen Lehrer:innen

Meine akademischen Lehrenden waren in Marburg:

Adamkiewicz
Barth
Bartsch
Bauer
Baum
Bäumlein
Becker A.
Becker K.
Becker S.
Best
Bette
Bien
Bliemel
Bonaterra
Bösner
Brehm
Bücking
Carl
Cetin
Czubayko
Daut
Decher
Del Rey
Dettmeyer
Dietz
Dinges
Donner-Banzhoff
Duda
Eberhart
Eggers
El-Zayat
Engenhart-Cabillic
Eschbach
Eubel
Fendrich
Feuser
Figiel
Frink
Fritz
Fuchs-Winkelmann
Geks
Geraedts
Görg
Gress
Grgic
Grimm
Grundmann
Haas
Halaszovich
Hertl
Hildebrandt
Hoch
Hofmann
Hoyer
Irqsusi
Jerrentrup
Josephs
Kalder
Kann
Kanngießer
Karatolios
Kill
Kinscherf
Kircher
Kirschbaum
Kluge
Kolb-Niemann
Kortus-Götze
Kostev
Köhler
König
Kruse
Kühnert
Lechler
Leonhardt
Lill
Lohoff
Mahnken
Maier
Meißner
Menzler
Meyer
Meyer-Wittkopf
Milani
Mittag
Moll
Morin
Mueller
Mutters
Nenadic
Neubauer
Neumüller Nikolaizik
Nimsky
Nockher
Oberkircher
Oberwinkler
Oertel
Oliver
Opitz
Pagenstecher
Pankuweit
Parahuleva
Patrascan
Peterlein
Pfestroff
Pfützner
Plant
Preisig-Müller
Reese
Renz
Richter
Rinne
Rißе
Roelcke
Roeßler
Rost
Ruchholtz
Sahmland
Schäfer
Schieffer
Schierl
Schneider
Schoner
Schratt
Schu
Schütz
Schulze
Schütt
Schüttler
Schwalbe
Seifart
Seitz
Sekundo
Sevinc
Sommer
Stahl
Steinfeldt
Steiniger
Strik
Stuck
Tackenberg
Teymoortash
Thieme
Thum
Timmermann
Timmesfeld
Vannucchi
Vogelmeier
Vogt
Vorwerk
Wagner
Walter
Weber
Weihe
Westermann
Wiesmann
Wilhelm
Wißniowski
Wolff
Worzfeld
Wrocklage
Wulf
Zavorotny
Ziring
Zwiorek

8.3 Danksagung

Für die vorliegende Arbeit gebührt mein Dank zahlreichen Menschen, die mich über die Dauer der Promotionsarbeit maßgeblich geprägt und unterstützt haben. Im Institut für medizinische Mikrobiologie war dies allen voran Prof. Dr. Michael Lohoff, der mit seiner besonders herzlich-stoischen Art zu einem wichtigen Mentor und Freund für mich geworden ist. Die Art meines wissenschaftlichen Denkens und die Präzision meiner Arbeit sind direktes Produkt seiner intensiven Förderung. Prof. Dr. Ulrich Steinhof, Prof. Dr. Magdalena Huber und Prof. Dr. Alexander Visekruna möchte ich zudem für zahlreiche freundschaftliche und wissenschaftlich-kritische Gespräche danken. Das Institut konnte ich dank ihnen als einen kreativen und produktiv chaotischen Ort schätzen lernen.

Über die Jahre haben mich zudem unzählige Kolleg:innen begleitet, die unentwegt weitere Puzzleteile für diese Geschichte beigetragen haben. Martin Müller hat mich überhaupt erst in das Labor geführt, Dr. Dr. Olaf Pinkenburg hat mich molekularbiologisch ausgebildet, Dr. Maik Luu hat mich über lange Strecken intensiv fachlich und technisch unterstützt. Dr. Lucia Campos-Carrascosa, Rossana Romero, Manuel Gerlach, Daniel Staudenraus, Hanna Leister und viele mehr haben zu einem wirklich inspirierenden Umfeld beigetragen und die Zeit für mich zu einer tief prägenden gemacht.

Finanziell haben die Deutsche Krebshilfe und das Deutschlandstipendium meine beiden Freisemester ermöglicht und die nötige Freiheit geschaffen, mit der ich meine Forschung produktiv vorantreiben konnte.

Danken möchte ich zuletzt noch meinen engsten Vertrauten, die mich durch alle Höhen und Tiefen der Promotion begleitet haben. Meine Eltern haben mir viel Freiraum gelassen und meinen Weg duldsam mitgetragen. Dorothea Daiminger war und ist eine besondere Inspiration und ein Vorbild für Schärfe und Kompromisslosigkeit an den richtigen Stellen. Till Bedau und Aaron Grahl waren immer zur Stelle mit offenen Ohren, Pétanque-Partien, Urlauben zum Präfrontalkortex-Defragmentieren und künstlerischem Ausgleich. Auf Eure Freundschaft konnte ich immer bauen.

8.4 Ehrenwörtliche Erklärung

Ich ekläre ehrenwörtlich, dass ich die dem Fachbereich Medizin Marburg zur Promotionsprüfung eingereichte Arbeit mit dem Titel „Die Bedeutung des Lymphozyten-Transkriptionsfaktors IRF4 in der Entstehung von präB Zell Leukämien der Maus“ im Institut für Medizinische Mikrobiologie und Krankenhaushygiene unter Leitung von Prof. Dr. Michael Lohoff mit Unterstützung durch die auf den aufgeführten Publikationen als Co-Autor:innen genannten Kooperationspartner:innen ohne sonstige Hilfe selbst durchgeführt und bei der Abfassung der Arbeit keine anderen als die in der Dissertation aufgeführten Hilfsmittel benutzt habe. Ich habe bisher an keinem in- oder ausländischen Medizinischen Fachbereich ein Gesuch um Zulassung zur Promotion eingereicht, noch die vorliegende oder eine andere Arbeit als Dissertation vorgelegt.

Ich versichere, dass ich sämtliche wörtlichen oder sinngemäßen Übernahmen und Zitate kenntlich gemacht habe.

Mit dem Einsatz von Software zur Erkennung von Plagiaten bin ich einverstanden.

Vorliegende Arbeit wurde (oder wird) in folgenden Publikationsorganen *„Cell Death and Differentiation“, „Cell Metabolism“, „Lancet Infectious Diseases“, „Nature Microbiology“* veröffentlicht:

Das Gupta, D. *et al.* IRF4 deficiency vulnerates B-cell progeny for leukemogenesis via somatically acquired Jak3 mutations conferring IL-7 hypersensitivity. *Cell Death Differ* 1–14 (2022) doi:10.1038/s41418-022-01005-z.

Kurniawan, H. *et al.* Glutathione Restricts Serine Metabolism to Preserve Regulatory T Cell Function. *Cell Metab* **31**, 920-936.e7 (2020).

Romero-Olmedo, A. J. *et al.* Induction of robust cellular and humoral immunity against SARS-CoV-2 after a third dose of BNT162b2 vaccine in previously unresponsive older adults. *Nat Microbiol* **7**, 195–199 (2022).

Romero-Olmedo, A. J. *et al.* Dynamics of humoral and T-cell immunity after three BNT162b2 vaccinations in adults older than 80 years. *Lancet Infect Dis* (2022) doi:10.1016/s1473-3099(22)00219-5.

Ort, Datum, Unterschrift Doktorandin/Doktorand

„Die Hinweise zur Erkennung von Plagiaten habe ich zur Kenntnis genommen."
Ort, Datum, Unterschrift Referentin/Referent

---

9. In dieser Arbeit beschriebene Originalarbeiten

Das Gupta, D. *et al.* IRF4 deficiency vulnerates B-cell progeny for leukemogenesis via somatically acquired Jak3 mutations conferring IL-7 hypersensitivity. *Cell Death Differ* 1–14 (2022) doi:10.1038/s41418-022-01005-z.

Kurniawan, H. *et al.* Glutathione Restricts Serine Metabolism to Preserve Regulatory T Cell Function. *Cell Metab* **31**, 920-936.e7 (2020).

Romero-Olmedo, A. J. *et al.* Induction of robust cellular and humoral immunity against SARS-CoV-2 after a third dose of BNT162b2 vaccine in previously unresponsive older adults. *Nat Microbiol* **7**, 195–199 (2022).

Romero-Olmedo, A. J. *et al.* Dynamics of humoral and T-cell immunity after three BNT162b2 vaccinations in adults older than 80 years. *Lancet Infect Dis* (2022) doi:10.1016/s1473-3099(22)00219-5.

CDDpress

www.nature.com/cdd

ARTICLE OPEN

IRF4 deficiency vulnerates B-cell progeny for leukemogenesis via somatically acquired *Jak3* mutations conferring IL-7 hypersensitivity

Dennis Das Gupta[1], Christoph Paul[2], Nadine Samel[1,3], Maria Bieringer[1], Daniel Staudenraus[1], Federico Marini[4], Hartmann Raifer[1], Lisa Menke[1], Lea Hansal[1], Bärbel Camara[1], Edith Roth[5], Patrick Daum[5], Michael Wanzel[6], Marco Mernberger[6,7], Andrea Nist[6], Uta-Maria Bauer[6], Frederik Helmprobst[8,9], Malte Buchholz[10], Katrin Roth[11], Lorenz Bastian[12], Alina M. Hartmann[12], Claudia Baldus[12], Koichi Ikuta[13], Andreas Neubauer[14], Andreas Burchert[14], Hans-Martin Jäck[5], Matthias Klein[15], Tobias Bopp[15,16], Thorsten Stiewe[6,7], Axel Pagenstecher[8,9] and Michael Lohoff[1]✉

The processes leading from disturbed B-cell development to adult B-cell progenitor acute lymphoblastic leukemia (BCP-ALL) remain poorly understood. Here, we describe *Irf4*$^{-/-}$ mice as prone to developing BCP-ALL with age. *Irf4*$^{-/-}$ preB-I cells exhibited impaired differentiation but enhanced proliferation in response to IL-7, along with reduced retention in the IL-7 providing bone marrow niche due to decreased CXCL12 responsiveness. Thus selected, preB-I cells acquired *Jak3* mutations, probably following irregular AID activity, resulting in malignant transformation. We demonstrate heightened IL-7 sensitivity due to *Jak3* mutants, devise a model to explain it, and describe structural and functional similarities to *Jak2* mutations often occurring in human Ph-like ALL. Finally, targeting JAK signaling with Ruxolitinib in vivo prolonged survival of mice bearing established *Irf4*$^{-/-}$ leukemia. Intriguingly, organ infiltration including leukemic meningeosis was selectively reduced without affecting blood blast counts. In this work, we present spontaneous leukemogenesis following IRF4 deficiency with potential implications for high-risk BCP-ALL in adult humans.

Cell Death & Differentiation; https://doi.org/10.1038/s41418-022-01005-z

INTRODUCTION

Two signaling pathways via the Interleukin-7 receptor (IL-7R) and the preB cell receptor (preBCR) ensure an orderly progression of B lymphopoiesis [1–3]. ProB cells adhere to bone marrow (BM) stromal cells (SCs) expressing CXCL12 and VCAM-1 through CXCR4 and VLA-4 respectively, while SC-derived IL-7 induces their proliferation [4]. The formation of the preBCR composed of Igμ protein and the surrogate light chain (ψL), consisting of λ5 and VPREB, marks the entrance to the preB cell stage. Signaling via the preBCR in turn induces the transcription factor (TF) interferon regulatory factor 4 (IRF4) which is also critical during T-cell differentiation [5, 6]. In preB cells, IRF4 halts cycling and facilitates recombination of the light chain locus by RAG1/2 [1]. Despite its importance, *Irf4*$^{-/-}$ mice still develop, albeit less, surface (s)Igμ^{+} mature B cells [7], likely due to a partially redundant function of IRF8. Accordingly, *Irf4,8*$^{-/-}$ B progenitors are completely arrested at the preB cell stage [8].

Disruption of this developmental track can provoke B-cell progenitor acute lymphoblastic leukemia (BCP-ALL). In humans, this disease preferentially affects children (age 0–19), while most deaths however occur in the adult population [9]. Cases affecting adolescents and young adults (AYA) display a different set of driver mutations compared to childhood BCP-ALL [10–13].

Herein, we report that adult *Irf4*$^{-/-}$ mice spontaneously develop BCP-ALL with age and delineate the steps from disturbed *Irf4*$^{-/-}$ B lymphopoiesis to overt leukemia.

[1]Institute for med. Microbiology & Hospital Hygiene, Philipps University Marburg, Marburg, Germany. [2]University Hospital Gießen and Marburg, Dept. of Ophthalmology, Philipps University Marburg, Marburg, Germany. [3]MVZ for Laboratory Medicine and Microbiology, Koblenz-Mittelrhein, Germany. [4]Institute of Medical Biostatistics, Epidemiology and Informatics (IMBEI), University Medical Center of the Johannes Gutenberg-University Mainz, Mainz, Germany. [5]Division of Molecular Immunology, Nikolaus-Fiebiger Center, University of Erlangen-Nürnberg, Erlangen, Germany. [6]Institute for Molecular Biology and Tumor Research (IMT), Center for Tumor- and Immunobiology (ZTI), Philipps University Marburg, Marburg, Germany. [7]Genomics Core Facility, Philipps University Marburg, Marburg, Germany. [8]Core Facility for Mouse Pathology and Electron Microscopy, Philipps University Marburg, Marburg, Germany. [9]University Hospital Gießen and Marburg, and Philipps University, Institute of Neuropathology, Marburg, Germany. [10]University Hospital Gießen and Marburg, and Philipps University, Clinic for Gastroenterology and Core Facility Small Animal Ultrasound, Marburg, Germany. [11]Core facility for Cellular Imaging, Philipps University Marburg, Marburg, Germany. [12]Medical Department II, Hematology and Oncology, University Medical Center Schleswig- Holstein, Kiel, Germany. [13]Institute for Frontier Life and Medical Sciences, Kyoto University, Kyoto, Japan. [14]University Hospital Gießen and Marburg, and Philipps University, Dept. Hematology, Oncology and Immunology, Marburg, Germany. [15]Institute for Immunology, Research Center for Immunotherapy (FZI), University Cancer Center, University Medical Center of the Johannes Gutenberg-University Mainz, Mainz, Germany. [16]German Cancer Consortium (DKTK), Mainz, Germany. ✉email: lohoff@med.uni-marburg.de

Edited by T Mak

Received: 7 February 2022 Revised: 7 April 2022 Accepted: 8 April 2022
Published online: 22 April 2022

RESULTS

Irf4$^{-/-}$ mice spontaneously develop preB cell leukemia

Following the serendipitous finding, that some aged *Irf4*$^{-/-}$ mice developed tumors and died, we systematically observed 80 *Irf4*$^{-/-}$ mice over time. We detected 14 tumors (incidence 17.5%), that spontaneously appeared in lymph node (LN) areas (mean age: 268d, median: 238d, Fig. 1a). Tumors were neither detected in mice younger than 150d nor in C57BL/6 wild-type (wt) mice housed in the same room.

All tumors (Fig. 1b shows a representative tumor in situ) were accompanied by lymphadenopathy (arrowheads) and increased spleen size (Fig. 1c). The suspected lymphomatous origin was corroborated microscopically (Fig. 1b, right panels), with infiltration of mononucleated cells into the BM, lung, and liver (Fig. 1d). Due to the known impaired maturation of *Irf4*$^{-/-}$ preB cells [7], spontaneous eruption of preB-leukemia seemed plausible: In spleen sections (Fig. 1e), infiltrating cells stained positive for both B220 and Igμ (although less than untransformed "follicle" B cells) and Ki67. By flow cytometry, BM samples from tumor mice harbored an expanded pro/preB cell compartment (Hardy fraction (fr.)A-D [14], B220^{mid}sIgμ^{-}) (Fig. 1f, g). Fr.A-D cells were detected also in peripheral lymphoid organs and blood of tumor mice (Fig. 1h). Following the Hardy classification (Fig. 1i), we determined tumor cells to be fr.C preB cells (B220^{mid}sIgμ^{-}CD43^{+}CD24^{+}BP-1^{+}) (Fig. 1j, k, sFig. 1a). In addition, Igμ, but not Igκ/λ was detected intracellularly (sFig. 1b). Lastly, tumors stained positive for surface λ5, part of the ψL (Fig. 1l). These attributes characterize the disease as preB-I cell BCP-ALL.

To prove clonality, we sequenced the VDJ junctions of the IgH region in three tumors (Supplementary Table 1). Almost all sequences per tumor were identical, demonstrating clonality. The tumors (three examples) further displayed copy number variations (CNV) (sFig. 1h), targeting differing genomic regions. Finally, transfer of tumor cells robustly elicited leukemia in wt acceptor mice (sFig. 1d–g) with as little as 500 transferred cells (sFig. 1f, g), indicating bona fide malignancy.

B lymphopoiesis in *Irf4*$^{-/-}$ mice harbors a hyperproliferative preB-I cell compartment

The uniform appearance of BCP-ALL in *Irf4*$^{-/-}$ mice suggested a defined preleukemic pro/preB cell state vulnerable to immortalization. Dimensional reduction of BM samples stained for B-cell differentiation markers, identified an enlarged fr.C preB cell compartment already in healthy *Irf4*$^{-/-}$ mice (Fig. 2a–c, sFig. 2a). This disturbed, but productive B-cell maturation confirms and extends previous reports [7]. Expression analysis of IL-7Rα and of CD2 (sFig. 2b, c), which accompanies cytosolic Igμ expression [15] further showed an increased frequency of CD2$^{-/dim}$IL-7Rα^{+}B220^{+}sIgμ^{-} preB cells in *Irf4*$^{-/-}$ mice.

Purified BM B220^{+} cells from *Irf4*$^{-/-}$ and wt mice were cultured with IL-7 (Fig. 2d–g) to compare proliferative capacities. After 6d, *Irf4*$^{-/-}$ cells had expanded roughly three-fold, whereas wt cell numbers decreased. Phenotypically, *Irf4*$^{-/-}$ cells accumulated at the fr.C stage (Fig. 2e, f) and expressed surface λ5 (Fig. 2g, h); exactly like *Irf4*$^{-/-}$ leukemia. In contrast, wt cells differentiated further, losing surface CD43 (making them fr.D) (Fig. 2e, f) with some cells expressing sIgμ (fr.E). Thus, IL-7 unmasked the leukemic potential of the fr.C compartment in *Irf4*$^{-/-}$ mice with both unchecked proliferation and a reinforced differentiation block. Notably, IL-7 dependent *Irf4*$^{-/-}$ preB-I cell proliferation was blocked by NIBR3049 and Ruxolitinib, inhibitors of the IL-7R downstream actors JAK3 and JAK1 respectively (sFig. 2d).

Irf4$^{-/-}$ B-cell progenitors exhibit reduced retention to the BM niche

As overt leukemia is characterized by systemic presence, we tested whether already preleukemic *Irf4*$^{-/-}$ B-cell progenitors would leak from the BM. To reduce the complex Hardy classification, we identified early B-cell progenitors, approximately until the preB-I stage, by B220^{+}CD2$^{-/dim}$ expression (sFig. 2b). We detected higher frequencies of splenic B220^{+}CD2$^{-/dim}$ cells in *Irf4*$^{-/-}$ than in wt mice (Fig. 2h), which accumulated with age. Thus, premature BM evasion adds to the impaired differentiation and hyperproliferation that characterize *Irf4*$^{-/-}$ preleukemia.

Potentially, this finding represented a systemic consequence of reduced vicinity to BM niche cells. We, therefore, analyzed the proximity of *Irf4*$^{-/-}$ and wt B220^{+}CD2$^{-/dim}$ cells to IL-7^{+} BMSCs in situ using *Il-7*^{eGFP} reporter mice (Fig. 2j–m, sFig. 2e, f, Supplementary Movie 1) [16]. In femur cryosections, the B220^{+}CD2$^{-/dim}$ subset (Fig. 2j, arrowheads) but not the whole *Irf4*$^{-/-}$ B220^{+} cell compartment was on average located further away from IL-7^{+} BMSCs, compared to wt control (Fig. 2l, m). We excluded differences in IL-7^{+} BMSC abundance between genotypes (sFig. 2g).

B progenitor retention to BM is secured via the interaction of CXCR4 on pro/preB cells with the IL-7^{+} BMSC-derived chemokine CXCL12 [17, 18]. Notably, *Irf4*$^{-/-}$ pro/preB cells expressed markedly lower levels of CXCR4 compared to wt cells (Fig. 2n). Chemokine migration assays with Hardy fr.A-D cells showed that *Irf4*$^{-/-}$ cells indeed migrated significantly less towards CXCL12 (Fig. 2o). Thus, reduced CXCR4-CXCL12 interaction likely induces the systemic seeding of *Irf4*$^{-/-}$ B progeny. Inversely, direct cell interactions are likely not responsible, because *Irf4*$^{-/-}$ and wt fr.A-D cells adhered equally to monolayers of OP-9 cells in vitro (sFig. 2h).

The IL-7-JAK-STAT-axis is recurrently altered in *Irf4*$^{-/-}$ leukemia

Most likely, a second, acquired genetic alteration was necessary for bona fide leukemia development and arose with low frequency per time, explaining the affected age and relatively low penetrance. Importantly, IL-7 deprivation of BM-evaded pro/preB cells should create strong survival stress and potential selection pressure for bona fide leukemogenesis. To identify somatically acquired mutations, we performed whole-exome sequencing (WES) of three independent tumors (T8, T10, T11) compared to sorted B220^{+}sIgμ^{-} cells from *Irf4*$^{-/-}$ BM. Comparisons of the single nucleotide variants (SNVs) between the three samples identified nine genes affected in all three tumor samples (Fig. 3a). Out of these, SNVs in four genes (*Rrs1, Jak3, AW82073,* and *Duxf3*) showed alternate base frequencies close to 0.5 or 1 (Fig. 3b), suggesting that they could be present on one or both alleles of all leukemic cells. Although we did not exclude the oncogenic potential of the other three genes, we focused on *Jak3*, because it is associated with IL-7R signaling. We detected *Jak3* mutations also in other tumors TD1, TD2, TD3, and T14 by Sanger- and RNA-sequencing (Fig. 3c, Supplementary Table 2). Thus, seven out of seven tested tumors carried *Jak3* mutations ("JAK3$_{mut}$"). All mutations targeted either the active kinase domain or the pseudokinase domain regulating JAK3 activity. Some of these SNVs have been described before [19]. Further, using two different classifiers, no gene fusions could be detected (see methods). Analysis of typical BCP-ALL genes [20] identified some respective mutations at low frequencies, indicative of subclonal events (Fig. 3d). Among these, mutations in *Jak1*, the partner to JAK3 in IL-7R signaling, were detected in both T8 and T11.

To analyze the role of the JAK3$_{mut}$, we transduced *Irf4*$^{-/-}$ preB-I cell cultures with retroviruses (RVs) encoding no or wt JAK3 or the JAK3$_{mut}$ R653H and T844M. Culturing transduced cells in the presence of αIL-7 to test for IL-7 independency unexpectedly resulted in cell death after a few days with no benefit for cells expressing JAK3$_{mut}$ (sFig. 3a, b). To test if JAK3$_{mut}$ would confer advantages with limited IL-7, RV-infected *Irf4*$^{-/-}$ preB-I cell cultures were exposed to decreasing IL-7 concentrations (Fig. 3e–g). At 0.1 and 0.01 ng/ml IL-7, both JAK3$_{mut}$-, but not

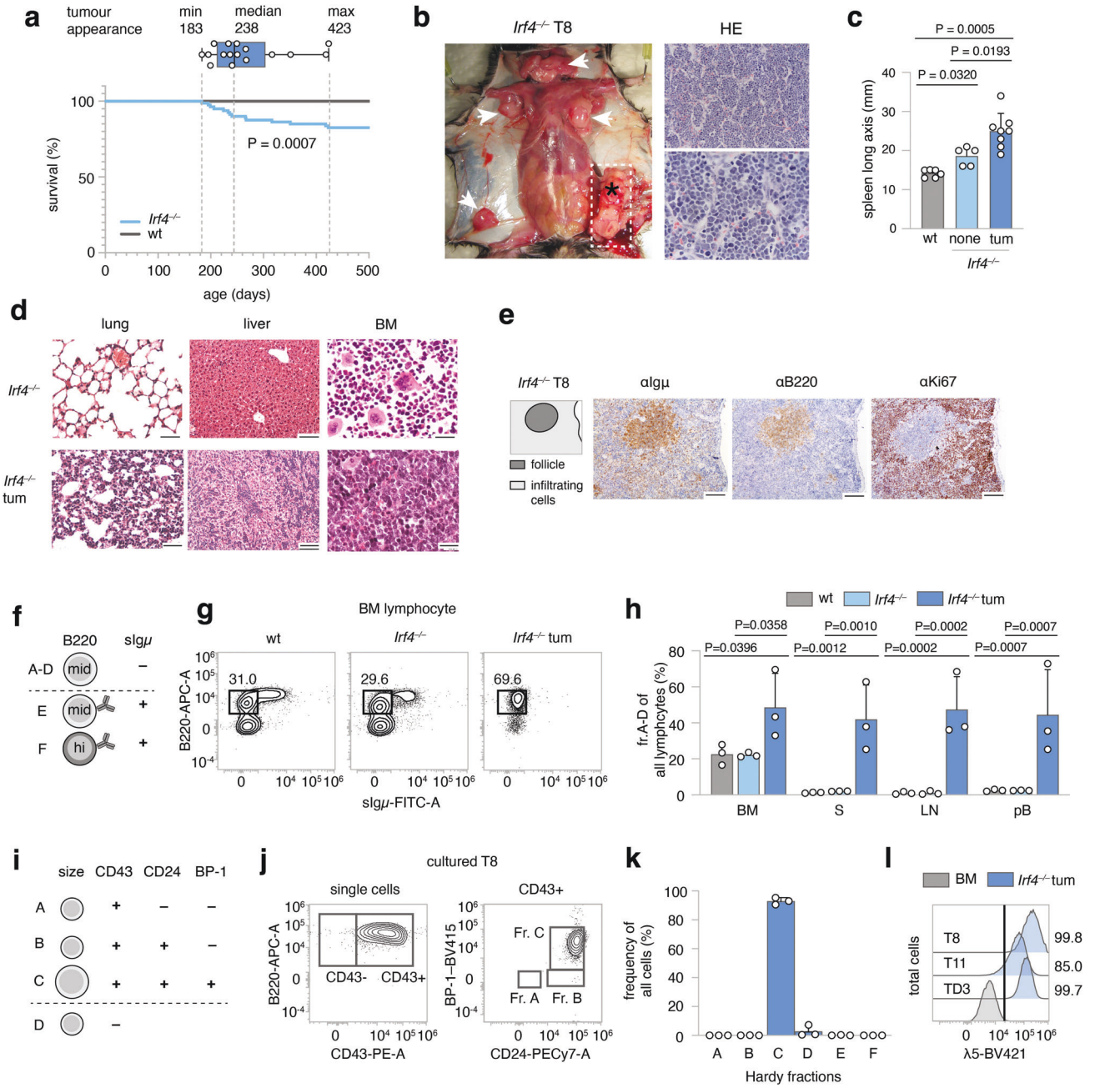

Fig. 1 Spontaneous emergence of preB-I cell BCP-ALL in adult *Irf4*$^{-/-}$ mice. a A cohort of 80 *Irf4*$^{-/-}$ and wt mice was observed over 500 days for tumor development. Kaplan–Meier plot of survival. Box and whisker plot indicates minimum, maximum and median age at tumor appearance of the 14 affected mice. **b** Macroscopic appearance of an exemplary tumor (asterisk) and LNs (arrowheads) in an *Irf4*$^{-/-}$ mouse. Right: Hematoxylin-Eosin (HE) staining from the tumor. Scale bars: top: 50 µm, bottom: 20 µm. **c** Longitudinal spleen (S) axis (mm) of *Irf4*$^{-/-}$ mice with ($n = 8$) or without ($n = 5$) tumor and control wt mice ($n = 6$). tum = tumor. **d** HE stainings of lung, liver, and BM of tumor mouse T8 and a healthy *Irf4*$^{-/-}$ mouse. Scale Bars: 50 µm (lung and liver), 20 µm (BM). **e** IHC-stainings of T8 mouse spleen for Igµ, B220, and Ki67. Scale bars: 100 µm. **f** Schematic representation of gross Hardy fractioning by surface B220 and Igµ expression. **g** Whole BM cells from wt, *Irf4*$^{-/-}$, and tumor mice were stained for B220 and sIgµ expression and analyzed by flow cytometry. **h** Quantification of cell frequencies gated as in (**g**) for BM, S, LN, and pB (peripheral blood) of $n = 3$ mice per group. **i** Tabular representation of Hardy fr. A-D by size, CD43-, CD24-, and BP-1-surface expression. **j** Surface expression of markers as in (**i**) of in vitro cultured T8 tumor cells **k** quantification of cell frequencies gated as in (**j**) for three tumors (T8, T11, TD3) **l** surface λ5 expression on T8, T11, and TD3 by flow cytometry in comparison to whole BM cells from *Irf4*$^{-/-}$ mice (BM) as a negative control. Statistical significance testing was performed with (**c**) one-way Welch-ANOVA followed by Dunnet's T3 multiple comparison test and (**h**) with two-way ANOVA followed by pair-wise Tukey corrected comparisons within each organ. Bars depict mean ± SD, dots indicate mice (**h**) or distinct *Irf4*$^{-/-}$ tumors (**k**).

$JAK3_{wt}$-RV led to the outgrowth of transduced over untransduced cells after 6d of culture (Fig. 3f, g). Thus, $JAK3_{mut}$ confer IL-7-hypersensitivity, but not -independency. Accordingly, ex vivo cultured *Jak3*-mutated T8 and T11 cells also still depended on IL-7 (sFig. 3c, d). However, the tumor cells exhibited increased proliferation (sFig. 3e) and λ5 surface retention (sFig. f, g) in decreased IL-7 concentrations when compared to wt or *Irf4*$^{-/-}$ preB cell culture.

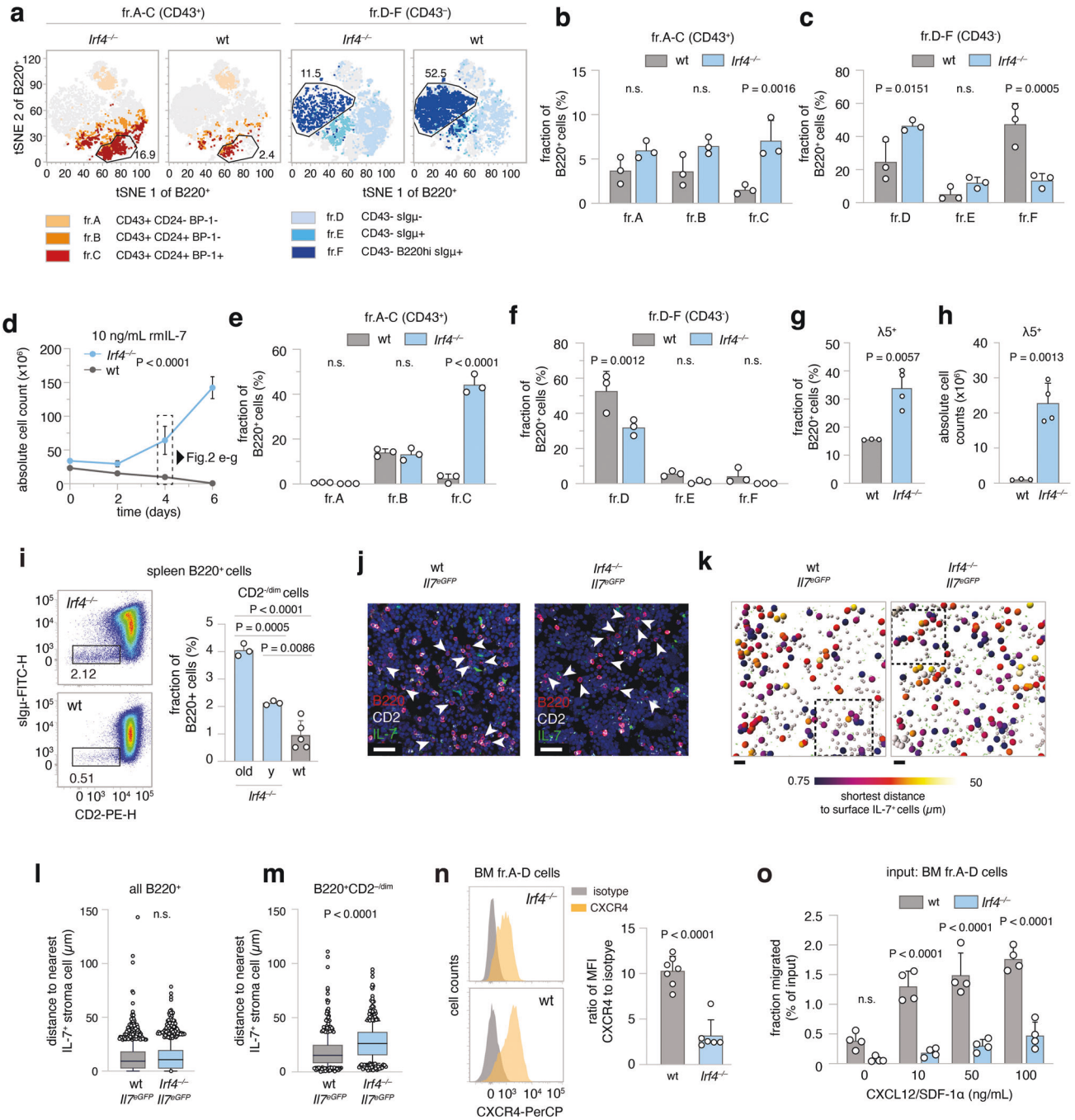

Fig. 2 ***Irf4*$^{-/-}$ B lymphopoiesis is preleukemically altered.** **a**–**c** flow cytometric analysis of BM cells for Hardy markers as in Fig. 1j. **a** tSNE of BM cells gated on B220^{+} cells. Colors correspond to Hardy fractions identified by the markers detailed in the legend. **b** and **c** quantification of Hardy fraction frequencies for $n = 3$ mice per genotype. **d**–**h** BM cells from *Irf4*$^{-/-}$ and wt mice were cultured in the presence of 10 ng/mL rmIL-7 for 6 days and **d** counted every two days. **e**, **f** After 4 days, cells were stained as in **a**–**c** and Hardy fractions quantified. **g** frequency and **h** absolute cell counts of λ5^{+} cells on day 4. **i** spleen cells from *Irf4*$^{-/-}$ ("y" = young: 6–10 weeks and old: >6 months) and wt mice were analyzed for the presence of CD2$^{-/dim}$sIgμ^{-} cells within the B220^{+} gate. one-way ANOVA, Tukey post hoc. **j**–**m** 7 μm cryosections from *Irf4*$^{-/-}$ *Il-7*^{eGFP} and wt *Il-7*^{eGFP} mice were stained for B220, CD2, GFP, and DAPI. **j** exemplary regions of BM cryosections. Arrowheads indicate B220^{+}CD2$^{-/dim}$ cells. Scale bars = 15 μm. **k** automated B220^{+} cell detection: gray spheres indicate B220^{+} cells, larger spheres B220^{+}CD2$^{-/dim}$ cells, color-coded for their distance to GFP^{+} cells. Rectangles indicate magnified areas in **j**. Scale bars = 40 μm. **l**, **m** quantification of distances to IL-7^{+} cells for **l** all B220^{+} and **m** B220^{+}CD2$^{-/dim}$ cells. ($n = 4$ mice per genotype, one cryosection from femur metaphysis per mouse analyzed). Box and whiskers indicate mean and 95-IQR, dots indicate cells outside 95-IQR. **n** BM cells from *Irf4*$^{-/-}$ and wt mice were gated on B220^{+}sIgμ^{-} fr.A-D cells and analyzed for CXCR4 expression (left panels as representative staining). Data is presented for $n = 7$ (wt) and $n = 6$ (*Irf4*$^{-/-}$) mice as the ratio of geometric mean for CXCR4 to isotype staining. **o** MACS-purified fr.A-D cells from BM were placed in the top insert of a Boyden chamber and left to migrate towards differing concentrations of CXCL12 for 16 h. Dots represent $n = 4$ biologically independent experiments, presented as migrated percentage of input cells. Two-Way ANOVA, Sidak post hoc for (**b**, **c**, **e**, **f**, **o**), Two-tailed unpaired *t* test for (**g**, **h**, **l**–**n**).

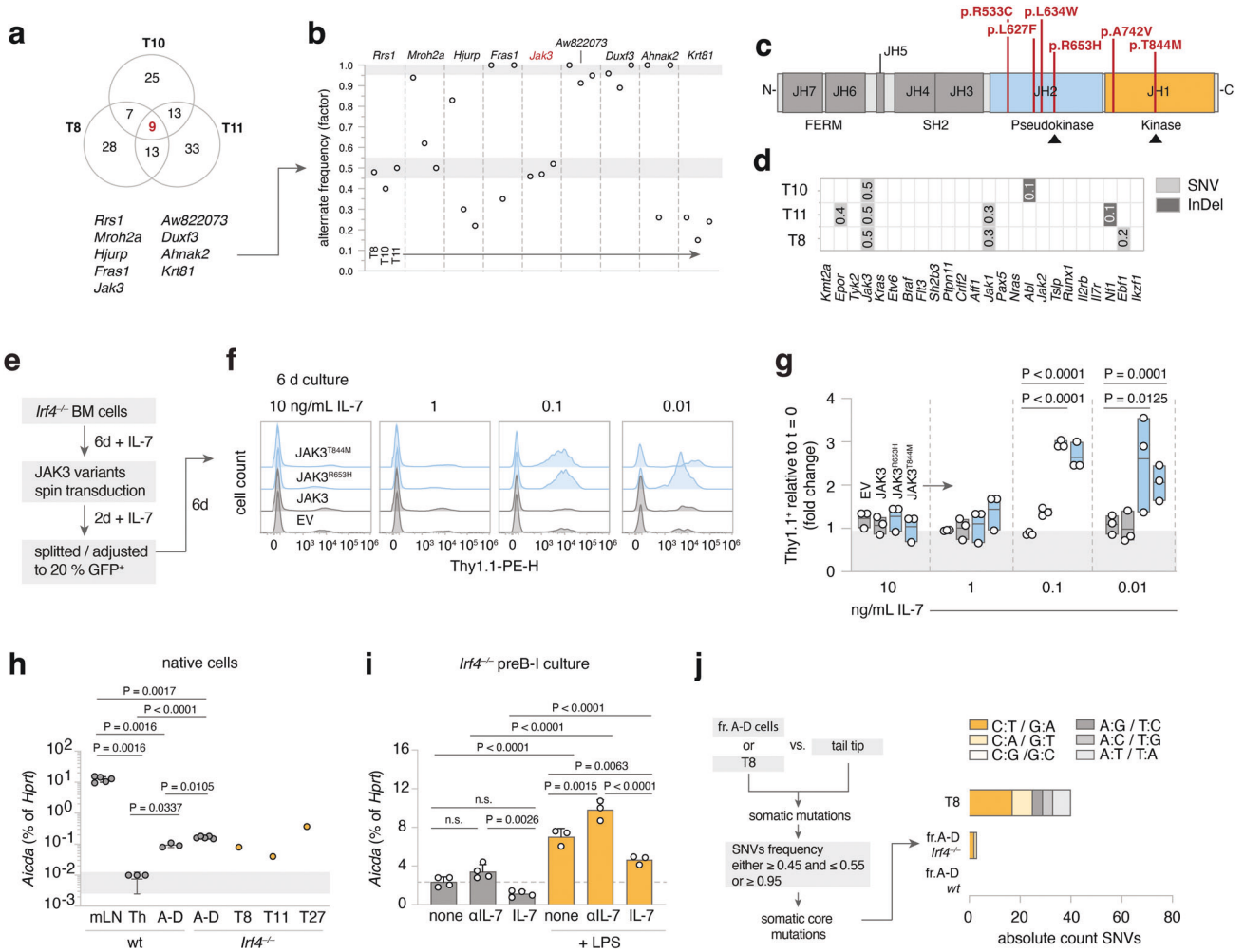

Fig. 3 leukemia-derived *Jak3* mutations heighten IL-7 sensitivity of *Irf4*$^{-/-}$ preB-I cells. a Venn diagram of shared mutated genes among WES from three *Irf4*$^{-/-}$ leukemia samples (T8, T10, T11) **b** the nine shared genes were filtered for SNV frequency. gray areas: >0.95 and 0.45–0.55 margins as core mutation filters. **c** the five detected distinct *Jak3* SNVs were mapped onto JAK3 primary structure (JH = Jak homology domain). **d** *Irf4*$^{-/-}$ leukemia WES were analyzed for mutations (SNV or InDel = insertions/deletions) in genes commonly altered in human BCP-ALL. Numbers indicate rounded frequencies of alteration. **e–g** *Irf4*$^{-/-}$ BM cells were cultured for 6d with 10 ng/mL rmIL-7, transduced with control or JAK3$_{mut}$ coding RVs, rested for 2 days, and then split into decreasing IL-7 concentrations. **f** Histograms for the Thy1.1 RV infection marker 6 days after splitting. **g** Quantification of Thy1.1^{+} cells after 6 days relative to start of culture ($t = 0$). Dots indicate $n = 3$ independent experiments, plotted as floating bars. EV = empty vector. **h** qRT-PCR from wt and *Irf4*$^{-/-}$ cells for *Aicda* mRNA expression, relative to *Hprt* expression for $n = 3$ (Th (= T helper) and sorted fr.A-D wt BM cells), $n = 5$ (mLN (= mesenteric lymph node) and sorted fr.A-D *Irf4*$^{-/-}$ BM cells), $n = 1$ per tumor T8, T11, T27. **i** *Irf4*$^{-/-}$ preB-I cell cultures from whole BM cells were cultured in combinations of IL-7, αIL-7, and LPS for 24 h, as indicated, and analyzed for *Aicda* levels by qRT-PCR for $n = 4$ (no LPS) and $n = 3$ (LPS) samples. **j** WES from fr.A-D cells and T8 were compared to tail-tip samples to identify SNVs. Filtering on SNV frequency "0.45–0.55 or ≥0.95" yielded putative "core mutations". Absolute numbers of nucleotide exchanges are presented as stacked bars, colors give the type of nucleotide exchange. Two-way ANOVA, Sidak post hoc for **g–i**.

Aicda is upregulated in *Irf4*$^{-/-}$ preB cells by LPS and deprivation of IL-7

Because six out of seven *Jak3* mutations were C to T base exchanges (Table 2), we suspected a specific mutagenic agent. DNA-editing enzymes including the APOBEC family member AID can deamidate cytosines, e.g., during somatic hypermutation [21, 22]. Repair mechanisms most often ultimately cause C to T conversions [23, 24]. Notably, AID is induced in wt preB cells by IL-7 withdrawal and LPS stimulation and acts as a facilitator of human BCP-ALL [25]. Therefore, we compared *Aicda* expression in sorted *Irf4*$^{-/-}$ and wt fr.A-D cells to that of wt mesenteric (m)LN- and CD4^{+} T_H1-cells as controls and to individual leukemia samples. While mLN cells highly expressed *Aicda*, fr.A-D preB- and leukemia cells, but not T_H1-cells, also expressed readily detectable amounts (Fig. 3h).

Furthermore, like their wt counterpart [25], in vitro expanded *Irf4*$^{-/-}$ preB-I cells upregulated *Aicda* further under LPS treatment and during IL-7 withdrawal (Fig. 3i). This finding can explain how BM evasion and exposure to pathogens might cooperatively initiate mutagenic processes via AID in vulnerable *Irf4*$^{-/-}$ preB-I cells.

To test if T8 exhibited signs of previous AID activity on a global level, we analyzed C:T/G:A-transition frequencies in WES of T8, as well as BM-sorted *Irf4*$^{-/-}$ and wt fr.A-D cells compared with matched tail-tip samples. Indeed, we found a marked preponderance of C:T/G:A-transitions in T8, when filtering on putative somatic core SNVs (Fig. 3j).

Jak3 mutations in mice mirror *Jak2* mutations in human Ph-like ALL

Next, we compared *Irf4*$^{-/-}$ leukemia to the complex landscape of human BCP-ALL subtypes (reviewed in refs. [11, 26, 27]), using a published human BCP-ALL cohort for which a random forest classifier had been established (Methods for details) [28]. Only

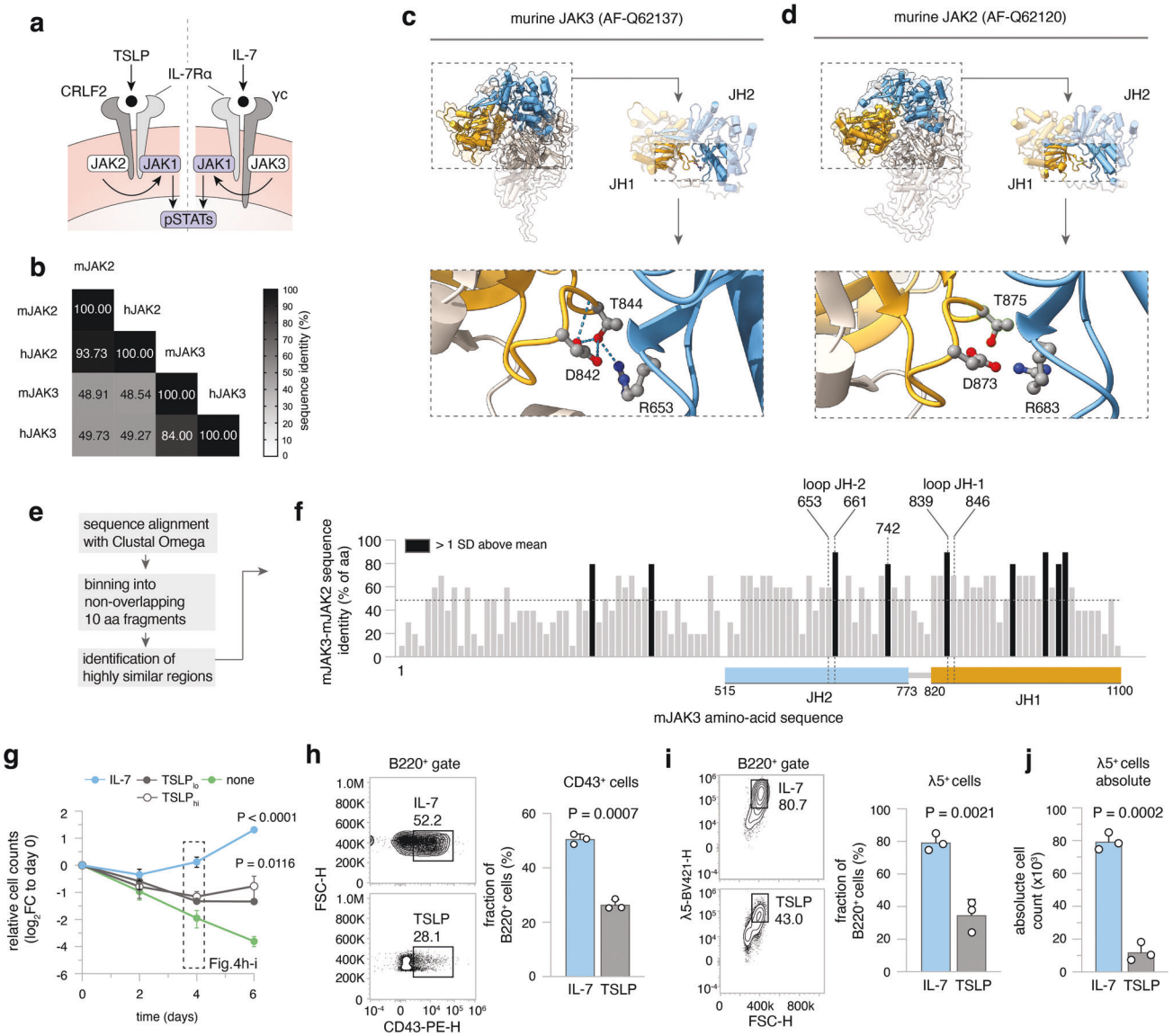

Fig. 4 Ph-like ALL in humans harbors *Jak2* mutation corresponding to *Jak3* mutations in *Irf4*$^{-/-}$ BCP-ALL. a Cartoon depicting IL-7 and TSLP receptor components. **b** Multiple sequence alignment results (using Clustal Omega) of mouse (m) and human (h) JAK3 and JAK2 amino-acid sequences are presented as a matrix. Numbers and shade indicate sequence identity as percentage of amino acids. **c**–**d** Alpha-fold structure predictions of murine **c** JAK3 and **d** JAK2 are presented. Colors indicate domains: orange = JH1, blue = JH2. JH1-JH2 interface is magnified and T844/T875, R653/R683, D842/D873 amino acids are highlighted as ball-and-sticks representations. Dotted lines = hydrogen bonds. **e** Overview of analysis for **f**: Sequences of mJAK2 and mJAK3 were aligned using Clustal Omega. The sequence of mJAK3 was binned into 10 non-overlapping amino-acid fragments and the sequence identity to mJAK2 plotted along the mJAK3 sequence. Dotted line = mean protein-wide sequence identity, black bars = areas with sequence identity greater than 1 SD above mean. JH1 and JH2 loop regions are mapped onto the sequence, JH1 and JH2 domain regions are indicated by colored rectangles below. **g**–**j** *Irf4*$^{-/-}$ BM cells were cultured for 6 days in the presence of 10 ng/mL rmIL-7, 10, or 100 ng/mL rmTSLP($_{lo/hi}$) or no cytokine (none). **g** $\log_2$ of cell counts relative to day 0 for $n = 3$ independent experiments plotted as means ± SD. One-way ANOVA, Sidak post hoc comparing cytokine effect. **h**–**i** On day 4, **h** CD43$^+$ and **i** λ5$^+$ cells within B220$^+$ cells were recorded for IL-7 and TSLP treated cultures. Numbers indicate percentages within the depicted gates of B220$^+$ cells. **j** Absolute counts of λ5$^+$ cells at day 4. Dots in **h**–**j** indicate $n = 3$ independent experiments, presented as bars (mean ± SD). Unpaired two-tailed *t* test for **h**–**j**.

mildly (potentially due to the interspecies comparison) elevated prediction scores were generated for Ph$^+$, Ph-like, KMT2a- and DUX4-rearranged human BCP-ALL (sFig. 4a, b). Since all of these except Ph-like are defined by specific gene rearrangements, that we had not detected in *Irf4*$^{-/-}$ mouse leukemia, we excluded them as comparable candidates.

Ph-like ALL harbors recurrent genetic alterations in signaling molecules, especially in CRLF2 and JAK2 [20]. While BCP-ALL overall preferentially affects children, the incidence of the Ph-like subtype increases from 10% in children to above 25% in AYA and adults [20, 29], reminiscent of the older age of *Irf4*$^{-/-}$ leukemic mice. Furthermore, a published dataset of 154 Ph-like BCP-ALL cases exhibited 10-fold reduced *IRF4* transcripts, when compared to other BCP-ALL subtypes [20].

While in human Ph-like ALL, *Jak2* is commonly mutated, we report recurrent *Jak3* mutations in *Irf4*$^{-/-}$ mice. As both proteins are part of distinct but similar signaling complexes in B-cell progenitors (Fig. 4a), we investigated structural and functional similarities between the specific *Jak3* and *Jak2* mutations. Comparisons of amino-acid sequences revealed high protein-

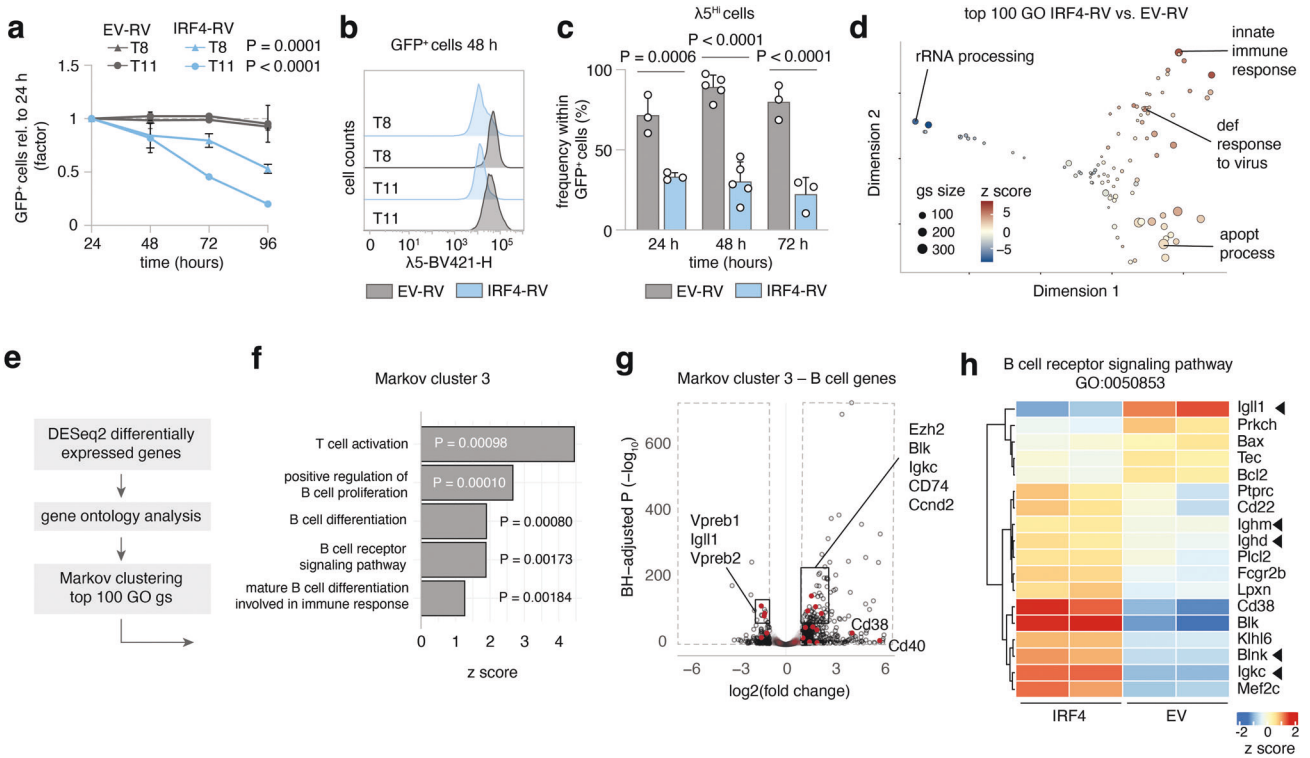

Fig. 5 IRF4 re-expression results in apoptosis and differentiation of leukemia cells. a–c T8 and T11 cells were transduced with IRF4-RV or control empty vector (EV)-RV. **a** GFP$^+$ cell frequency normalized to 24 h after transduction was recorded. One-Way ANOVA, Sidak post hoc for RV effect per tumor. Mean ± SD of $n = 3$ independent experiments. **b** Representative histogram of λ5 surface expression of GFP+ cells at 48 h. **c** Pooled Quantification of λ5^{Hi} cells for three (24, 72 h) to five (48 h) independent experiments for T8 and T11. **d–h** T8 cells were collected in duplicates at 24 h after EV-RV and IRF4-RV transduction and subjected to bulk RNAseq. **d** MDS plot of top 100 gene ontology (GO) gene-sets varying between EV and IRF4 transduced T8. Representative gene sets annotated. Size of circles = number of genes, color = *z* score. **e** Analysis strategy for GO gene-set clustering using Markov clustering. **f** Gene-sets from Markov cluster 3 and corresponding *P* values and *z* scores. **g** Volcano plot of B-cell genes from Markov cluster 3 (red) highlighted within all differentially regulated genes (black). **h** Heat map of B-cell receptor signaling GO gene-set. Immunoglobulin genes and the tumor suppressor *Blnk* are marked. Color = z score.

wide interspecies and intermolecular similarities for both proteins (Fig. 4b). Mapping the two amino acids R653 and T844 (mutated in *Irf4*$^{-/-}$ mice) onto JAK3 structure predictions, generated by the alpha-fold algorithm [30], revealed that the two amino acids are in direct contact at an interface of JH1-JH2 domains (Fig. 4c). This interface specifically is highly conserved in JAK2 compared to JAK3 (Fig. 4d, f, sFig. 4c, d). Intriguingly, R683 (corresponding to R653 in JAK3) is by far the most commonly mutated amino acid in JAK2 in Ph-like ALL, while mutations targeting T875 (corresponding to T844) also have been described [31]. These findings suggest that mutations in human JAK2 and mouse JAK3 affect a highly similar functional hotspot.

As mentioned above, JAK2 and JAK3 are part of distinct, but similar receptors: JAK3 binds the common γ-chain involved in IL-7 signaling, while JAK2 associates with CRLF2 involved in TSLP signaling. Both signals involve the IL-7Rα chain and the same downstream pathways (STATs, PI3K) [32]. Therefore, the alternative presence of JAK3/JAK2 mutations between mouse and human BCP-ALL might reflect different cytokine preferences. Human proB/preB cells proliferate in response to both TSLP and IL-7 [33]. However, in *Irf4*$^{-/-}$ BM cells IL-7, but not TSLP induced robust proliferation (Fig. 4g) as well as high frequencies and absolute counts of CD43$^+$ (Fig. 4h) and λ5$^+$ preB cells (Fig. 4i, j).

IRF4 re-expression leads to cell death and differentiation

As *Irf4* deletion was a prerequisite for leukemia in our model, we examined the effect of forced IRF4 re-expression, using RVs coding for GFP alone (EV-RV) or plus IRF4 (IRF4-RV). When re-introducing IRF4 into T8 or T11, GFP$^+$ IRF4-expressing-, but not GFP$^+$ control cells gradually disappeared over time (Fig. 5a). AnnexinV/PI stainings confirmed apoptosis (not shown). Further, we noted the loss of surface λ5-expression induced by IRF4-RV (Fig. 5b, c). Comparing the transcriptomes of still viable cells 24 h after transduction revealed strong induction of "apoptotic process" and "innate immune response" gene ontology (GO) gene-sets (gs) (Fig. 5d). Markov clustering of GO gs affected by IRF4 re-expression (Fig. 5e, f) further identified several coregulated B-cell differentiation gs (Fig. 5f), with downregulated ψL components *Igll1*, *Vpreb1,* and *Vpreb2*, but upregulated differentiation genes including *Igμ*, *Igκ,* and *Blnk* (Fig. 5g, h, sFig. 5a, b). Similar results were obtained for T11 (sFig. 5c, d). Therefore, fully transformed leukemia remained targetable by IRF4 re-expression.

Small compound agents affecting *Irf4*$^{-/-}$ leukemia *cells* in vitro

Next, we screened a collection of kinase inhibitors for their capacity to kill *Irf4*$^{-/-}$ leukemia cells in vitro. We included NIBR3049 targeting JAK3, Ruxolitinib, an inhibitor of JAK1/2 (downstream of JAK3), and Dexamethasone, a cornerstone for treating lymphomatous malignancies. Furthermore, we included inhibitors of NFκB (IKK, TAK1), JNK, MEK, ERK, PP2A, GFI1, FAK, and the Bruton tyrosine kinase (BTK) acting downstream of the BCR.

A variety of these substances potently killed tumor cells (sFig. 6a), implying the involvement of multiple pathways in leukemia cell survival. The efficacy of Ruxolitinib and NIBR3049 corroborated our results concerning *Jak3* driver mutations. Furthermore, inhibitors of GFI1 and PP2A, as well as NFκB and

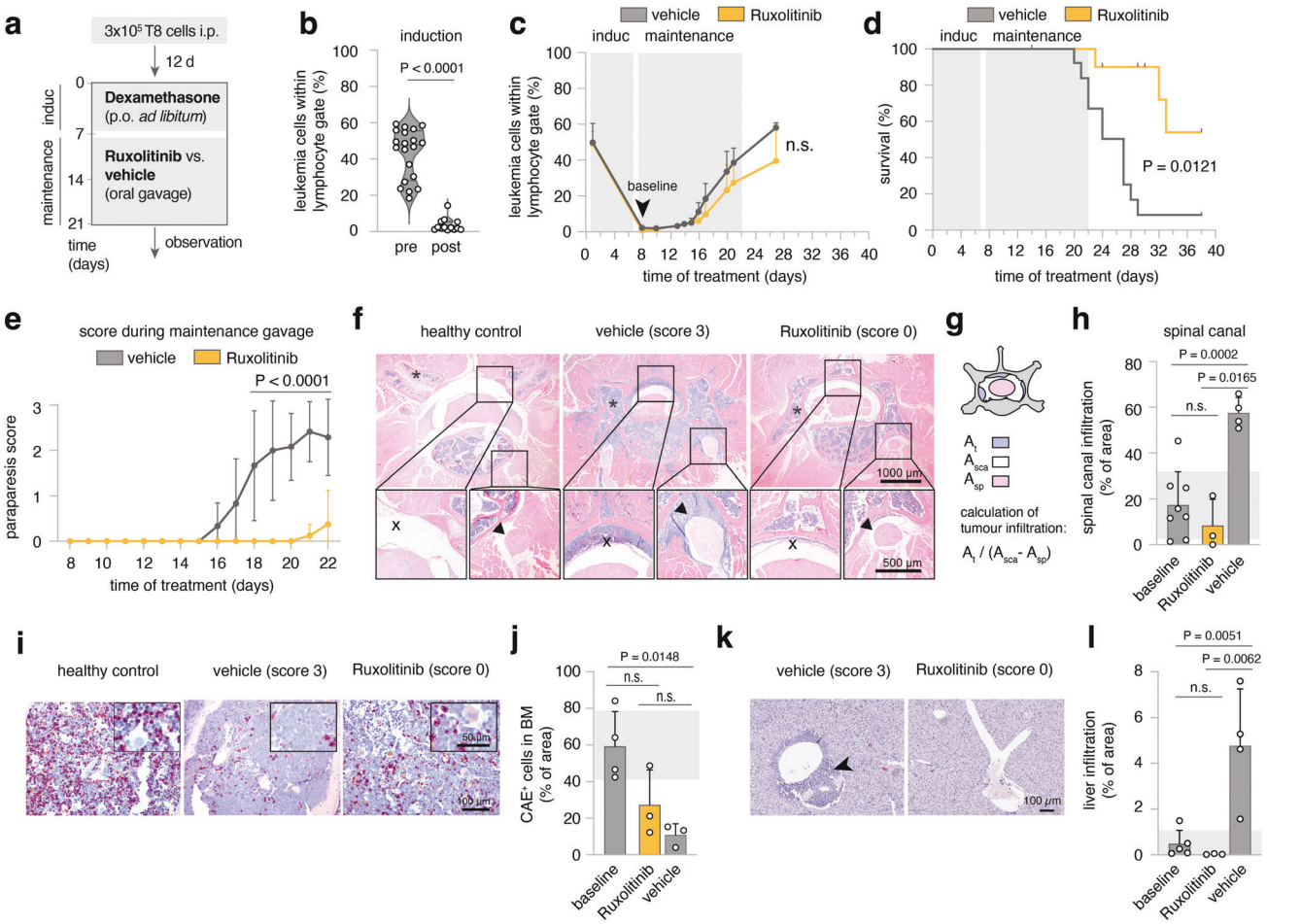

Fig. 6 Ruxolitinib reduces leukemic meningeosis and organ infiltration in vivo. a Schematic overview of experimental design. Day 0: injection of mice with 2×10^5 T8 cells. After 12 days initiation of Dexamethasone induction therapy supplied in drinking water for seven days. Maintenance therapy comprised either Ruxolitinib-phosphate (11 mice) or vehicle control gavage (13 mice) twice daily for 14 days. Mice were scored daily and blood sampling was performed regularly. **b** Leukemia cell frequency ($B220^+sIg\mu^-$) within lymphocyte gate before and after induction with Dexamethasone. Two-tailed unpaired *t* test **c** time-course of leukemia cell frequencies in peripheral blood for Ruxolitinib and vehicle-treated mice. **d** Survival as Kaplan–Meier plot analyzed with Log-rank test. In the Ruxolitinib group, four mice were excluded and censored due to intervention-related adverse reactions or due to their use in the analysis described in **f**–**l**. **e** Disease scores, determined as described in methods. Mean ± SD of the scores per indicated treatment group analyzed by two-way ANOVA, Sidak post hoc. $n = 2$ replicate experiments for **b**–**e** with similar outcome. **f** Exemplary histopathology (HE) of healthy or leukemia bearing mice (score 3, vehicle-treated or score 0, Ruxolitinib-treated). One representative mouse per condition. Bar size in the bottom right corners. Top panels: an overview of cross-sectioned lumbar vertebrum, bottom inserts from spinal canal (left) and spinal nerve root (right). **g** Schematic representation of the calculation of tumor infiltration into the spinal canal. (A_t: area of tumor infiltration, A_{sca}: area of total spinal canal, A_{sp}: area of the spinal cord). **h** Quantification of spinal canal infiltration according to **g** for $n = 8$ after induction (baseline), $n = 3$ score 0 (Ruxolitinib) and $n = 4$ score 3 (vehicle) mice. **i** Representative CAE stainings from vertebral BM for score 0 and score 3 mice. **j** Quantification of area occupied by CAE^+ cells relative to total BM area for $n = 4$ (baseline), $n = 3$ (score 0, Ruxolitinib) and $n = 4$ (score 3, vehicle) mice. **k** Representative HE stainings from liver tissue for score 0 and score 3 mice, Scale bar bottom right. **l** Quantification of tumor infiltrated area relative to whole liver area for $n = 5$ (baseline), $n = 3$ (score 0, Ruxolitinib) and $n = 4$ (score 3, vehicle) mice. Each dot represents measurements of three complete liver cross-sections per mouse.

JNK, were potent. In contrast, inhibiting BTK, MEK and ERK had no impact.

In vivo therapy of established *Irf4*$^{-/-}$ B-ALL

Next, we implemented JAK inhibition as in vivo treatment for *Irf4*$^{-/-}$ leukemia. We began induction therapy with Dexamethasone around day 12 after adoptively transferring 3×10^5 T8.1 cells i.p. into wt mice (Fig. 6a), when overt leukemia was noted in peripheral blood (pB) (Fig. 6b "pre"). After 7d of treatment, leukemic cell numbers in pB were robustly reduced (Fig. 6b "post"), although few cells reproducibly remained detectable (Fig. 6c). Maintenance therapy was continued with Ruxolitinib or vehicle control by oral gavage twice daily for the following 12 days (Fig. 6a, c). Importantly, the half-life of Ruxolitinib in mice is only 0.8 h ("Australian Public Assessment Report for Ruxolitinib", Australian Government), implying that any observed in vivo effectiveness might be underestimated.

Despite maintenance therapy, leukemic cells in pB reappeared, with no significant difference between treatment groups (Fig. 6c). However, treatment with Ruxolitinib resulted in a clear survival benefit (Fig. 6d) and marked improvement of a prominent neurological symptom: in sham-treated animals, temporary limpness of the tail and hind legs occurred seconds after gavage, which we quantified using a newly established scoring system (ranging from 0 to 3, see Methods).

Mechanistically, ultrasound imaging revealed an echogenic paravertebral mass (sFig. 7a, b) in score 3, but not score 0 mice. By histology, score 3 correlated with severe infiltration of blasts into

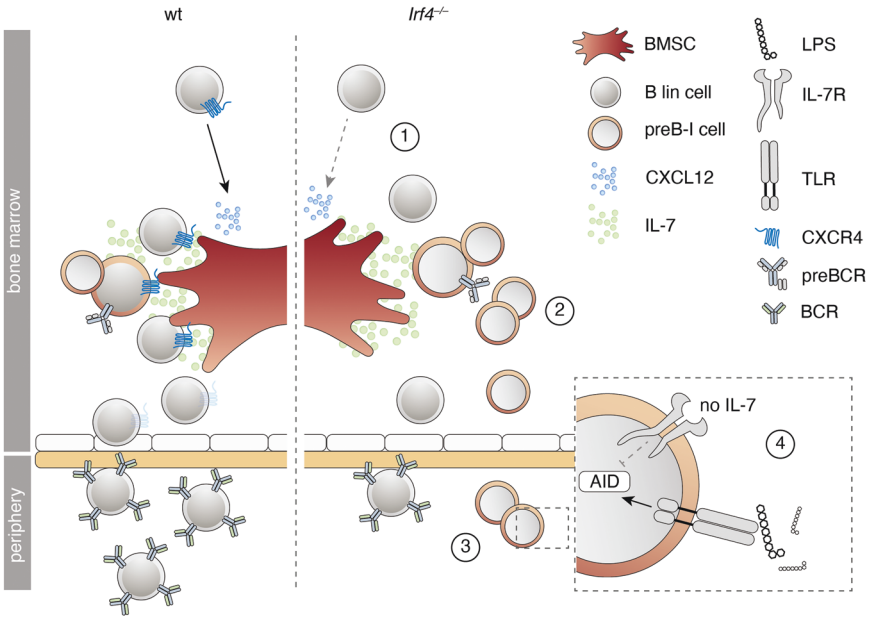

Fig. 7 Summary of the preB-I preleukemic state induced by IRF4 deficiency. Cartoon summarizing the findings for IRF4 deficient compared to wt B lymphopoiesis. B lineage (lin) cells are less responsive to BMSC-derived CXCL12 due to reduced surface CXCR4 expression (1). *Irf4*$^{-/-}$ preB-I cells exhibit impaired differentiation and IL-7 dependent hyperproliferation (2). *Irf4*$^{-/-}$ preB cells escape into the periphery (3), where a combination of IL-7 deprivation and danger-associated molecular patterns (such as LPS) might induce AID expression (4), fueling mutagenesis.

the spinal canal (X in Fig. 6f), extending into spinal nerve roots (arrowhead in Fig. 6f). Therefore, paraparesis likely represented a manifestation of mouse leukemic meningeosis, exacerbated by gavage-induced increases in intraabdominal pressure.

Paraparesis was reproducibly relieved during Ruxolitinib treatment (Fig. 6e), correlating with the suppression of perimyelon infiltration that ensued in vehicle-treated mice after the end of induction therapy (Fig. 6f, h). In contrast, the severely impaired hematopoiesis in sham-treated mice, indicated by low CAE^{+} cell frequencies, was not significantly ameliorated by Ruxolitinib (Fig. 6i, j).

These findings raised the possibility that Ruxolitinib preferentially targets infiltration of solid organs rather than BM or pB. Accordingly, Ruxolitinib fully blocked the liver infiltration as observed in sham-treated mice (Fig. 6k, l). As tissue infiltration is regulated by homing receptors, we treated T8.1 and T8.2 cells with Ruxolitinib in vitro and recorded the expression of CD29 (integrin β1), which pairs with various integrin alpha chains involved in cell- and tissue adhesion [34, 35]. Notably, on T8.1 and T8.2, Ruxolitinib reduced CD29 expression dose-dependently (sFig. 6c–e) while it even slightly increased expression of MHC I molecules (H2D^{b}, H2K^{b}), stained as a specificity control.

DISCUSSION

The herein described spontaneous leukemogenesis in *Irf4*$^{-/-}$ mouse stresses the particular vulnerability of preB-I cells. Our data provide insights for (a) conditions promoting leukemogenesis, (b) functional consequences of *Jak* mutations, (c) parallels of mouse and human BCP-ALL and (d) potential in vivo treatment:

(a) We provide evidence for a two-hit leukemogenesis model: The first hit (*Irf4* loss) resulted in reduced differentiation, IL-7-dependent hyperproliferation, and impaired retention to the BM niche (Fig. 7). A second hit (targeting *Jak3* in our model) created a dominant survival signal, probably founding overt preB-I leukemia.

The induction of BCP-ALL in *Irf4*$^{-/-}$ mice are similar to *Ikzf1* and *Pax5* mutated mouse models [36–38], implying similarities between these TF-alterations. Probably, one shared mechanism is the differentiative impairment. Importantly, for *Irf4*$^{-/-}$ fr.A-D cells we even detect slightly higher levels of *Pax5* compared to wt fr.A-D cells (sFig. 8), ruling out that the findings in *Irf4*$^{-/-}$ mice merely mirror those of *Pax5* deficiency. The reverse remains conceivable; that *Ikzf1* and *Pax5* mutations converge in lowering IRF4 expression.

In addition to mice mutated in *Pax5* or *Ikzf1*, *Irf4/Irf8*$^{-/-}$, and *Irf4/Spi1*$^{-/-}$ mice have been shown to develop leukemia early in life at a high incidence [39, 40]. Contrasting these studies, we report that a single deficiency for IRF4 fully suffices for leukemogenesis. We excluded secondary alterations in *Irf8, Spi1* in our model: we found unchanged expression and gene sequence of IRF8 (not shown) and normal amounts of *Spi1* transcripts (sFig. 8a) in *Irf4*$^{-/-}$ fr.A-D cells. The single IRF4 deficiency models potential clonal initiating events better than *Irf4/Irf8*$^{-/-}$ or *Irf4/Spi1*$^{-/-}$ mice, because *Irf4*$^{-/-}$ mice harbor productive B-cell development.

We newly describe that a preleukemic alteration can lead to reduced BM retention, presenting a tentative explanation for the induction of mutagenic signals, as deprivation from IL-7 and exposure to bacterial compounds can cooperatively induce the mutagenic agent AID [25].

(b) Why do *Jak3* mutations only lead to enhanced sensitivity to, but not complete independence of IL-7? Analysis of JAK3 and JAK2 structure implied that mutations of R683/R653 and T875/T844 might decrease JH1-JH2 interaction strength. This would imply reduced auto-inhibition as the GOF mechanism—in line with findings for the JAK family member TYK2 [41]. This alone cannot explain cytokine independency, owing to the receptor biology: The two preassembled receptor chains keep JAKs intracellularly separated [42]. Ligand binding is needed for a conformational change that brings JAKs into the proximity needed for cross-phosphorylation.

To explain our observations, we propose an oncogene model with two equilibria (Fig. 8a, b): the first is determined by cytokine concentration and dictates the probability of receptor conformation change (Fig. 8a). The second, independent equilibrium (Fig. 8b), is determined by the interaction strength at the JH1-

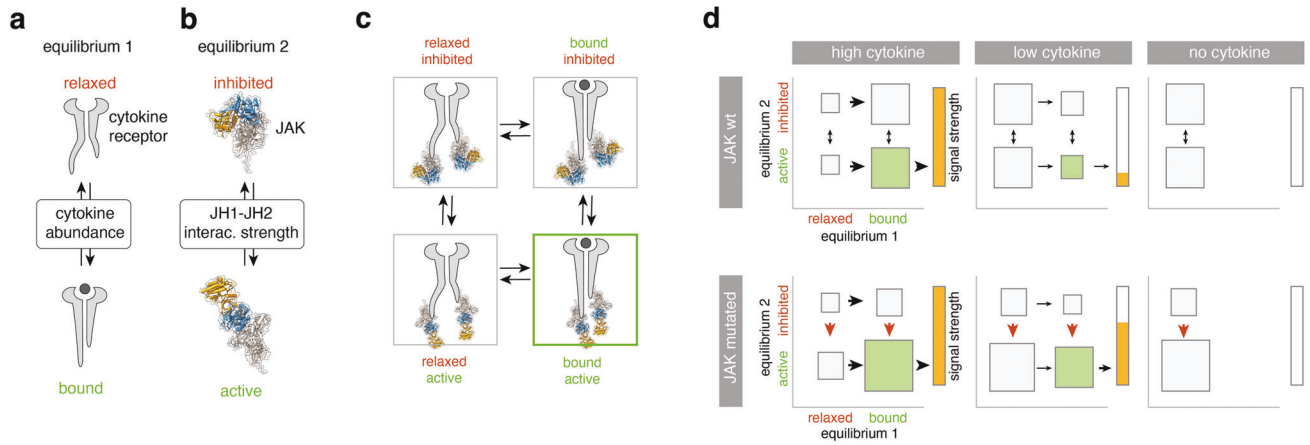

Fig. 8 A "two-equilibrium model" explains JAK mutant effects in primary preB-I cells. a Equilibrium 1 is determined by cytokine abundance and dictates the cytokine receptor state (bound vs. relaxed). **b** Equilibrium 2 is determined by the interaction strength between JH1 and JH2 domains in JAKs and dictates the JAK state (inhibited vs. active). **c** Equilibria 1 and 2 interact to create four possible states. Green lettering indicates signaling favoring state. Green frame indicates the actively signaling state. **d** For high (left), low (middle), and no (right) cytokine in the presence or absence of JAK3 mutations, hypothetical probabilities of equilibria states as in **c** are presented. Size of rectangles signifies likelihood of state relative to others. Arrows indicate shifts of equilibria, red arrows indicate the effect of JAK mutations. Green rectangle = active signaling state (bound and active). Bars to the right of each panel indicate signal strength as a direct result of the two equilibria adjacent to it.

JH2 interface and dictates the probability of JH1 and JH2 dissociation. Only the combination of the "bound" and "active" state (Fig. 8c) would result in the elicitation of a signal (Fig. 8c, green frame).

In this model, JAK mutations would only affect the second equilibrium (Fig. 8d, red arrows). Sporadic ligand binding would still be needed for elicitation of signaling. The model stringently predicts the better exploitation of low cytokine concentrations for JAK_{mut} that we observed in vitro. Figure 8d depicts theoretical probabilities of receptor states in the presence (top row) or absence (bottom row) of JAK mutations.

Our findings that $JAK3_{mut}$ confer heightened cytokine sensitivity, but not -independence, is in contrast to what has been found for JAK2-R683G mutants expressed in the commonly used BaF3 cell line [43]. However, BaF3 cells depend on IL-3 and not IL-7Rα cytokines (i.e., IL-7 or TSLP). Therefore, it remains conceivable, that the IL-3 receptor provides a different physiology, which may deviate from the IL-7R physiology in primary B progenitors.

(c) The finding that *Irf4*$^{-/-}$ preB-I cells respond preferentially to IL-7 over TSLP presents a possible explanation, why mouse models of BCP-ALL acquire *Jak3* mutations, and human Ph-like ALL typically harbors *Jak2* mutations. Our comparison of JAK structure predictions yielded corresponding mutations likely to elicit similar downstream effects.

(d) Lastly, our in vivo experiments reinforce Ruxolitinib as a potential treatment for JAK-driven BCP-ALL. The compound represents an important therapeutic agent in myeloproliferative disease and is already studied for the treatment of Ph-like-ALL [44, 45]. We describe a preferential effect of Ruxolitinib on CNS- and organ infiltration, potentially due to reductions in integrin expression on leukemia cells. These effects are of potential translational importance because current CNS-targeted therapies for ALL remain toxic.

METHODS

Mice

C57Bl/6 mice were purchased from Charles River, Sulzfeld, Germany. *Irf4*$^{-/-}$ mice [7] and *Il-7*^{eGFP} mice [46] (provided by Koji Tokoyoda, DRFZ Berlin) were bred on the C57Bl/6 background and housed in the animal facility of the Biomedical Research Center at the University of Marburg, Germany. If not stated otherwise, all mice used in the presented experiments were 8–12 weeks old and sex-matched.

Tumor cell lines and cell culture

Stable tumor cell lines T8.1, T8.2, and T11 were established from primary *Irf4*$^{-/-}$ leukemia cells (derived from primary tumor 8, i.e., T8, or tumor 11 (T11)) by culturing them on a monolayer of irradiated (30 Gy) ST2 stromal cells [47] grown to confluency in Opti-MEM medium (31985070, ThermoFisher Scientific) supplied with 1% cell culture supernatant from JIL-7.6 J558 cells [48] (a gift from Fritz Melchers, Berlin) as a source of IL-7. After several passages, T8 and T11 cells grew independently of ST2 cells. For in vitro inhibitor experiments, 2.5×10^5 T8.1 or T8.2 cells (or T11 cells) were cultured in 500 µL RPMI medium in 48 well plates in the presence of the indicated concentrations of inhibitors. To determine the percentage of viable cells, samples were stained using Annexin V and propidium iodide (PI) (see below) after 48 h. Substances used include Defactinib (S7654, Selleckchem), Oxocaenol (O9890, Sigma), GANT61 (Sigma, G9048), SP203580 (EI-286-0001, Enzo), SP600125 (EI-305-0010, Enzo), PD98059, Promega), Ibrutinib (S2680, Selleckchem), BAY11-7082 (ALX-270-219, Alexis), Dexamethasone (PZN 08704491, mibe GmbH) and Ocadaic acid (O4511, Sigma).

Murine pro/preB cell cultures

Femur and tibia bones from 8 to 12 weeks old mice were explanted and cleaned from adherent tissues. Cells were extracted via centrifugation at 11×10^3 RPM for 10 s. Total BM cells were enriched for $B220^+$ ($slg\mu^-$) B lineage cells using an in-house magnetic-activated cell sorting protocol. Briefly, whole bone marrow cells were stained with a mix of FITC-conjugated antibodies to (Igµ), CD11b, B220, Ter119, CD49b, CD4, and CD8 (all from eBioscience), followed by incubation with an anti FITC/streptavidin/biotin/magnetic bead complex (Miltenyi Biotec) and magnetic sorting using a microcentrifugation tube stand (Miltenyi Biotec) [49]. Sorting efficiency, as confirmed by flow cytometry, routinely exceeded 90%. Cells were seeded at a density of 1×10^5 cells per well in 200 µL RPMI complete (96-well plates, Greiner). Pro/preB cell cultures were propagated with 10 ng/mL rmIL-7 (217-17, Peprotech) in RPMI-1640 medium complete (R8758, Sigma-Aldrich, supplemented with: 10% FCS (Sigma-Aldrich), 2 mM L-glutamine (Biochrom), 50 µM β-mercaptoethanole (Sigma-Aldrich), 0.03/0.05 g per 500 mL Penicillin G/Streptomycin Sulfate, 1% non-essential amino acids (PAA Laboratories)). In some experiments, pro/preB cells (1.25×10^6/mL medium) were treated for 24 h with LPS (Sigma, 1 µg/ml), anti-IL-7 (BioXCell, 10 µg/ml), rmIL-7, or respective combinations, before generating mRNA for qRT-PCR.

Transwell migration assay and OP-9 adhesion assay

For the transwell migration assays, Hardy fr.A-D cells were magnetically sorted from BM of wt and *Irf4*$^{-/-}$ mice as described above (with addition of FITC-conjugated anti-Igµ antibody), and 2×10^5 cells in RPMI (without additives, FCS-free) containing 10 ng/mL rmIL-7 seeded in 50 µL in the top

chamber of 96-well 5 µm pore uncoated 96-well transwell plates (HTS transwell® Corning). The bottom chamber was flooded with 200 µL RPMI containing indicated concentrations of rmCXCL12 (Peprotech). After 16 h, inserts were removed, cells in the bottom chamber were collected, counted, and analyzed for B220 surface expression using flow cytometry. The fraction of migrated cells was calculated as n(migrated) × $freq_{B220}$(migrated)/n(input) × $freq_{B220}$(input). Normalization to $B220^+$ cells reduced interexperimental differences due to differences in cell purity after magnetic selection. For OP-9 adhesion assays, 5×10^3 OP-9 cells (a gift from Hyun-Dong Chang, DRZF Berlin) were seeded in 96-well microtiter plates 24 h before the assay. On the day of the assay, fr.A-D cells were purified as above and 2×10^5 fr.A-D cells were seeded on top of OP-9 monolayers in RPMI complete + 10 ng/mL rmIL-7. Plates were centrifuged briefly to accelerate cell descension. After 1 h, suspended cells were collected in the supernatant and by washing OP-9 monolayers two times with PBS.

Flow cytometry and cell sorting

For surface staining of B lineage markers, cells were harvested, resuspended in PBS/1% FCS and stained with anti-B220 (RA3-6B2, Biolegend), anti-Igµ (II/41, BD Bioscience), anti-CD43 (RM2-5, Biolegend), anti-CD24 (M1/69, invitrogen), anti-BP-1 (BP-1, BD Bioscience), anti-CD2 (RM2-5, Biolegend), anti-CXCR4 (L276F12, Biolegend), anti-CD127 (=IL-7Rα) (A7R34, BD Bioscience), anti-CD179b (=λ5) (LM34, BD Bioscience) as indicated (20 min at room temperature in the dark). All antibodies were employed at a dilution of 1:500. Fluorescence was recorded using either a FACS Aria III (BD) or an Attune NxT (Thermo-Fisher) analyzer. Data analysis was performed using the FlowJo V10 software (BD). For dimensional reduction, we used the t-Distributed Stochastic Neighbor Embedding (tSNE) [50] algorithm built into FlowJo V10. Epitopes on BM cells from $Irf4^{-/-}$ and wt control mice used for dimensional reduction analysis comprised B220, sIgµ, CD43, CD24, BP-1. For RNA and WES analyses, BM cells were surface labeled for B220 and sIgµ expression, and $B220^+sIg\mu^-$ cells were sorted using a FACS Aria III (BD Bioscience). Sorting efficiency was routinely above 95%. To determine cell viability, AnnexinV/PI staining was performed using 5 µL AnnexinV (640905, Biolegend) per 500 µL HBSS. After 20 min of incubation at room temperature in the dark, 1 µL PI (421301, Biolegend) was added, and cells were immediately measured.

CNVs analysis

CNVs were analyzed in tumor samples 8, 10, and 14 and compared to $Irf4^{-/-}$ normal tail tissue. Whole DNA was extracted from 5×10^6 cells per sample using the Macherey-Nagel NucleoSpin Tissue kit (REF 740952.50) according to the manufacturer's protocol. Library preparation was performed using the Illumina Nextera DNA kit according to the manufacturer's instructions. Sequencing was performed on an Illumina-HiSeq-1500 platform in rapid-run mode at the Genomics Core Facility of Philipps-University Marburg. Fastq quality control was performed using custom scripts. Raw sequenced reads were aligned to the Ensembl Mus musculus reference (revision 79) using Bowtie2 (version 2.0.0) [51] with standard parameterization. Analysis of CNVs was performed using the cn.mops (Copy Number estimation by a Mixture Of PoissonS) package (version 1.18.1) [52] with the following parametrization: prior impact = 1, lower threshold −0.9, upper threshold = 0.5 minimum width = 4. Window length was set to 10000 and the algorithm was run in unpaired mode.

BM cryosections and analysis of B progenitor vicinity to IL-7^+ BMSCs

Mouse femora from $Irf4^{-/-}$ or *wt il-7*^{eGFP} reporter mice were explanted, cleaned from soft tissues, and fixated overnight in 4% PFA PBS (Alfa Aesar). Samples were then dehydrated by incubation in 30% sucrose in PBS for 24 h. Dried and dehydrated femora were snap-frozen in cryomolds® (Tissue-Tek) using O.C.T freezing medium (Tissue-Tek) by being placed in a beaker of Hexan, surrounded by a beaker of Acetone and dry ice. Samples were stored at −20 °C until processing. Cryosections of 7 µm were generated with a Leica cryostat (DB80 LX microtome blades, Leica) using Kawamoto tape [53] (Section-lab) as described before [54]. Cryosections were stained with antibodies against B220 (RA3-6B2, Biolegend), CD2 (14-0021-85, eBioscience, conjugated to AF555 using lightning-Link kit, Abcam), GFP (Rockland goat polyclonal anti-GFP, 600-101-215) with secondary rabbit anti-goat F(ab')2 AF488 (thermo-scientific A21222). Samples were then mounted in DAPI ProLong Gold Antifade (ThermoFisher Scientific). Images were recorded using a Leica confocal (SP8i) microscope. Image analysis was performed in IMARIS (version 9.7.2).

Histological analyses

Tissue samples were immediately fixed in 4% PFA PBS solution. Histological analysis was performed on 3 µm thick sections from paraffin-embedded tissue as described previously [55]. Briefly, rehydrated paraffin sections were first blocked with 0.3% H_2O_2 and goat normal serum. For immunohistochemical (IHC) stainings, rat antibodies against CD45R/B220 (clone RA3-6B2, BD) and KI67 (clone TEC-3, Dako) were then incubated on the tissue slices and the bound antibody was detected with biotinylated goat anti-rat IgG (Southern Biotechnology). Bound antibody was visualized with the Vectastain-kit (Vector Laboratories) according to the manufacturer's protocol. Hematoxylin-Eosin (HE) stainings were performed according to standard procedures. Cells of the granulocytic lineage were stained on paraffin-embedded tissues with the Naphthol AS-D Chloracetate (Specific Esterase, CAE) Kit (Ref: 91C-1KT, Sigma-Aldrich) according to the manufacturer's protocol.

In the in vivo therapeutic experiments, we calculated the narrowing of the spinal cord using the equation $A_t/(A_{sca}–A_{sp})$, where A_{sca} is the area of the spinal canal, A_t that of the tumor, and A_{sp} that of the spinal cord area. Two different cross-sections per animal were examined. The infiltration of the liver was calculated by dividing the tumor area in the liver by the whole area of the liver section. Three whole liver sections were analyzed per animal. All measurements were performed using Fijii [56].

Whole-exome sequencing and biostatistical analysis

To determine SNV within leukemia samples, genomic (g)DNA was extracted both from primary $Irf4^{-/-}$ tumors as well as FACS-sorted control $B220^+sIg\mu^-$ BM fr.A-D cells using the High Pure PCR Template Preparation kit from Roche (11796828001). The integrity of the resultant gDNA was confirmed in a 2% Agarose gel. Macrogen in Seoul performed SureSelect All Exon V6 library preparation and sequenced exons on a NovaSeq platform producing 2 × 150 bp reads at a coverage of 100× (50× on-target coverage). Fastq quality control was performed using FASTQC (version 0.11.9). Raw sequenced reads were aligned to the Ensembl Mus musculus reference (revision 96) using STAR (version 2.6.1d) using default parametrization. Soft-clipped aligned reads were then subjected to variant calling analysis. Position-wise pile-up files were generated using samtools (version 1.9) with the mpileup option and a pile-up quality threshold of 15, both for single sample and matched variant calling. Subsequently, variant calling was performed for SNP and InDel detection using VarScan2 (version 2.3.9) on single samples with the following parametrization: sampling depth = 100,000, minimum variant frequency = 0.05, minimum coverage = 8, minimum variant reads = 2, minimum average read quality = 15 and a *p* value threshold was set to 0.05. Only primary alignments were considered, the strand filter was enabled, and duplicates were removed. As a comparison, matched tumor-normal variant calling was performed with VarScan as well using an identical parameter setting with the somatic *p* value threshold set to 0.05.

For Fig. 3n raw sequenced reads were aligned to the Ensembl Mus musculus reference (revision 96) using Burrows-Wheeler Aligner (BWA version 0.7.17) using default parametrization [57]. Prior to variant calling, aligned reads were filtered using a custom filter that excludes reads with more than three mismatches, more than two indels, or a mapping quality below 20 using pysam (version 0.16.0.1). Duplicates were marked and removed using Picard (GATK version 4.1.6.0) [58]. Filtered aligned reads were then subjected to variant calling analysis. Position-wise pile-up files were generated using samtools (version 1.9) with the mpileup option and a minimal base quality threshold of 20. Subsequently, variant calling performed for SNP detection using VarScan2 (version 2.4.4) using matched tumor-normal (somatic) mode with the following parametrization: sampling depth = 100,000, minimum variant frequency = 0.2, minimum coverage = 8, minimum variant supporting reads = 5, minimum average read quality = 20 and a somatic *p* value threshold was set to 0.05. Only primary alignments were considered, and the strand filter was enabled. SNP calls were filtered to high confidence somatic mutations using VarScan's somaticFilter method, SNPs with a variant allele frequency above 0 in the matched reference sample were excluded.

Sanger sequencing and polymerase chain reaction

SNVs in the JAK3 gene were confirmed by Sanger sequencing of PCR fragments spanning the *Jak3* pseudokinase and kinase region (primers

used for PCR amplification and Sanger Sequencing: mJAK3 for, mJAK3 rev s. Supplemental Data). Sequencing services were provided by Microsynth Seqlab. To determine the clonality of tumor cells, the VμH region was amplified by PCR. Amplicons were run on an agarose gel and extracted using the QIAquick Gel Extraction Kit (Qiagen). DNA fragments were then cloned into the vector pJet1.2 (Thermo Scientific) and transformed into DH10B E. coli. The indicated numbers of clones (Fig. 1g) for each PCR amplicon were sequenced and aligned with software from IMGT/V-quest [59].

Retroviral transduction of *Jak3*-mutants and IL-7 independency assay

The coding sequence of murine *Jak3* was amplified from pCineo-Jak3 (a gift from Olli Silvennoinen from Tampere-university in Finland) and cloned into the pMSCV-Thy1.1 expression plasmid using *BamHI* and *SalI* restriction digestion. Site-directed mutagenesis was performed following the manufacturer's protocol using the Quick-Change II site-directed mutagenesis kit (Agilent Technologies; primers employed are listed in the Supplemental Materials). Viral supernatant from mutated pMSCV-Thy1.1-Jak3 constructs was produced as described previously [49]. For viral transduction, 5×10^5 IL-7 dependent primary *Irf4*$^{-/-}$ preB-I cell cultures were resuspended in 400 µL RPMI medium (D5030, Sigma-Aldrich) with 600 µL viral supernatant and 1.5 µL polybrene and spun in culture plates at 2700 rpm for 90 min at 37 °C. Cells were then replenished with a conditioned medium and rested for 24 h. Transduction efficiency was measured by flow cytometry using surface staining for Thy1.1 (OX-70, Biolegend). For the IL-7 independency assay (Fig. 3b), transduced cells were split and cultured with either recombinant murine (rm)IL-7 or 10 µg/ml neutralizing anti-IL-7 antibody (BE0048, Bio X Cell).

RNA-sequencing and biostatistical analysis

RNA extraction from primary tumor samples and FACS-sorted B220$^+$ slgμ$^-$ pro/preB cells was performed using Trizol extraction. Quality control was performed using the Bioanalyzer RNA 6000 NanoChip (Agilent Technologies). Library preparation was performed at the Institute for Immunology, University Medical Center of the Johannes Gutenberg-University Mainz using the NEBNext Ultra Library Prep kit (New England Biolabs). For deep sequencing, the Illumina-HiSeq- 4000 platform was used (Beijing Genomic Institute). Quality control on the sequencing data were performed with the FastQC tool (version 0.11.2, https://www.bioinformatics.babraham.ac.uk/projects/fastqc/). RNA-sequencing reads were aligned to the ENSEMBL Mus_musculus.GRCm38 reference genome. The corresponding annotation (ENSEMBL v76) was also retrieved from ENSEMBL FTP website. The STAR aligner (version 2.4.0j) was used to perform mapping to the reference genome. Alignments were processed with the featureCounts function [60] of the Rsubread package, using the annotation file also used for supporting the alignment. Exploratory Data Analysis was performed with the pcaExplorer package [61]. Differential expression analysis was performed with DESeq2 package [62], setting the false discovery rate (FDR) cutoff to 0.1. DESeq2 datasets were analyzed using the GeneTonic [63] and pcaExplorer packages. To assess the possible occurrence of gene fusions, we applied two different methods, Star-Fusion (version 1.10.1) and Arriba (version 2.1.0). For STAR-Fusion, required meta reference files were created from the Ensembl Mus musculus reverence (revision 100) as recommended in the STAR-Fusion manual. In case of Arriba, we used the mm10 + GENCODEM25 assembly. In each case, we used the dockerized versions of the tools. Raw fastq files were used as an input for both tools. Subsequently, raw reads were mapped using the recommended alternative STAR settings recommended in the tools manual to leverage chimeric reads from the alignments. Default filters as recommended by the STAR-Fusion and Arriba manuals were applied to limit the false-positive rate. For the same reason, known blacklisted regions as provided by the Arriba release were excluded from the analysis.

BCP-ALL subtype predictions using random forest classifier

Human genes (GRCh38.p13, v104) with annotated orthologous genes in mice were extracted from ensembl database using the BiomaRt online tool. Gene counts from RNA-sequencing of a previously published human BCP-ALL cohort [28] and of murine tumor samples were subsetted to include only human-mouse orthologous genes. The resulting gene counts were normalized by variant stabilization transformation using the R package DESeq2 version 1.32.0. Allocation of the murine tumor samples to human BCP-ALL molecular subtypes was performed based on gene expression using a random forest machine learning algorithm (R package caret version 6.0-88) trained on the human cohort. Predictions were plotted using R package pheatmap version 1.0.12. Differential gene expression was analyzed in R package DESeq2 and resulting gene lists ranked by log2-fold-change were analyzed in GSEA version 4.1.0.

JAK structure and sequence analysis

Mouse JAK2 (AF-Q62120) and JAK3 (AF-Q62137) structure predictions were acquired from the AlphaFold protein structure database [64] and visualized in UCSF ChimeraX (version 1.2.5) [65]. Multiple sequence alignments were performed using the EMBL-EBI Clustal Omega tool.

Quantitative real-time (qRT-)PCR

Total RNA was extracted both from primary *Irf4*$^{-/-}$ tumors as well as FACS-sorted control B220$^+$slgμ$^-$ BM fr.A-D cells of either *Irf4*$^{-/-}$ or wt animals using the Gdansk extractme kit (EM09.1) according to the manufacturer's protocol. cDNA was prepared from whole RNA samples using the RevertAid cDNA kit from Thermo Fisher (K1621). qRT-PCR for *Aicda*, *Spi1*, and *Pax5* was performed using the SybrGreen MasterMix reagent (4385612, AppliedBiosystems) in a StepOnePlus cycler (AppliedBiosystems). Data presented as percentage of HPRT using the formula $x = 1/2^{(\text{cyclesAicda} - \text{cyclesHPRT})} \times 100$.

In vivo therapeutic studies and ultrasound imaging

Mice were injected with 3×10^5 T8.1 cells intraperitoneally and monitored daily for clinical symptoms. When mice began showing signs of general morbidity, leukemia was confirmed by FACS analysis of tail vein blood for B220$^+$ slgμ$^-$ blast cells. When blast cells in pB reached 25 (mean 50)%, therapy was initiated with oral Dexamethasone (Jenapharm) at 6 mg/L supplied ad libitum in the drinking water for seven days. Maintenance therapy comprised either Ruxolitinib-phosphate (S5243, Sellekchem) 1 mg (in 2% DMSO, 30% PEG300 in H_2O, as proposed by the manufacturer), Defactinib (S7654, Sellekchem) 1.2 mg (in 5% DMSO, 50% PEG300, 5% Tween 80 in H_2O, as proposed by the manufacturer) or vehicle control (5% DMSO, 50% PEG300, 5% Tween 80 in H_2O) administered twice daily via oral gavage. During the course of the disease, this treatment led to paraparesis of the hind legs and tail. A clinical scoring system was established according to the extent of paraparesis and mice were scored daily accordingly: Scores 0–3: (0) no paraparesis, (1) paraparesis induced by treatment intervention, resolves within 30 s, (2) paraparesis induced by treatment intervention, does not resolve within 30 s, (3) persistent paraparesis, independent of treatment intervention. Score 3 prompted sacrification of affected mice. High-resolution ultrasound imaging was performed using a Visual Sonics Vevo 2100 System (FUJIFILM VisualSonics, Toronto, Canada) with microscan transducer MS-550-D, 22–55 MHz (FUJIFILM VisualSonics, Toronto, Canada) as described previously [66].

Statistical analysis

Statistical analysis was performed using the GraphPad 9.0 software. Data are commonly presented as mean ± SD. Prior to significance testing, normal distribution and homogeneity of variances were confirmed by Shapiro–Wilk test and Brown–Forsythe testing. Statistical significance when comparing two normally distributed groups was evaluated using two-tailed unpaired *t* tests. In case of significant differences in variances between groups, Welch's correction was applied to account for non-norminal distribution of data. When comparing multiple groups, a one-way or two-way analysis of variance was performed, depending on the number of variables that differed between compared groups. This was followed by a Tukey's Sidak, or Dunnett's *post hoc* test, as indicated in figure legends. An alpha level of $P < 0.05$ was employed for significance testing. In the in vivo experiment, all animals were included in the analyses.

Reporting summary

Further information on research design is available in the Nature Research Reporting Summary linked to this article.

DATA AVAILABILITY

The RNAseq datasets generated during the current study have been deposited in the Gene Expression Omnibus (GEO) archive and are available under the accession number GSE192424. The WES datasets can be accessed under PRJNA706650 in the sequencing read archive (SRA).

REFERENCES

1. Johnson K, Hashimshony T, Sawai CM, Pongubala JMR, Skok JA, Aifantis I, et al. Regulation of immunoglobulin light-chain recombination by the transcription factor IRF-4 and the attenuation of interleukin-7 signaling. Immunity 2008;28:335–45.
2. Geier JK, Schlissel MS. Pre-BCR signals and the control of Ig gene rearrangements. Semin Immunol 2006;18:31–9.
3. Herzog S, Reth M, Jumaa H. Regulation of B-cell proliferation and differentiation by pre-B-cell receptor signalling. Nat Rev Immunol 2009;9:195–205.
4. Fistonich C, Zehentmeier S, Bednarski JJ, Miao R, Schjerven H, Sleckman BP, et al. Cell circuits between B cell progenitors and IL-7+ mesenchymal progenitor cells control B cell development cell circuits control B cell development. J Exp Med2018;215:2586–99.
5. Huber M, Lohoff M. IRF4 at the crossroads of effector T-cell fate decision. Eur J Immunol 2014;44:1886–95.
6. Lohoff M, Mak TW. Roles of interferon-regulatory factors in T-helper-cell differentiation. Nat Rev Immunol 2005;5:125–35.
7. Mittrücker H-W, Matsuyama T, Grossman A, Kündig TM, Potter J, Shahinian A, et al. Requirement for the transcription factor LSIRF/IRF4 for mature B and T lymphocyte function. Science 1997;275:540–3.
8. Lu R, Medina KL, Lancki DW, Singh H. IRF-4,8 orchestrate the pre-B-to-B transition in lymphocyte development. Gene Dev 2003;17:1703–8.
9. Katz AJ, Chia VM, Schoonen WM, Kelsh MA. Acute lymphoblastic leukemia: an assessment of international incidence, survival, and disease burden. Cancer Cause Control 2015;26:1627–42.
10. Tasian SK, Hurtz C, Wertheim GB, Bailey NG, Lim MS, Harvey RC, et al. High incidence of Philadelphia chromosome-like acute lymphoblastic leukemia in older adults with B-ALL. Leukemia 2016;31:981–4.
11. Roberts KG. Genetics and prognosis of ALL in children vs adults. Hematol Am Soc Hematol Educ Program 2018;2018:137–45.
12. Mullighan CG. Genomic characterization of childhood acute lymphoblastic leukemia. Semin Hematol 2013;50:314–24.
13. Liu Y-F, Wang B-Y, Zhang W-N, Huang J-Y, Li B-S, Zhang M, et al. Genomic profiling of adult and pediatric b-cell acute lymphoblastic leukemia. Ebiomedicine 2016;8:173–83.
14. Hardy RR, Carmack CE, Shinton SA, Kemp JD, Hayakawa K. Resolution and characterization of pro-B and pre-pro-B cell stages in normal mouse bone marrow. J Exp Med 1991;173:1213–25.
15. Sen J, Arceci RJ, Jones W, Burakoff SJ. Expression and ontogeny of murine CD2. Eur J Immunol 1989;19:1297–302.
16. Zehentmeier S, Pereira JP. Cell circuits and niches controlling B cell development. Immunol Rev 2019;289:142–57.
17. Tokoyoda K, Egawa T, Sugiyama T, Choi B-I, Nagasawa T. Cellular niches controlling B lymphocyte behavior within bone marrow during development. Immunity 2004;20:707–18.
18. Ma Q, Jones D, Springer TA. The chemokine receptor CXCR4 is required for the retention of B lineage and granulocytic precursors within the bone marrow microenvironment. Immunity 1999;10:463–71.
19. Batista CR, Lim M, Laramée A-S, Abu-Sardanah F, Xu LS, Hossain R, et al. Driver mutations in Janus kinases in a mouse model of B-cell leukemia induced by deletion of PU.1 and Spi-B. Blood Adv 2018;2:2798–810.
20. Roberts KG, Li Y, Payne-Turner D, Harvey RC, Yang Y-L, Pei D, et al. Targetable kinase-activating lesions in Ph-like acute lymphoblastic leukemia. N. Engl J Med 2014;371:1005–15.
21. Refsland EW, Harris RS. The APOBEC3 family of retroelement restriction factors. Curr Top Microbiol 2013;371:1–27.
22. Petersen-Mahrt SK, Harris RS, Neuberger MS. AID mutates E. coli suggesting a DNA deamination mechanism for antibody diversification. Nature 2002;418: 99–104.
23. Noia JD, Neuberger MS. Altering the pathway of immunoglobulin hypermutation by inhibiting uracil-DNA glycosylase. Nature 2002;419:43–8.
24. Wilson TM, Vaisman A, Martomo SA, Sullivan P, Lan L, Hanaoka F, et al. MSH2–MSH6 stimulates DNA polymerase η, suggesting a role for A:T mutations in antibody genes. J Exp Med 2005;201:637–45.
25. Swaminathan S, Klemm L, Park E, Papaemmanuil E, Ford A, Kweon S-M, et al. Mechanisms of clonal evolution in childhood acute lymphoblastic leukemia. Nat Immunol 2015;16:766–74.
26. Malard F, Mohty M. Acute lymphoblastic leukaemia. Lancet 2020;395:1146–62.
27. Mullighan CG. How advanced are we in targeting novel subtypes of ALL? Best Pract Res Clin Haematol 2019;32:101095.
28. Bastian L, Schroeder MP, Eckert C, Schlee C, Tanchez JO, Kämpf S, et al. PAX5 biallelic genomic alterations define a novel subgroup of B-cell precursor acute lymphoblastic leukemia. Leukemia 2019;33:1895–909.
29. Jain N, Roberts KG, Jabbour E, Patel K, Eterovic AK, Chen K, et al. Ph-like acute lymphoblastic leukemia: a high-risk subtype in adults. Blood 2017;129:572–81.
30. Jumper J, Evans R, Pritzel A, Green T, Figurnov M, Ronneberger O, et al. Highly accurate protein structure prediction with AlphaFold. Nature 2021;596:583–9.
31. Herold T, Schneider S, Metzeler K, Neumann M, Hartmann L, Roberts KG, et al. Philadelphia chromosome-like acute lymphoblastic leukemia in adults have frequent IGH-CRLF2 and JAK2 mutations, persistence of minimal residual disease and poor prognosis. Haematologica. 2016;102:130–8.
32. Corfe SA, Paige CJ. The many roles of IL-7 in B cell development; mediator of survival, proliferation and differentiation. Semin Immunol 2012;24:198–208.
33. Milford TM, Su RJ, Francis OL, Baez I, Martinez SR, Coats JS, et al. TSLP or IL-7 provide an IL-7Rα signal that is critical for human B lymphopoiesis. Eur J Immunol 2016;46:2155–61.
34. Härzschel A, Zucchetto A, Gattei V, Hartmann TN. VLA-4 expression and activation in B cell malignancies: functional and clinical aspects. Int J Mol Sci 2020;21:2206.
35. Springer TA. Adhesion receptors of the immune system. Nature 1990;346:425–34.
36. Tijchon E, Havinga J, Leeuwen FNvan, Scheijen B. B-lineage transcription factors and cooperating gene lesions required for leukemia development. Leukemia 2013;27:541–52.
37. Martin-Lorenzo A, Hauer J, Vicente-Duenas C, Auer F, Gonzalez-Herrero I, Garcia-Ramirez I, et al. Infection exposure is a causal factor in B-cell precursor acute lymphoblastic leukemia as a result of Pax5-inherited susceptibility. Cancer Discov 2015;5:1328–43.
38. Schjerven H, Ayongaba EF, Aghajanirefah A, McLaughlin J, Cheng D, Geng H, et al. Genetic analysis of Ikaros target genes and tumor suppressor function in BCR-ABL1+ pre–B ALLIkaros tumor suppressor function in Ph+ pre–B ALL. J Exp Med 2017;214:793–814.
39. Pang SHM, Minnich M, Gangatirkar P, Zheng Z, Ebert A, Song G, et al. PU.1 cooperates with IRF4 and IRF8 to suppress pre-B-cell leukemia. Leukemia 2016;30:1375–87.
40. Jo S-H, Schatz JH, Acquaviva J, Singh H, Ren R. Cooperation between deficiencies of IRF-4 and IRF-8 promotes both myeloid and lymphoid tumorigenesis. Blood 2010;116:2759–67.
41. Lupardus PJ, Ultsch M, Wallweber H, Kohli PB, Johnson AR, Eigenbrot C. Structure of the pseudokinase–kinase domains from protein kinase TYK2 reveals a mechanism for Janus kinase (JAK) autoinhibition. Proc Natl Acad Sci 2014;111:8025–30.
42. McElroy CA, Holland PJ, Zhao P, Lim J-M, Wells L, Eisenstein E, et al. Structural reorganization of the interleukin-7 signaling complex. Proc Natl Acad Sci 2012;109:2503–8.
43. Hertzberg L, Vendramini E, Ganmore I, Cazzaniga G, Schmitz M, Chalker J, et al. Down syndrome acute lymphoblastic leukemia, a highly heterogeneous disease in which aberrant expression of CRLF2 is associated with mutated JAK2: a report from the International BFM Study Group. Blood 2010;115:1006–17.
44. Tasian SK, Assad A, Hunter DS, Du Y, Loh ML. A Phase 2 study of ruxolitinib with chemotherapy in children with philadelphia chromosome-like acute lymphoblastic leukemia (INCB18424-269/AALL1521): dose-finding results from the part 1 safety phase. Blood 2018;132:555–555.
45. Verstovsek S, Mesa RA, Gotlib J, Levy RS, Gupta V, DiPersio JF, et al. A double-blind, placebo-controlled trial of ruxolitinib for myelofibrosis. N. Engl J Med 2012;366:799–807.
46. Hara T, Shitara S, Imai K, Miyachi H, Kitano S, Yao H, et al. Identification of IL-7–producing cells in primary and secondary lymphoid organs using IL-7–GFP knock-in mice. J Immunol 2012;189:1577–84.
47. Ogawa M, Nishikawa S, Ikuta K, Yamamura F, Naito M, Takahashi K, et al. B cell ontogeny in murine embryo studied by a culture system with the monolayer of a stromal cell clone, ST2: B cell progenitor develops first in the embryonal body rather than in the yolk sac. Embo J 1988;7:1337–43.
48. Ceredig R, Boekel Eten, Rolink A, Melchers F, Andersson J. Fetal liver organ cultures allow the proliferative expansion of pre-B receptor-expressing pre-B-II cells and the differentiation of immature and mature B cells in vitro. Int Immunol 1998;10:49–59.
49. Kang CH, Hartmann E, Menke L, Staudenraus D, Abass E-F, Raifer H, et al. A hyperactive mutant of interferon-regulatory factor 4. Eur J Immunol 2018;49:812–5.
50. Maaten LVD, Hinton G. Visualizing data using t-SNE. J Mach Learn Res 2008;9:2579–625.
51. Langmead B, Salzberg SL. Fast gapped-read alignment with Bowtie 2. Nat Methods 2012;9:357–9.
52. Klambauer G, Schwarzbauer K, Mayr A, Clevert D-A, Mitterecker A, Bodenhofer U, et al. cn.MOPS: mixture of Poissons for discovering copy number variations in next-generation sequencing data with a low false discovery rate. Nucleic Acids Res 2012;40:e69.
53. Kawamoto T. Use of a new adhesive film for the preparation of multi-purpose fresh-frozen sections from hard tissues, whole-animals, insects and plants. Arch Histol Cytol 2003;66:123–43.
54. Zehentmeier S, Roth K, Cseresnyes Z, Sercan Ö, Horn K, Niesner RA, et al. Static and dynamic components synergize to form a stable survival niche for bone marrow plasma cells. Eur J Immunol 2014;44:2306–17.

55. Canene-Adams K. Preparation of formalin-fixed paraffin-embedded tissue for immunohistochemistry. Methods Enzymol 2013;533:225–33.
56. Schindelin J, Arganda-Carreras I, Frise E, Kaynig V, Longair M, Pietzsch T, et al. Fiji: an open-source platform for biological-image analysis. Nat Methods 2012;9:676–82.
57. Li H, Durbin R. Fast and accurate short read alignment with Burrows–Wheeler transform. Bioinformatics 2009;25:1754–60.
58. McKenna A, Hanna M, Banks E, Sivachenko A, Cibulskis K, Kernytsky A, et al. The genome analysis toolkit: a MapReduce framework for analyzing next-generation DNA sequencing data. Genome Res 2010;20:1297–303.
59. Brochet X, Lefranc M-P, Giudicelli V. IMGT/V-QUEST: the highly customized and integrated system for IG and TR standardized V-J and V-D-J sequence analysis. Nucleic Acids Res 2008;36:W503–8.
60. Liao Y, Smyth GK, Shi W. featureCounts: an efficient general purpose program for assigning sequence reads to genomic features. Bioinformatics 2014;30:923–30.
61. Marini F, Binder H. pcaExplorer: an R/Bioconductor package for interacting with RNA-seq principal components. BMC Bioinformatics 2019;20:331.
62. Love MI, Huber W, Anders S. Moderated estimation of fold change and dispersion for RNA-seq data with DESeq2. Genome Biol 2014;15:550.
63. Marini F, Ludt A, Linke J, Strauch K. GeneTonic: an R/Bioconductor package for streamlining the interpretation of RNA-seq data. *Biorxiv*. 2021; https://www.biorxiv.org/content/10.1101/2021.05.19.444862v1.
64. Varadi M, Anyango S, Deshpande M, Nair S, Natassia C, Yordanova G, et al. AlphaFold Protein Structure Database: massively expanding the structural coverage of protein-sequence space with high-accuracy models. Nucleic Acids Res. 2021;50:D439–D444.
65. Pettersen EF, Goddard TD, Huang CC, Meng EC, Couch GS, Croll TI, et al. UCSF ChimeraX: structure visualization for researchers, educators, and developers. Protein Sci 2021;30:70–82.
66. Buchholz SM, Goetze RG, Singh SK, Ammer-Herrmenau C, Richards FM, Jodrell DI, et al. Depletion of macrophages improves therapeutic response to gemcitabine in murine pancreas cancer. Cancers 2020;12:1978.

ACKNOWLEDGEMENTS

The authors want to thank Koji Tokoyoda (DRFZ, Berlin) for supplying *Il-7*^{eGFP} mice for breeding, Olli Silvennoinen (Tampere-university, Finland) for supplying us with the JAK3 construct, and Fritz Melchers (DRFZ Berlin) for the JIL-7.6 J558 and ST2 cells. Further, Hyun-Dong Chang and Anja Hauser (both DRFZ, Berlin) for supplying OP-9 cells and Kawamoto materials, respectively.

AUTHOR CONTRIBUTIONS

DDG, CP, NS, MB, FH, ML designed experiments; DDG, CP, NS, MB, DS, LM, BC, FH, LH performed experiments; DDG, CP, MB, HR, ER, PD, MW, MM, AN, UMB, FM, FH, MB, HMJ, AN, AB, MK, TB, TS, AP, LB, AH, CB, ML analyzed data; DDG and ML prepared the manuscript.

FUNDING

D.D.G. received personal funding through the German Cancer Aid, Mildred-Scheel doctoral scholarship (70112922). M.L. was funded by the Deutsche Forschungsgemeinschaft (DFG) (LO 396/8-1) and the Else Kröner-Fresenius-Stiftung. Open Access funding enabled and organized by Projekt DEAL.

COMPETING INTERESTS

The authors declare no competing interests.

STUDY APPROVAL

All animal experiments were approved by the local government (Regierungspräsidium Gießen, G49/2018, G34/2021) and conducted according to the German animal protection law.

ADDITIONAL INFORMATION

Supplementary information The online version contains supplementary material available at https://doi.org/10.1038/s41418-022-01005-z.

Correspondence and requests for materials should be addressed to Michael Lohoff.

Reprints and permission information is available at http://www.nature.com/reprints

Publisher's note Springer Nature remains neutral with regard to jurisdictional claims in published maps and institutional affiliations.

Cell Metabolism

Article

Glutathione Restricts Serine Metabolism to Preserve Regulatory T Cell Function

Graphical Abstract

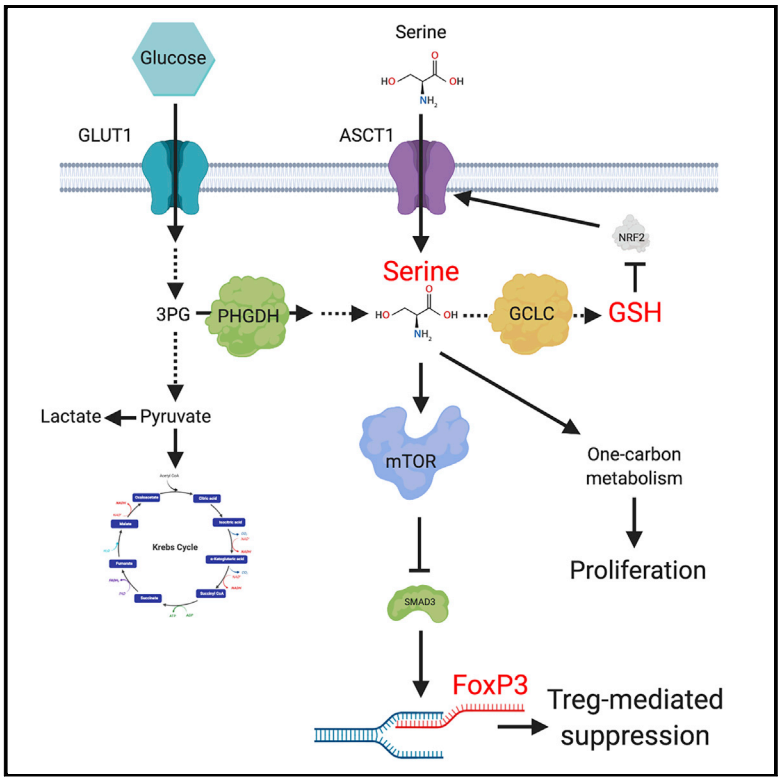

Highlights

- Ablation of *Gclc* in Tregs causes autoimmunity and increases anti-tumor responses
- *Gclc*-derived GSH is needed for the suppressive function of Tregs *in vitro* and *in vivo*
- GSH in Tregs regulates serine concentrations and metabolism. which impact mTOR and FoxP3
- Serine- and glycine-deficient diet rescues mutant mice from lethal inflammation

Authors

Henry Kurniawan, Davide G. Franchina, Luana Guerra, ..., Johannes Meiser, Karsten Hiller, Dirk Brenner

Correspondence

dirk.brenner@lih.lu

In Brief

Regulatory T cells (Tregs) rely on oxidative metabolism, which triggers the generation of reactive oxygen species (ROS). Accumulating ROS are controlled by the antioxidant glutathione (GSH). Kurniawan et al. reveal an unexpected subset-specific role of GSH in serine metabolism and Treg function.

Kurniawan et al., 2020, Cell Metabolism *31*, 920–936
May 5, 2020
https://doi.org/10.1016/j.cmet.2020.03.004

CellPress

CellPress

Cell Metabolism

Article

Glutathione Restricts Serine Metabolism to Preserve Regulatory T Cell Function

Henry Kurniawan,[1] Davide G. Franchina,[1] Luana Guerra,[1] Lynn Bonetti,[1] Leticia Soriano - Baguet,[1] Melanie Grusdat,[1] Lisa Schlicker,[2,3] Oliver Hunewald,[4] Catherine Dostert,[1] Myriam P. Merz,[5] Carole Binsfeld,[1] Gordon S. Duncan,[6] Sophie Farinelle,[1] Yannic Nonnenmacher,[2,3] Jillian Haight,[6] Dennis Das Gupta,[7] Anouk Ewen,[1] Rabia Taskesen,[12] Rashi Halder,[8] Ying Chen,[9] Christian Jäger,[8] Markus Ollert,[4,10] Paul Wilmes,[8] Vasilis Vasiliou,[9] Isaac S. Harris,[11] Christiane B. Knobbe-Thomsen,[12] Jonathan D. Turner,[5] Tak W. Mak,[6,12,13] Michael Lohoff,[7] Johannes Meiser,[14] Karsten Hiller,[2,3] and Dirk Brenner[1,10,15,16,*]

[1]Experimental & Molecular Immunology, Department of Infection and Immunity, Luxembourg Institute of Health, 29 Rue Henri Koch, Esch-sur-Alzette, Luxembourg

[2]Braunschweig Integrated Center of Systems Biology (BRICS), Technische Universität Braunschweig, Rebenring 56, 38106 Braunschweig

[3]Computational Biology of Infection Research, Helmholtz Centre for Infection Research, Inhoffenstraße 7, 38124 Braunschweig, Germany

[4]Allergy and Clinical Immunology, Department of Infection and Immunity, Luxembourg Institute of Health, 29 Rue Henri Koch, L-4354 Esch-sur-Alzette, Luxembourg

[5]Immune Endocrine Epigenetics Research Group, Department of Infection and Immunity, Luxembourg Institute of Health, 29 Rue Henri Koch, L-4354 Esch-sur-Alzette, Grand Duchy of Luxembourg

[6]The Campbell Family Cancer Research Institute, Ontario Cancer Institute University Health Network, Toronto, ON, Canada

[7]Institute for Medical Microbiology and Hospital Hygiene, University of Marburg, Marburg, Germany

[8]Luxembourg Centre for Systems Biomedicine, University of Luxembourg, 7 Avenue des Hauts Fourneaux, Esch-sur-Alzette, Luxembourg

[9]Department of Environmental Health Sciences, Yale School of Public Health, New Haven, CT, USA

[10]Odense Research Center for Anaphylaxis (ORCA), Department of Dermatology and Allergy Center, Odense University Hospital, University of Southern Denmark, Odense, Denmark

[11]Department of Biomedical Genetics and Wilmot Cancer Institute, University of Rochester Medical Center, 601 Elmwood Ave, Rochester, New York, USA

[12]Departments of Medical Biophysics and Immunology, Faculty of Medicine, University of Toronto, Toronto, ON, Canada

[13]The University of Hong Kong, Hong Kong SAR, China

[14]Cancer Metabolism Group, Department of Oncology, 84 Val Fleuri, Luxembourg, Luxembourg

[15]Immunology & Genetics, Luxembourg Centre for Systems Biomedicine, University of Luxembourg, 7 Avenue des Hauts Fourneaux, Esch-sur-Alzette, Luxembourg

[16]Lead Contact

*Correspondence: dirk.brenner@lih.lu

https://doi.org/10.1016/j.cmet.2020.03.004

SUMMARY

Regulatory T cells (Tregs) maintain immune homeostasis and prevent autoimmunity. Serine stimulates glutathione (GSH) synthesis and feeds into the one-carbon metabolic network (1CMet) essential for effector T cell (Teff) responses. However, serine's functions, linkage to GSH, and role in stress responses in Tregs are unknown. Here, we show, using mice with Treg-specific ablation of the catalytic subunit of glutamate cysteine ligase (*Gclc*), that GSH loss in Tregs alters serine import and synthesis and that the integrity of this feedback loop is critical for Treg suppressive capacity. Although *Gclc* ablation does not impair Treg differentiation, mutant mice exhibit severe autoimmunity and enhanced anti-tumor responses. *Gclc*-deficient Tregs show increased serine metabolism, mTOR activation, and proliferation but downregulated FoxP3. Limitation of cellular serine *in vitro* and *in vivo* restores FoxP3 expression and suppressive capacity of *Gclc*-deficient Tregs. Our work reveals an unexpected role for GSH in restricting serine availability to preserve Treg functionality.

Context and Significance

Regulatory T cells (Tregs) restrict inflammation to maintain healthy body functions. Dysregulation of Treg metabolism thus leads to inflammatory disease; however, our knowledge of their metabolic needs is limited. Researchers of the Luxembourg Institute of Health describe a novel metabolic control mechanism in Tregs that serves as a barrier against autoimmunity. The antioxidant glutathione restricts serine metabolism in Tregs to preserve their suppressive function such that glutathione depletion boosts anti-tumor immunity. Glutathione is thus a stress sensor in Tregs whose manipulation holds promise for anti-inflammatory and anti-tumor therapies. The authors further show that elucidation of the metabolic mechanism of a disease can lead to its mitigation by a rationally designed diet, setting a new direction for future treatment of metabolic diseases.

INTRODUCTION

Tregs suppress Teffs to maintain peripheral tolerance and prevent autoimmunity (Wing and Sakaguchi, 2010). Metabolic reprogramming in activated Tregs is distinct from that in Teffs (Dang et al., 2011; Delgoffe et al., 2009; Shi et al., 2011), implying that specific nutrients may affect the function and differentiation of T cell subsets differently.

Serine is a non-essential amino acid (NEAA) and fosters Teff function (Ma et al., 2017; Ron-Harel et al., 2016), but its role in Tregs is unknown. Serine is either taken up directly by cells or synthesized *de novo* from the glycolytic metabolite 3-phosphoglycerate (3-PG). Intracellular serine is the major carbon source for folate-mediated one-carbon metabolism (1CMet), which operates in the cytosol and mitochondria to provide building blocks for S-adenosylmethionine (SAM), nucleotides, NAD(P)H, and ATP. 1CMet thus supports AA homeostasis, epigenetic maintenance, and redox defense (Ducker and Rabinowitz, 2017; Tibbetts and Appling, 2010). Serine is also a source of glycine and cysteine used to synthesize glutathione (GSH), the main antioxidant preserving intracellular redox balance (Meister, 1983; Ye et al., 2014). GSH, composed of glycine, glutamine, and cysteine, is synthesized by glutamate cysteine ligase (GCL; containing Gclc and Gclm subunits) and glutathione synthase (Lu, 2009). GSH is vital for Teff functions and proliferation (Mak et al., 2017).

We report here, using Treg-specific *Gclc*-deficient mice, that a feedback loop involving GSH and serine unexpectedly regulates Treg functionality. GSH-deficient Tregs display increased serine uptake and *de novo* synthesis, enhancing 1CMet. Inhibition of serine uptake restores the suppressive capacity in *Gclc*-deficient Tregs. GSH not only controls a Treg's redox state but also acts as negative feedback regulator to restrict serine import and synthesis. Strikingly, GSH-deficient Tregs are linked to both autoimmunity and increased tumor rejection *in vivo*. Our results demonstrate a novel role for GSH in restricting serine metabolism to support Treg's suppressive capacity.

RESULTS

Gclc Ablation in Tregs Leads to Multi-organ Autoimmunity

Considering that Tregs rely on oxidative metabolism (Almeida et al., 2016; Pearce et al., 2013), we investigated whether wild-type (WT) Tregs generate more ROS than WT Teffs. Naive T cells isolated from C57BL/6 mice were treated *in vitro* with anti (α)-CD3 antibody (Ab), αCD28 Ab, and interleukin (IL)2, with or without transforming growth factor (TGF)β, to trigger the differentiation of induced Tregs (iTregs) or Th0 cells, respectively. Unexpectedly, ROS were lower (Figure 1A) but mitochondrial membrane potential and maximal oxygen consumption rate (OCR) were higher in WT iTregs compared to WT Th0 cells (Figures 1B and 1C), suggesting that ROS scavenging is very efficient in iTregs. In line, iTregs contained ~3-fold more GSH than Th0 cells (Figure 1D), conferring superior buffering of oxidative stress.

To explore GSH loss specifically in Tregs, we crossed *Gclc*$^{fl/fl}$ mice with *Foxp3*^{cre} mice to generate *Foxp3*^{cre}-*Gclc*$^{fl/fl}$ animals (Rubtsov et al., 2008). We isolated naive T cells from male mutants (6 week old) and *Gclc*$^{fl/fl}$ littermate controls and generated iTregs *in vitro*. Under conditions of optimal TCR stimulation, iTreg differentiation was not impaired by *Gclc* ablation (Figure 1E), and STAT5 phosphorylation (Figure S1A) and cell size (Figure S1B) were normal. In accordance with a previous report, suboptimal TCR stimulation of *Gclc*-deficient naive T cells led to more iTregs than in controls (Figure S1C) (Lian et al., 2018). Quantitative RT-PCR and mass spectrometry confirmed loss of *Gclc* mRNA and GSSG/GSH in mutant FoxP3$^+$ iTregs (Figures S1D and S1E), in line with their higher ROS (Figure S1F). *Gclc* deletion in all T cell subsets reduces CD4$^+$ and CD8$^+$ T cell numbers and homeostasis (Mak et al., 2017). However, Treg-specific *Gclc* deletion did not impair natural Treg (nTreg) homeostasis in the spleen or thymus of male mice. Indeed, percentages and absolute numbers of peripheral nTregs were slightly increased (Figures 1F and S1G).

By 8 weeks of age, male *Foxp3*^{cre}-*Gclc*$^{fl/fl}$ mice showed inflammation and reduced body weight and size (Figures 1G and S1H). By 12 weeks, most exhibited severe lymphadenopathy and splenomegaly (Figures 1H–1J) and a shorter lifespan (Figure 1K). Female *Foxp3*^{cre}-*Gclc*$^{fl/fl}$ mice, which possess an active *Foxp3*^{cre}-expressing or WT X chromosome and so retain some *Gclc*$^+$ nTregs, did not develop disease and had a normal lifespan (Figure 1K). Diseased male mice showed organ infiltration by T cells and macrophages (Figures 1L, S1I, and S1J) and increased serum anti-dsDNA Abs (Figure 1M). Thus, although *Gclc* ablation in Tregs does not impair Treg homeostasis, mice bearing these mutated cells develop multi-organ autoimmunity.

Teff Accumulation and Increased IFNγ Drive Lethal Auto-inflammation

Diseased male *Foxp3*^{cre}-*Gclc*$^{fl/fl}$ mice showed increased lymphocytic cellularity in the spleen and in lymph nodes (LN) (Figure 2A). Relative and absolute numbers of naive T cells (CD62L^{high}CD44^{low}) were decreased in the mutants, whereas the frequency and absolute numbers of activated CD4$^+$ and CD8$^+$ Teffs (CD62L^{low}CD44^{high}) were increased (Figures 2B, 2C, S2A, and S2B). These differences were not observed in female *Foxp3*^{cre}-*Gclc*$^{fl/fl}$ mice, indicating that non-targeted Tregs can suppress the inflammatory disease (Figure S2C). T cells from male *Foxp3*^{cre}-*Gclc*$^{fl/fl}$ mice produced more IFNγ, IL2 (CD4$^+$), and TNF (CD8$^+$), but not IL17 (CD4$^+$) (Figures 2D and 2E). Tbet expression was enhanced in mutant CD4$^+$ T cells (Figure S2D). ELISA confirmed high systemic levels of IFNγ, TNF, and IL2 in the serum of male mutants (Figure 2F). T cell frequencies, activation, and IFNγ production were increased in the lamina propria in male mutants (Figures S2E–S2G). T follicular helper cells (PD1$^+$CXCR5$^+$) and germinal center B cells (GL-7$^+$CD95$^+$) were elevated in mutant spleen (Figures S2H and S2I), and serum concentrations of IgG1, IgG2a, IgG3, and IgA were elevated (Figure S2J).

We next crossed male *Foxp3*^{cre}-*Gclc*$^{fl/fl}$ mice to *Ifn*$\gamma^{-/-}$ mice and monitored autoimmune disease onset in the progeny. *Ifn*γ deletion significantly reduced disease burden and prolonged survival (Figure 2G). Thus, *Gclc* function allows Tregs to suppress IFNγ-mediated autoimmunity and spontaneous Teff activation *in vivo*.

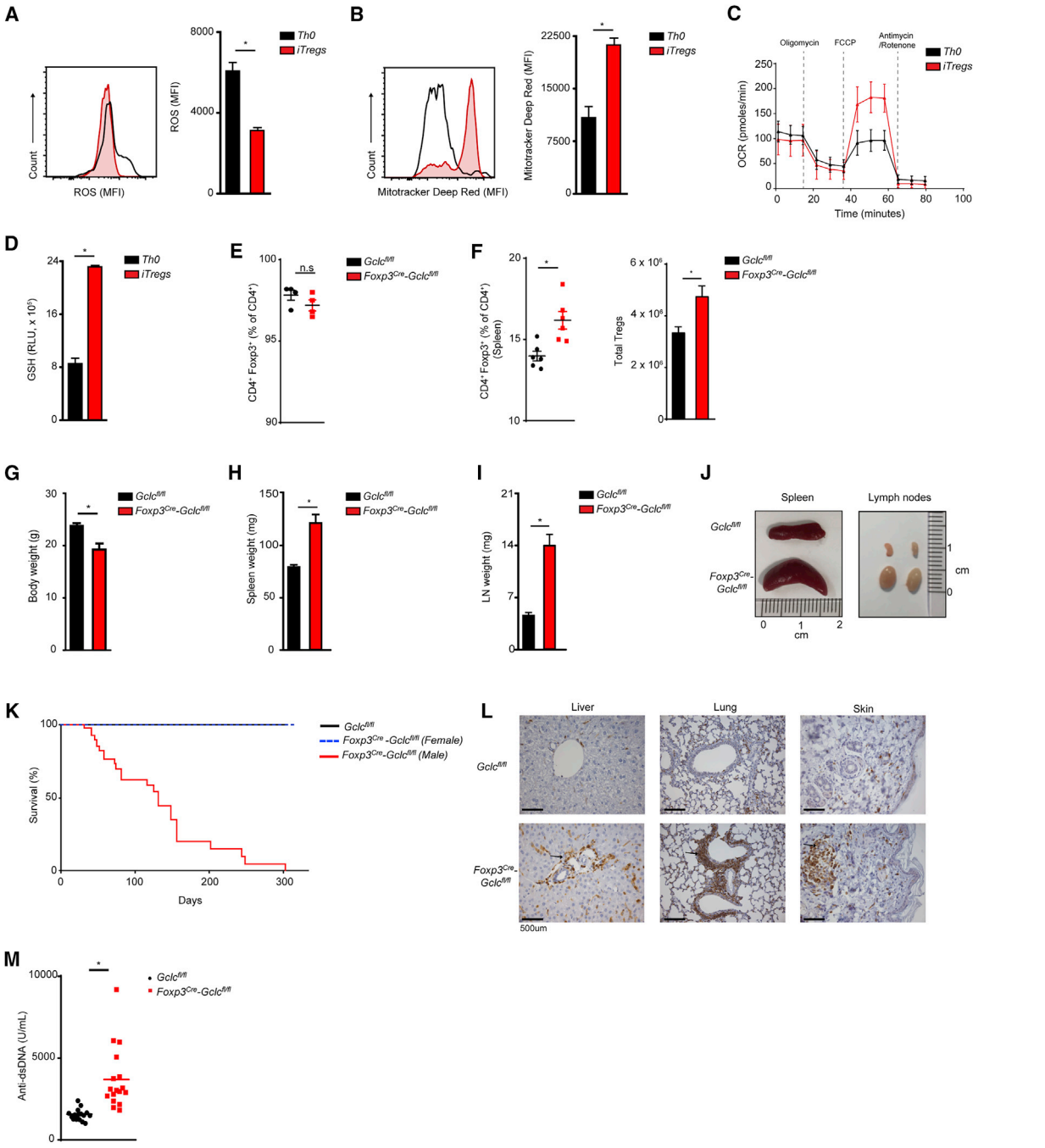

Figure 1. *Gclc* Deficiency Does Not Affect Treg Homeostasis but Does Lead to Multi-organ Inflammation

(A–D) Splenic naive T cells from C57BL/6 mice were treated with αCD3+αCD28+IL2, with or without TGFβ, to generate iTreg or Th0 cells, respectively. Cells were stained with (A) DCF-DA to detect ROS, or (B) Mitotracker Deep Red to assess mitochondrial function, followed by flow cytometry (FC).

(C) Seahorse determination of OCR.

(D) Luminescence-based quantification of intracellular GSH. Data are mean ± SEM (n = 3) and are representative of 3 independent trials.

(E) FC quantitation of $CD4^+Foxp3^+$ iTregs among splenic naive T cells isolated from $Gclc^{fl/fl}$ (control) or $Foxp3^{cre}$-$Gclc^{fl/fl}$ mice and treated *in vitro* with αCD3+αCD28+IL2+TGF-β. Data are mean ± SEM (n = 4); 5 trials.

(F) Flow cytometric analysis (FCA) of $CD4^+Foxp3^+$ nTregs from spleens of $Gclc^{fl/fl}$ and $Foxp3^{cre}$-$Gclc^{fl/fl}$ mice. Data are mean ± SEM (n = 6); 5 trials.

(G–I) Weights of (G) whole body, (H) spleen, and (I) LN from $Gclc^{fl/fl}$ and $Foxp3^{cre}$-$Gclc^{fl/fl}$ mice at 8–12 weeks of age. Data are mean ± SEM (n = 13).

(J) Images of spleens and LN from $Gclc^{fl/fl}$ and $Foxp3^{cre}$-$Gclc^{fl/fl}$ mice (8 weeks of age).

(K) Survival of $Gclc^{fl/fl}$ (n = 48) and $Foxp3^{cre}$-$Gclc^{fl/fl}$ (male n = 38, female = 21) mice.

(legend continued on next page)

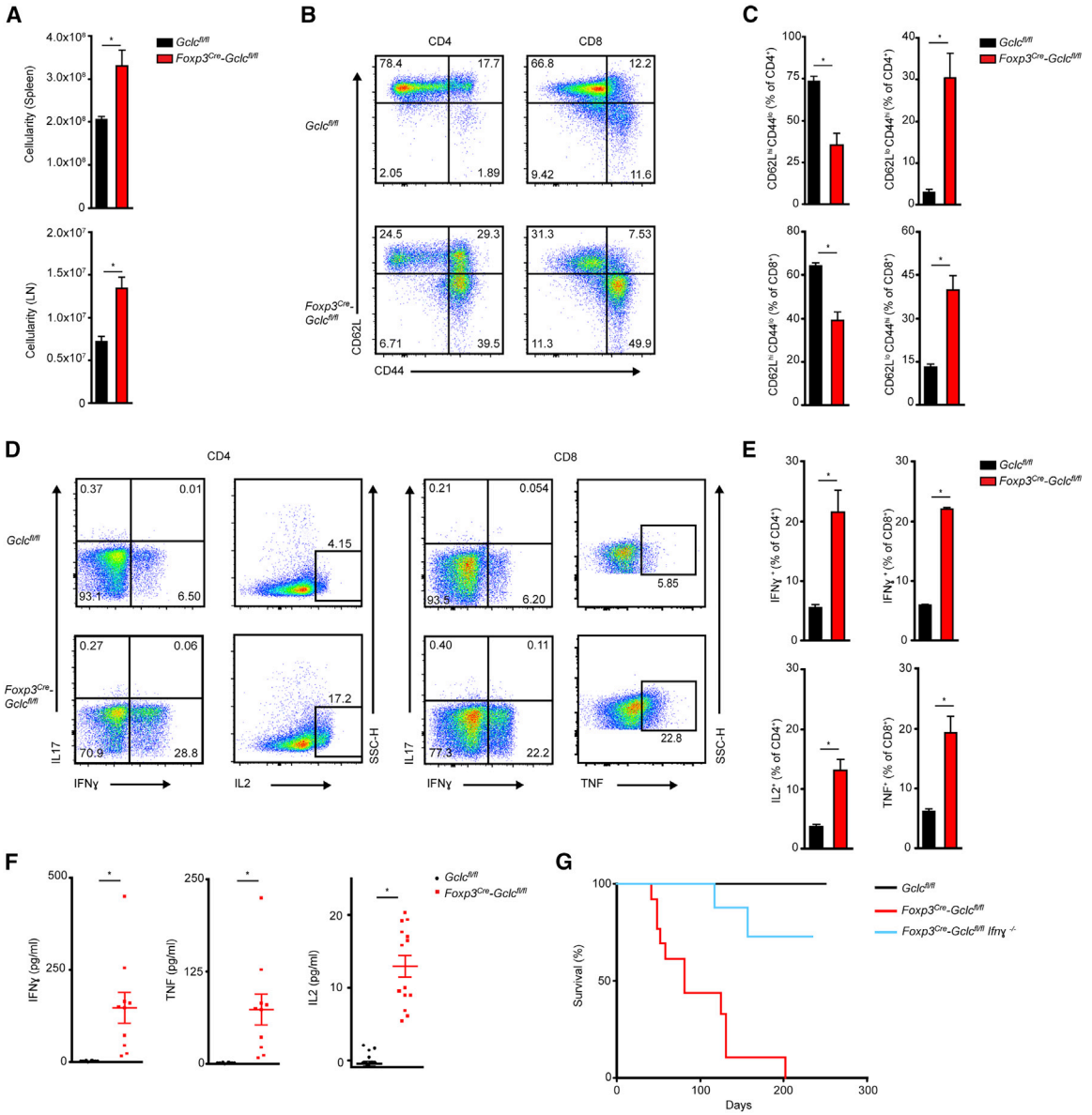

Figure 2. Treg-Specific *Gclc* Deletion Impairs Homeostasis

(A) Total lymphocyte numbers in spleen and LN of *Gclc*$^{fl/fl}$ and *Foxp3*^{cre}-*Gclc*$^{fl/fl}$ mice. Data are mean ± SEM (n = 6); 2 trials.

(B and C) FCA of naive (CD62L^{hi}CD44^{lo}), central memory (CD62L^{hi}CD44^{hi}), and effector (CD62L^{lo}CD44^{hi}) subsets (B), and quantification within the CD4$^+$ population (top) and CD8$^+$ population (bottom) (C), from *Gclc*$^{fl/fl}$ and *Foxp3*^{cre}-*Gclc*$^{fl/fl}$ mice as in (A). Data are mean ± SEM (n = 3); 5 trials.

(D and E) Intracellular staining and FCA of IFNγ, IL17, IL2, and TNF production by purified CD4$^+$ (left) and CD8$^+$ (right) splenic *Gclc*$^{fl/fl}$ and *Foxp3*^{cre}-*Gclc*$^{fl/fl}$ T cells re-stimulated *in vitro* with 50 ng PMA + 750 ng Iono for 6 h. Data are mean ± SEM (n = 3); 3 trials.

(F) ELISA of IFNγ, TNF, and IL2 in serum of *Gclc*$^{fl/fl}$ and *Foxp3*^{cre}-*Gclc*$^{fl/fl}$ mice (8–12 weeks of age). Each symbol represents an individual mouse. Data are mean ± SEM (*Gclc*$^{fl/fl}$ n = 10; *Foxp3*^{cre}-*Gclc*$^{fl/fl}$ n = 17); 2 trials.

(G) Survival of *Gclc*$^{fl/fl}$ (n = 23), *Foxp3*^{cre}-*Gclc*$^{fl/fl}$ (n = 13), and Foxp3^{cre}-*Gclc*$^{fl/fl}$ x *Ifnγ*$^{-/-}$ (n = 14) mice. *p < 0.05.

GSH in Tregs Is Crucial for Their Suppressive Capacity

Flow cytometric analysis of splenic nTregs from *Foxp3*^{cre}-*Gclc*$^{fl/fl}$ and control mice revealed that surface levels of CD25, ICOS, CTLA4, GITR, and OX40 were comparable (Figure 3A). However, CD44 and CD69 were elevated on *Gclc*-deficient nTregs and iTregs (Figure S3A), indicating enhanced activation. PD1 was also higher on mutant nTregs. Although PD1 supports nTregs in normal tissues of WT mice (Francisco et al., 2009), PD1 is

(L) Histology of the indicated tissues resected from one *Gclc*$^{fl/fl}$ and one Foxp3^{cre}-*Gclc*$^{fl/fl}$ mouse and stained with αCD3. Scale bars, 500 μm. Results are representative of 5 mice/group; 2 trials.

(M) ELISA of anti-dsDNA Ab in serum of *Gclc*$^{fl/fl}$ (n = 17) and *Foxp3*^{cre}-*Gclc*$^{fl/fl}$ (n = 17) mice (8–12 weeks of age). *p < 0.05.

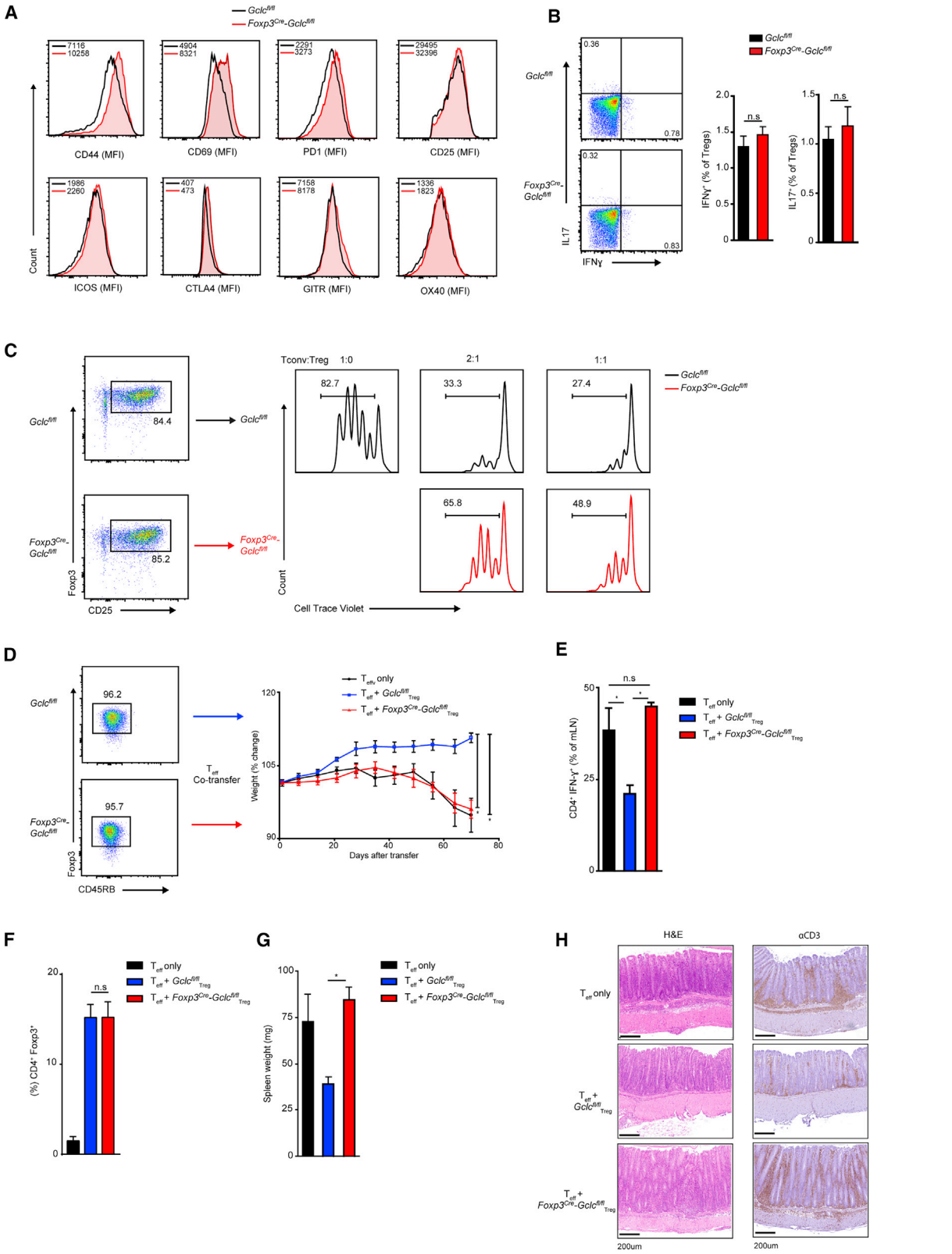

(legend on next page)

linked to Treg dysfunction and increased IFNγ in tumors (Lowther et al., 2016). Notably, *Gclc*-deficient nTregs did not produce more IFNγ after restimulation (Figure 3B), implying that they are stable and do not become Teffs. In line, Helios (Kim et al., 2015; Nakagawa et al., 2016) and IRF4 expression were normal in mutant splenic nTregs (Figure S3B). We next co-cultured control conventional T cells (Tconv) with control or *Foxp3*^{cre}-*Gclc*$^{fl/fl}$ iTregs or freshly isolated nTregs and measured Tconv proliferation. *Gclc*-deficient nTregs and iTregs suffered a dramatic reduction in suppressive capacity independent of the Treg:Tconv ratio (Figures 3C, S3C, and S3D) and expressed less IL10 and TGFβ (Figure S3E).

To explore these data *in vivo*, we employed a T-cell-dependent colitis model (Reardon et al., 2011). WT Teffs (CD4$^+$ CD45RB^{high}) were adoptively transferred alone, or with control or *Gclc*-deficient nTregs (CD4$^+$CD45RB^{low}), into *Rag1*$^{-/-}$ recipient mice. Colitis (represented by mouse weight loss) was induced by control Teffs alone but not if control nTregs were co-transferred (Figure 3D). In contrast, mice receiving control Teffs plus *Gclc*-deficient nTregs developed colitis (Figure 3D). Teffs from mice receiving control Teffs only, or control Teffs plus *Gclc*-deficient nTregs, produced more IFNγ (Figure 3E). Numbers of nTregs in all recipients after 50 days were equal, ruling out colitis due to mutant Treg death (Figure 3F). Recipients of control Teffs plus *Gclc*-deficient nTregs exhibited splenomegaly (Figure 3G), and intestinal crypts of these recipients showed T cell infiltration (Figure 3H). Thus, *Gclc* in Tregs is indispensable for suppression *in vitro* and *in vivo*.

FoxP3 Is Reduced in *Gclc*-Deficient Tregs Due to Increased mTOR Activation

To determine if *Gclc* deficiency alters Treg gene transcription, we used RNA sequencing (RNA-seq) and principal component analysis (PCA) to examine *Foxp3*^{cre}-*Gclc*$^{fl/fl}$ and *Gclc*$^{fl/fl}$ iTreg transcriptomes (Figure S4A). *Foxp3* was the most downregulated gene in mutant iTregs (Figure 4A) and splenic nTregs (Figure S4B). Although FoxP3$^+$ nTreg numbers were slightly increased in *Foxp3*^{cre}-*Gclc*$^{fl/fl}$ mice (Figures 1F), intracellular FoxP3 expression was reduced in mutant nTregs and iTregs (Figure 4B).

Reciprocity exists between mTOR and Foxp3 in Tregs (Delgoffe et al., 2009; Gerriets et al., 2015; Huynh et al., 2015). Phosphorylation (p) of mTOR and its target S6 were increased in nTregs and iTregs from male *Foxp3*^{cre}-*Gclc*$^{fl/fl}$ mice (Figure 4C). To rule out any effects of inflammation, we analyzed nTregs from female mutants heterozygously expressing a *Foxp3*^{cre}-YFP$^+$ reporter gene. Due to random X chromosome inactivation, these disease-free animals contain YFP$^+$ nTregs (activated Cre, *Gclc* absent) and YFP$^-$ nTregs (no Cre, *Gclc* intact). Higher pS6 and pmTOR were detected in YFP$^+$ nTregs than in YFP$^-$ nTregs (Figure S4C). To confirm this result, we generated tamoxifen (TAM)-inducible Treg-specific *Gclc*-deficient mice (*Foxp3*$^{ER\text{-}cre}$-*Gclc*$^{fl/fl}$), which showed no inflammation without TAM. We isolated naive T cells from these mutants and controls and induced iTregs *in vitro*. In parallel, we triggered acute *Gclc* deletion by adding 4-hydroxytamoxifen (4-OHT). Again, we observed increased pS6, decreased FoxP3, and reduced iTreg mediated suppression (Figures S4D and S4E). Conversely, retroviral transduction of *Gclc* into *Gclc*-deficient iTregs reduced pS6, increased FoxP3, and restored their suppressive capacity (Figures 4D and 4E). Thus, *Gclc's* effects on mTOR and FoxP3 are not compromised by an inflammatory environment.

When we treated *Gclc*-deficient iTregs with the mTOR inhibitor rapamycin (Rap) (Dumont and Su, 1996), pS6 was reduced and FoxP3 was restored (Figures 4F and 4G), confirming that increased mTOR in GSH-deficient cells decreases FoxP3. We isolated nTregs from spleen and LN of male *Foxp3*^{cre}-*Gclc*$^{fl/fl}$ and control mice, incubated these cells with or without Rap for 24 h, removed Rap, and measured nTregs' suppressive capacity. Again, Rap normalized *Gclc*-deficient nTreg-mediated suppression (Figure 4H). Smad3 is linked to FoxP3 induction in Tregs (Tone et al., 2008). Smad 3 is suppressed and inactivated by mTOR, and hyperphosphorylated in mTOR-deficient cells (Delgoffe et al., 2009). In consistency, our *Gclc*-deficient iTregs showed increased mTOR activation and reduced pSmad3, which was reversed by Rap (Figure 4I). We next infected control and *Gclc*-deficient iTregs with retrovirus expressing Smad3. FoxP3 increased in Smad3-transduced mutant cells, which regained their suppressive function (Figures 4J and 4K). Retroviral expression of constitutively active STAT5 had no effect (Figure S4F). Thus, mTOR inactivation mediated by GSH is critical for Smad3-dependent FoxP3 induction and iTregs' suppressive capacity.

To explore these findings *in vivo*, we intraperitoneally (i.p.) injected male control and *Foxp3*^{cre}-*Gclc*$^{fl/fl}$ mice (6 weeks) with Rap or vehicle every other day for 30 days. Rap ameliorated inflammatory disease in the mutants due to its immunosuppressive effect (Figures S4G–S4L). Rap also restored *Gclc*-deficient nTreg function such that Teff proliferation was suppressed *in vitro* (Figure S4M). To determine whether FoxP3 reconstitution alone in *Gclc*-deficient Tregs could rescue their suppressive

Figure 3. GSH Modulates Treg Functionality *In Vitro* and *In Vivo*

(A) FCA of the indicated surface markers on splenic nTregs from *Gclc*$^{fl/fl}$ and *Foxp3*^{cre}-*Gclc*$^{fl/fl}$ mice (n = 3); 4 trials.

(B) FC quantification of intracellular IFNγ and IL17 in splenic nTregs of *Gclc*$^{fl/fl}$ and *Foxp3*^{cre}-*Gclc*$^{fl/fl}$ mice re-stimulated *in vitro* with PMA + Iono for 6 h. Data are mean ± SEM (n = 3); 3 trials.

(C) *In vitro* suppression assay of splenic nTregs from *Gclc*$^{fl/fl}$ and *Foxp3*^{cre}-*Gclc*$^{fl/fl}$ mice incubated at the indicated ratios with Tconv labeled with 5 μM cell-trace violet (CTV). Suppression was determined by FC as a decrease in Tconv proliferation; 5 trials.

(D) *In vivo* assay of Treg suppression using a T cell adoptive transfer-based induced colitis model. *Rag1*$^{-/-}$ mice received WT Teff (CD4$^+$CD45RB^{high}) alone or together with FACS-sorted nTregs (CD4$^+$ CD45RB^{low}) from *Gclc*$^{fl/fl}$ or *Foxp3*^{cre}-*Gclc*$^{fl/fl}$ mice. Results are presented as post-transfer body weight relative to initial weight of recipients. Data are mean ± SEM (n = 4); 2 trials.

(E) Intracellular staining and FCA of IFNγ produced by CD4$^+$ Teff isolated from mesenteric LN of the mice in (D) at day 70 post-transfer and re-stimulated *in vitro* with PMA+Iono. Data are mean ± SEM (n = 4); 2 trials.

(F) Quantification of nTregs in peripheral blood of *Rag1*$^{-/-}$ recipients treated as in (D) at 50 days post-transfer. Data are mean ± SEM (n = 2–3). 2 trials.

(G) Quantification of spleen weights of the *Rag1*$^{-/-}$ recipients in (D) at experimental endpoint. Data are mean ± SEM (n = 4); 2 trials.

(H) Histology of large intestine of the mice in (D) after staining with H&E or αCD3. Scale bars, 200 μm. Data are mean ± SEM (n = 4); 2 trials. *p < 0.05.

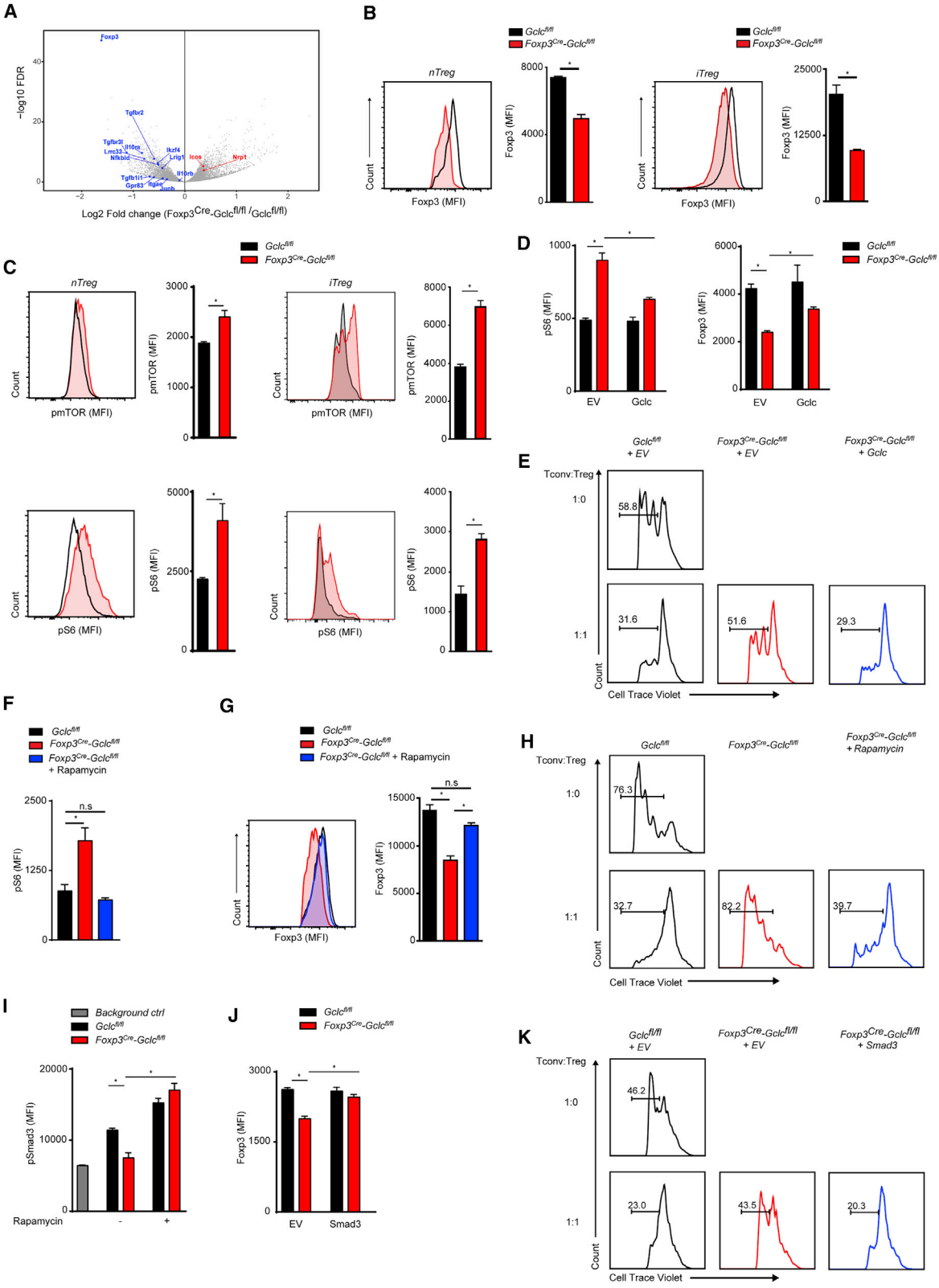

Figure 4. Lack of GSH Alters mTOR Signaling and Impairs FoxP3 Expression

(A) Volcano plot comparing mRNAs of the indicated Treg-associated genes in *Foxp3^{cre}-Gclc$^{fl/fl}$ and Gclc$^{fl/fl}$* iTregs. Downregulated (blue) and upregulated (red) transcripts in *Foxp3^{cre}-Gclc$^{fl/fl}$* are shown.

(legend continued on next page)

capacity, we transduced *Foxp3*^{cre}-*Gclc*$^{fl/fl}$ Tregs with control or *Foxp3*-expressing retrovirus and subjected transduced CD90.1^{+} iTregs to *in vitro* suppression assays. Indeed, retroviral *Foxp3* expression restored FoxP3 and the suppressive activity of *Gclc*-deficient Tregs (Figures S4N and S4O). Thus, GSH is crucial *in vitro* and *in vivo* for maintaining Treg suppression through effects on mTOR and FoxP3.

Regulation of Serine Availability by GSH Is Required for Treg Function

mTOR is an energy sensor that is activated by AA levels (Goberdhan et al., 2016). Gene set enrichment analysis revealed that *Gclc*-deficient iTregs and nTregs showed elevated expression of genes associated with AA metabolism or 1CMet (Figures 5A, 5B, S5A, and S5B). Heightened 1CMet is linked to increased Teff proliferation (Ma et al., 2017; Ron-Harel et al., 2016). In line, *Gclc*-deficient iTregs proliferated more vigorously than controls (Figure 5C), in striking contrast to *Gclc*-deficient Tconv, where GSH loss blocks proliferation (Mak et al., 2017). Thus, GSH has a surprising, subset-specific role in Tregs.

Serine drives 1CMet because it provides its hydroxymethyl group as a one-carbon unit to tetrahydrofolate (Ducker and Rabinowitz, 2017; Herbig et al., 2002; Tibbetts and Appling, 2010). *Gclc*-deficient iTregs showed increased expression of genes involved in serine metabolism (Figure 5D). When we cultured *Gclc*-deficient iTregs or 4-OHT-inducible *Gclc*-deficient iTregs without serine, pS6 was reduced to control levels (Figure 5E), while FoxP3 was increased (Figure 5F). Serine deprivation had only minor effects on pS6 and Foxp3 in control iTregs. Although glycine is also a 1CMet donor, its deprivation neither decreased pS6 nor restored FoxP3 in *Gclc*-deficient iTregs (Figure S5C). To assess when serine suppresses FoxP3 in GSH-deficient Tregs, we cultured *Gclc*-deficient iTregs with or without serine for various times. When mutant iTregs were induced from naive T cells in the absence of serine for 96 h, FoxP3 rose (Figure S5D). However, serine deprivation for only 48 h (followed by serine supplementation for the next 48 h) had no effect, and FoxP3 remained low in mutant iTregs. Conversely, mutant iTregs incubated with serine for the first 48 h followed by serine starvation for 48 h showed increased FoxP3. Thus, serine exerts its effect during later stages of Treg differentiation.

Cells import serine via the alanine-serine-cysteine-threonine transporters (ASCTs) 1 and 2, which are encoded by the *SLC1A4* and *SLC1A5* genes, respectively (Bröer and Bröer, 2017; Kaplan et al., 2018; Yamamoto et al., 2004). *SLC1A4* and *SLC1A5* are expressed by T cells (Ren et al., 2017). *SLC1A4* (but not *SLC1A5*) mRNA was upregulated in *Gclc*-deficient iTregs (Figures 5G and S5E). *SLC1A4* is a target of the master antioxidant transcription factor NRF2 (Christensen, 1990; Fu et al., 2019; Hirotsu et al., 2012; Schäfer et al., 2010), and NRF2 responses are triggered by increased intracellular ROS (Kong and Chandel, 2018). Thus, cells with elevated ROS might increase *SLC1A4*. Both iTregs and nTregs lacking *Gclc* (which have high ROS; Figure S1E) exhibited enriched expression of ROS metabolism genes (Figure S5F) and increased NRF2 target gene activation (Figure S5G). *SLC1A4* mRNA was increased in *Gclc*-deficient iTregs and normalized when treated with the ROS scavenger N-acetyl-cysteine (NAC) (Figure 5G). In line with increased *SLC1A4*, *Gclc*-deficient iTregs consumed more serine and secreted more glycine and formate than did controls (Figure 5H), and antioxidant treatment of these cells decreased intracellular serine (Figure 5I) and restored FoxP3 (Figure S5H).

The ASCT AA transporters are inhibited by L-phenylglycine (Foster et al., 2017). We treated control and *Gclc*-deficient iTregs with L-phenylglycine to block ASCTs and detected reduced intracellular serine in the mutant cells (Figure S5I) as well as decreased formate secretion (Figure 5J). L-phenylglycine restored FoxP3 in *Gclc*-deficient iTregs and 4-OHT-inducible *Gclc*-deficient iTregs (Figure 5K). CRISPR/Cas9-mediated downregulation of ASCT1 increased FoxP3 in mutant iTregs (Figure S5J). ASCT blockade also reinstated *Gclc*-deficient nTregs suppressive function (Figure 5L). Thus, restriction of serine uptake is crucial for maintaining Tregs' suppressive capacity.

Serine hydroxymethyltransferase (SHMT) mediates serine's contribution to 1CMet. Isotopic tracing with [U-$^{13}C_3$]-serine confirmed increased M1-labeling of formate in mutant iTregs (Figure 5M). While formate secretion by *Gclc*-deficient iTregs decreased upon SHMT inhibition (Figure S5K), Foxp3 did not increase (Figure S5L), but proliferation was normalized (Figure S5M). Thus, serine stimulates 1CMet to increase mutant Treg proliferation, but it also acts to decrease Foxp3- and Treg-mediated suppression independently of SHMT and 1CMet.

GSH Restricts Treg Metabolism and Controls Treg Function via Effects on FoxP3

Increased glycolysis is linked to decreased FoxP3 and diminished Treg suppressive capacity (Gerriets et al., 2015; Huynh et al., 2015). Indeed, *Gclc*-deficient iTregs consumed more

(B) FCA of FoxP3 in *Foxp3*^{cre}-*Gclc*$^{fl/fl}$ *and Gclc*$^{fl/fl}$ Tregs isolated from spleen (left) or induced *in vitro* (right). Data are mean ± SEM (n = 3); 5 trials.
(C) Intracellular staining and FCA of pmTOR and pS6 in *Gclc*$^{fl/fl}$ and Foxp3^{cre}-*Gclc*$^{fl/fl}$ Tregs as in (B). Data are mean ± SEM (n = 3); 5 trials.
(D) Intracellular staining and FCA of pS6 and Foxp3 in *Gclc*$^{fl/fl}$ and *Foxp3*^{cre}-*Gclc*$^{fl/fl}$ iTregs transduced with retrovirus expressing EV or *Gclc*. Data are mean ± SEM (n = 3); 3 trials.
(E) *In vitro* suppression assay of *Gclc*$^{fl/fl}$ and Foxp3^{cre}-*Gclc*$^{fl/fl}$ iTregs transduced with retrovirus expressing EV or *Gclc*. Transduced Tregs were FACS sorted and incubated with CTV-labeled Tconv at the indicated ratios; 2 trials.
(F) FCA of pS6 in *Foxp3*^{cre}-*Gclc*$^{fl/fl}$ and *Gclc*$^{fl/fl}$ iTregs incubated with/without Rap. Data are mean ± SEM (n = 3); 3 trials.
(G) Intracellular staining and FCA of FoxP3 in *Foxp3*^{cre}-*Gclc*$^{fl/fl}$ *and Gclc*$^{fl/fl}$ iTregs incubated with/without 100 nM Rap. Data are mean ± SEM (n = 3); 3 trials.
(H) *In vitro* suppression assay of splenic nTregs from *Gclc*$^{fl/fl}$ and Foxp3^{cre}-*Gclc*$^{fl/fl}$ mice that were incubated with/without Rap for 24 h and mixed with Tconv at the indicated ratios; 5 trials.
(I) Intracellular staining and FCA of pSmad3 in *Foxp3*^{cre}-*Gclc*$^{fl/fl}$ *and Gclc*$^{fl/fl}$ iTregs incubated with/without Rap. Data are mean ± SEM (n = 3); 2 trials.
(J) Intracellular staining and FCA of Foxp3 in *Gclc*$^{fl/fl}$ and *Foxp3*^{cre}-*Gclc*$^{fl/fl}$ iTregs transduced with retrovirus expressing EV or Smad3. Data are mean ± SEM (n = 3); 3 trials.
(K) *In vitro* suppression assay of *Gclc*$^{fl/fl}$ and Foxp3^{cre}-*Gclc*$^{fl/fl}$ iTregs transduced with retrovirus expressing EV or Smad3. Transduced Tregs were FACS sorted and incubated with CTV-labeled Tconv at the indicated ratios; 2 trials. *p < 0.05.

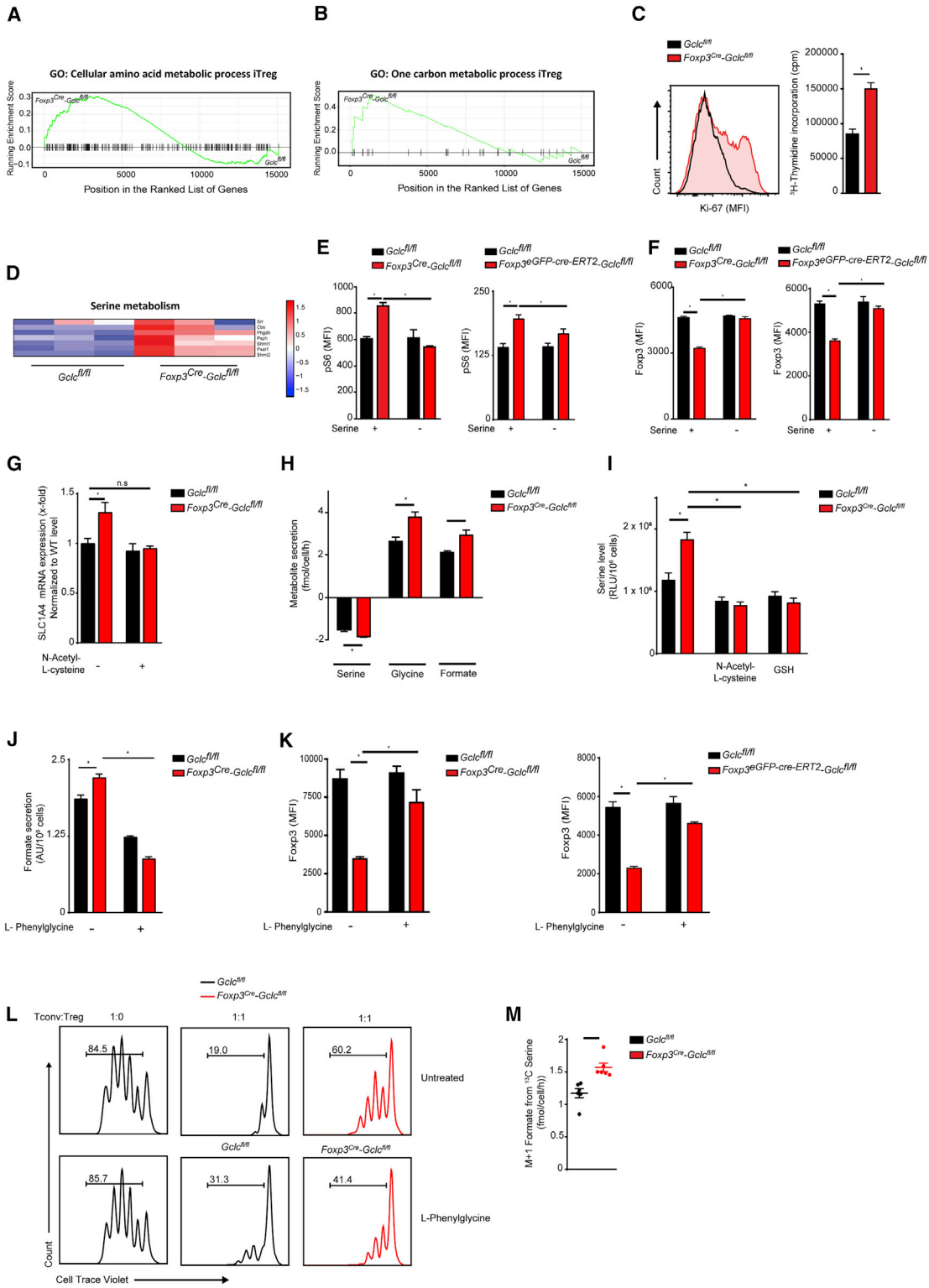

Figure 5. GSH-Mediated Regulation of the Serine Pool Is Required for Treg Function

(A) Barcode enrichment plot of KEGG pathway GO:0006520 (Cellular amino acid metabolic processes) for *Gclc*$^{fl/fl}$ and Foxp3^{cre}-*Gclc*$^{fl/fl}$ iTregs.

(B) Barcode enrichment plot of KEGG pathway GO:0006730 (1CMet) for *Gclc*$^{fl/fl}$ and Foxp3^{cre}-*Gclc*$^{fl/fl}$ iTregs.

(C) Determination of proliferation of *Gclc*$^{fl/fl}$ and Foxp3^{cre}-*Gclc*$^{fl/fl}$ iTregs by Ki-67 staining (left) and ^{3}H-thymidine incorporation (right). Data are mean ± SEM (n = 3); 3 trials.

(legend continued on next page)

glucose, secreted more lactate, and expressed more of the glucose transporter Glut1 than did controls (Figures 6A and S6A). Glycolysis stress testing of *Gclc*-deficient iTregs and 4-OHT-inducible *Gclc*-deficient iTregs revealed that the extracellular acidification rate (ECAR) of culture medium and cellular glycolytic capacity were increased whether *Gclc* ablation was constitutive or 4-OHT induced (Figures 6B and 6C). We then determined [U-$^{13}C_6$]-glucose incorporation into TCA cycle metabolites in *Gclc*-deficient and control iTregs over 24 h and measured mass isotopomer distributions (MIDs) by GC-MS. M2 isotopologues of citrate were elevated in mutant iTregs (Figure S6B), demonstrating an increased relative flux of glucose-derived carbon into the TCA cycle. Accordingly, OCR values in *Gclc*-deficient iTregs and 4-OHT-inducible *Gclc*-deficient iTregs were increased (Figures 6D and 6E).

To determine if enhanced metabolism interfered with iTreg mediated suppression, we incubated *Gclc*-deficient and control iTregs with 2-deoxyglucose (2-DG) or oligomycin to restrict glycolysis or oxidative phosphorylation (OXPHOS), respectively. Restriction of either pathway induced control levels of FoxP3 in the mutant cells and restored their suppressive function (Figures 6F and 6G). To investigate a direct link between FoxP3 and increased metabolism, we transduced *Gclc*-deficient and control iTregs with retrovirus expressing FoxP3 or empty vector (EV). In mutant iTregs, FoxP3 expression decreased uptake of the glucose analog 2-NDBG as well as Glut1 expression and glycolysis (ECAR) (Figures 6H–6J). *Gclc* deficiency in Tconv is associated with impaired mTOR activation and decreased MYC (Mak et al., 2017), but mTOR was more activated (Figure 4C) and MYC was normal in *Gclc*-deficient iTregs (Figure S6C), again pointing to a subset-specific function for GSH. To determine whether FoxP3 could alter a T cell's response to GSH depletion, we transduced activated WT Tconv with retrovirus expressing FoxP3 or EV and treated these cells with the GCLC inhibitor buthionine sulfoximine (BSO). In line with previous work (Gerriets et al., 2016), FoxP3 expression in activated Tconv reduced pS6 (Figures 6K and S6D). BSO decreased pS6 in activated Tconv expressing EV (Figure 6K), but FoxP3 expression altered the Tconv response to BSO and increased pS6 (Figure 6K). Thus, it is FoxP3 in Tregs that shapes responses to GSH depletion; that is, the decreased mTOR activation in activated Tconv lacking GSH shifts to activation of this pathway in *Gclc*-deficient Tregs.

De Novo Serine Synthesis in Tregs Interferes with Foxp3 Expression

During glycolysis, 3-phosphoglycerate dehydrogenase (PHGDH) redirects some 3-PG to serine synthesis. To determine if *Gclc*-deficient Tregs increased glycolysis to produce the 3-PG needed for their enhanced serine production, we incubated *Gclc*-deficient and control iTregs for 24 h with the PHGDH inhibitor PKUMDL-WQ-2101 (Wang et al., 2017) and found equivalent decreases in ECAR (Figure 7A). Thus, regardless of GSH, glycolysis in Tregs is driven partly by the need for intermediates for serine synthesis. [U-$^{13}C_6$]-glucose incorporation into serine and formate was enhanced in *Gclc*-deficient iTregs and reduced by PHGDH inhibition (Figures 7B and 7C). PHGDH inhibition or CRISPR/CAS9 mediated *Phgdh* deletion also elevated FoxP3 in *Gclc*-deficient iTregs and 4-OHT-inducible *Gclc*-deficient iTregs (Figures 7D and 7E). Consequently, PHGDH inhibition restored mutant iTregs suppressive capacity (Figure 7F). Thus, limitation of serine availability by GSH preserves FoxP3 expression and Treg function.

GSH regulates serine uptake and synthesis. Serine deprivation of control iTregs increased glucose-dependent GSH synthesis (Figure S7A), supporting interconnection of these pathways in a feedback loop. To investigate serine's relevance *in vivo*, we fed serine- and glycine-deficient food to 3-week-old control and mutant mice. Serine/glycine-deficient food is well tolerated, measurably decreases circulating serine/glycine, and does not interfere with immune cell subsets (Ma et al., 2017; Maddocks et al., 2013; Maddocks et al., 2017). Serine deprivation *in vivo* increased FoxP3 but reduced pS6 and CD44 in mutant nTregs (Figure 7G), and it decreased serum IFNγ and TNF as well as inflammatory T cells in mutant mice (Figures 7H and 7I). Strikingly, serine/glycine deprivation prevented mutant mouse spontaneous inflammation and death (Figure 7J), confirming the importance of serine metabolism and 1CMet *in vivo*.

To replicate our data in human Tregs, we isolated naive T cells from peripheral blood of healthy donors and induced iTreg differentiation *in vitro* with TGFβ in the absence or presence of BSO. GSH was reduced in BSO-treated human iTregs (Figure S7B). FoxP3 was also decreased, but pS6 was increased (Figures S7C and S7D). Serine deprivation of BSO-treated human iTregs restored FoxP3 and pS6 to control levels (Figures S7E and S7F). FoxP3 in BSO-treated human iTregs was also increased by

(D) Heatmap showing normalized differential gene expression patterns of genes associated with serine metabolism in *Gclc*$^{fl/fl}$ versus *Foxp3*^{cre}-*Gclc*$^{fl/fl}$ iTregs.
(E and F) Intracellular staining and FCA of (E) pS6 and (F) Foxp3 in *Gclc*$^{fl/fl}$ versus Foxp3^{cre}-*Gclc*$^{fl/fl}$ (left) and *Gclc*$^{fl/fl}$ versus Foxp3$^{eGPF\text{-}cre\text{-}ERT2}$-*Gclc*$^{fl/fl}$ (right) iTregs cultured in normal or serine-deficient medium. *Gclc*$^{fl/fl}$ versus Foxp3$^{eGPF\text{-}cre\text{-}ERT2}$-*Gclc*$^{fl/fl}$ iTregs were co-incubated with 1μM 4-OHT. Data are mean ± SEM (n = 3); 3 trials.
(G) RT-qPCR of *ASCT1* mRNA in *Gclc*$^{fl/fl}$ and Foxp3^{cre}-*Gclc*$^{fl/fl}$ iTregs. Data are mean ± SEM (n = 7); 2 trials.
(H) LC/MS quantification of serine uptake from, and glycine and formate secretion into, culture medium of *Gclc*$^{fl/fl}$ and Foxp3^{cre}-*Gclc*$^{fl/fl}$ iTregs. Data are mean ± SEM (n = 3); 2 trials.
(I) Quantification of intracellular serine in *Gclc*$^{fl/fl}$ and Foxp3^{cre}-*Gclc*$^{fl/fl}$ iTregs treated with/without 200 μM NAC or 0.5 mM GSH. Data are mean ± SEM (n = 3); 2 trials.
(J) Quantification of formate secretion into culture medium of *Gclc*$^{fl/fl}$ and Foxp3^{cre}-*Gclc*$^{fl/fl}$ iTregs treated with/without 50 μM L-phenylglycine. Data are mean ± SEM (n = 3); 2 trials.
(K) Intracellular staining and FCA of Foxp3 in *Gclc*$^{fl/fl}$ versus Foxp3^{cre}-*Gclc*$^{fl/fl}$ (left), and *Gclc*$^{fl/fl}$ versus Foxp3$^{eGPF\text{-}cre\text{-}ERT2}$-*Gclc*$^{fl/fl}$ (right), iTregs treated with/without L-phenylglycine. *Gclc*$^{fl/fl}$ versus Foxp3$^{eGPF\text{-}cre\text{-}ERT2}$-*Gclc*$^{fl/fl}$ iTregs were co-incubated with 4-OHT. Data are mean ± SEM (n = 3); 3 trials.
(L) *In vitro* suppression assay of nTregs that were isolated from *Gclc*$^{fl/fl}$ and Foxp3^{cre}-*Gclc*$^{fl/fl}$ mice, incubated with/without L-phenylglycine, and mixed *in vitro* with Tconv at the indicated ratios; 3 trials.
(M) Mass isotopomer distribution of M+1 formate following incubation of *Gclc*$^{fl/fl}$ and Foxp3^{cre}-*Gclc*$^{fl/fl}$ iTregs with [U-$^{13}C_3$]-serine for 24 h. Data are mean ± SEM (n = 3); 2 trials. *p < 0.05.

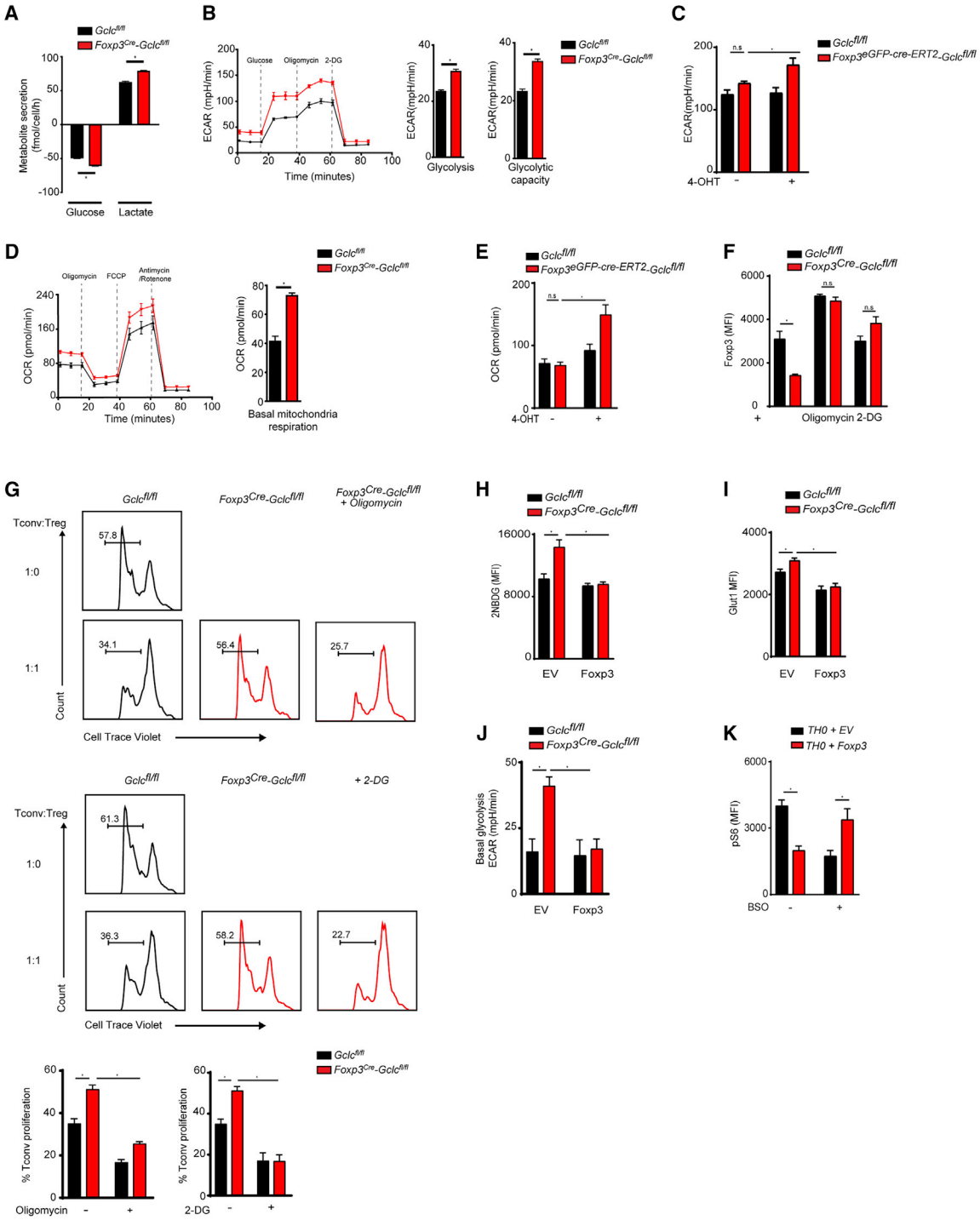

Figure 6. *Gclc* Expression Is Required to Modulate Treg Metabolism Supporting Treg Function

(A) Quantification of glucose uptake from and lactate secretion into culture medium of *Gclc*$^{fl/fl}$ and *Foxp3*^{cre}-*Gclc*$^{fl/fl}$ iTregs. Data are mean ± SEM (n = 3); 3 trials.

(B) Quantification of ECAR of *Gclc*$^{fl/fl}$ versus *Foxp3*^{cre}-*Gclc*$^{fl/fl}$ iTregs. Data are mean ± SEM (n = 4); 4 trials.

(C) Quantification of ECAR of *Gclc*$^{fl/fl}$ versus *Foxp3*$^{eGPF\text{-}cre\text{-}ERT2}$-*Gclc*$^{fl/fl}$ iTregs incubated with 4-OHT. Data are mean ± SEM (n = 3); 2 trials.

(D) Quantification of OCR of *Gclc*$^{fl/fl}$ versus *Foxp3*^{cre}-*Gclc*$^{fl/fl}$ iTregs. Data are mean ± SEM (n = 4); 4 trials.

(E) Quantification of OCR of *Gclc*$^{fl/fl}$ versus *Foxp3*$^{eGPF\text{-}cre\text{-}ERT2}$-*Gclc*$^{fl/fl}$ iTregs incubated with 4-OHT. Data are mean ± SEM (n = 3); 2 trials.

(F) Intracellular staining and FCA of FoxP3 in *Gclc*$^{fl/fl}$ versus *Foxp3*^{cre}-*Gclc*$^{fl/fl}$ iTregs treated with or without suboptimal doses of 0.5 nM oligomycin or 100 μM 2-DG for 24 h. Data are mean ± SEM (n = 3); 3 trials.

(G) *In vitro* suppression assay of *Gclc*$^{fl/fl}$ versus *Foxp3*^{cre}-*Gclc*$^{fl/fl}$ iTregs treated (or not) with suboptimal doses of oligomycin (top) or 2-DG (bottom) prior to incubation with CTV-labeled Tconv at the indicated ratios; 3 trials.

(legend continued on next page)

blocking serine synthesis or restricting serine influx (Figure S7G). Lastly, BSO-treated human iTregs showed a profound loss of suppression (Figure S7H). All these data parallel the results obtained using our mouse model of Treg-specific *Gclc* deficiency.

Anti-tumor Immunity Is Enhanced in *Foxp3*^{cre}-*Gclc*$^{fl/fl}$ Mice

Tregs can promote tumor growth by inhibiting Teff-mediated anti-tumor responses, and some tumors secrete substances driving Treg differentiation (Franchina et al., 2018b). Tumors often generate high ROS due to hypoxia or activities of cancer-associated macrophages or fibroblasts (Bhattacharyya and Saha, 2015; Henze and Mazzone, 2016; Sabharwal and Schumacker, 2014). These ROS inactivate Teffs and so dampen anti-tumor immunity (Bhattacharyya and Saha, 2015; Franchina et al., 2018b; Mak et al., 2017; Pilipow et al., 2018). GSH synthesis by T cells is thus a major defense against tumor-associated ROS. Our iTregs contained more intracellular GSH than Teffs (Figure 1D), in line with their greater ROS resistance (Huynh et al., 2015). This enhanced ROS resistance may allow Tregs to survive in the tumor microenvironment long enough to suppress anti-tumor responses by Teffs. Conversely, a loss of GSH that compromises Tregs' suppressive capacity might allow Teff anti-tumor responses to proceed unchecked to limit cancer growth. To test this hypothesis, we examined anti-tumor immunity in *Foxp3*^{cre}-*Gclc*$^{fl/fl}$ mice.

We subcutaneously (s.c.) injected *Foxp3*^{cre}-*Gclc*$^{fl/fl}$ and control mice with B16 melanoma cells or MC38 colon adenocarcinoma cells and monitored cancer progression. In both cases, tumor growth was slower in *Foxp3*^{cre}-*Gclc*$^{fl/fl}$ mice (Figures 7K and S7I), and tumor weight and size were reduced (Figures 7L, 7M, and S7J). Tumor-infiltrating lymphocytes (TILs) were increased in tumors of mutant mice (Figure 7N). Absolute numbers and frequencies of CD4$^+$ TILs were comparable, but absolute numbers and frequencies of CD8$^+$PD1$^+$GranzymeB$^+$ Teffs and CD8$^+$IFNγ^+ Teffs were increased in tumors of mutant mice (Figures 7O and S7K). Treg frequency was decreased in tumors of mutant mice, and these Tregs showed reduced FoxP3 (Figure 7O). Adoptive transfer of control or *Gclc*-deficient nTregs into FoxP3-Cre-*Gclc*$^{fl/fl}$ mice on the day prior to B16 melanoma cell inoculation resulted in significant tumor development in mutant mice receiving control nTregs, whereas mutant mice receiving *Gclc*-deficient nTregs had still a greatly decreased tumor burden (Figure 7p). Thus, loss of *Gclc* in Tregs reduces their ability to impair anti-cancer Teff responses and thus boosts anti-tumor immunity.

DISCUSSION

ROS are both detrimental byproducts of metabolism and important signaling molecules during cellular activation and differentiation (Franchina et al., 2018a; Sena and Chandel, 2012). In Tconv, mitochondrial ROS are linked to activation, proliferation, and effector functions (Devadas et al., 2002; Gülow et al., 2005; Jackson et al., 2004; Sena et al., 2013; Yi et al., 2006). Nevertheless, excessive ROS accumulation in these cells must be prevented by antioxidants like GSH. Accordingly, *Gclc* ablation in all T cells abrogates autoimmunity but also interferes with anti-viral responses (Lian et al., 2018; Mak et al., 2017). Prior to our study, GSH's function in Tregs was unknown. Targeting *Gclc* specifically in this subset has revealed an unexpected mechanism by which GSH-mediated ROS scavenging preserves mouse and human Treg functionality through restriction of serine metabolism.

Male *Foxp3*^{cre}-*Gclc*$^{fl/fl}$ mice developed an IFNγ-driven lethal lymphoproliferative disease but were better able to suppress tumorigenesis. We have shown, *in vitro* and *in vivo*, that these effects are due to *Gclc*'s crucial role in Treg suppressive function. A lack of GSH in Tregs reduced their FoxP3 and thus their suppressive capacity, a property restored by FoxP3 reconstitution. Surprisingly, Treg proliferation was increased in the absence of GSH, rather than decreased as in Tconv with genetic deletion of *Gclc* or subjected to pharmacological GCL inhibition (Hamilos et al., 1989; Mak et al., 2017; Suthanthiran et al., 1990). Thus, GSH has a unique function in Tregs.

Serine uptake and *de novo* synthesis were both increased in *Gclc*-deficient Tregs. Serine is utilized by Teffs and cancer cells to support proliferation (Labuschagne et al., 2014; Locasale et al., 2011; Ma et al., 2017; Maddocks et al., 2017; Possemato et al., 2011; Ron-Harel et al., 2016) and tumor invasion (Meiser et al., 2018), but we showed that serine interferes with Treg-mediated suppression. Blocking serine uptake or *de novo* synthesis restored FoxP3 and the suppressive capacity of mutants Tregs. Serine is a major substrate of 1CMet (Ducker and Rabinowitz, 2017), and we showed that formate production is increased in mutant Tregs in a manner driven by serine. Glycine starvation did not rescue FoxP3 in mutant Tregs, indicating a critical role for SHMT but not glycine cleavage. Previous studies have shown that glycine and serine are not always interchangeable (Labuschagne et al., 2014; Ma et al., 2017; Maddocks et al., 2017). However, while blocking SHMT in *Gclc*-deficient Tregs restored normal formate secretion and cell proliferation, it did not increase Foxp3. Thus, serine engages at least two distinct pathways in *Gclc*-deficient Tregs.

In vivo, inflammation and morbidity were drastically reduced in mutant mice fed on a serine/glycine-deficient diet. Serine and glycine are two NEAAs whose deprivation is well tolerated *in vivo* (Maddocks et al., 2013; Maddocks et al., 2017). Because an absence of dietary serine/glycine interferes with CD8$^+$ T cell responses (Ma et al., 2017), the reduction of T cell activation in *Gclc*-deficient mice is likely due at least in part to a direct effect of serine/glycine deprivation on Teff responses. However, the complete absence of inflammation in serine/glycine-starved mutant mice points to a more profound effect. While we cannot rule out that other immune cell subsets are affected, *Gclc*-deficient Tregs of serine/glycine-deprived animals showed restored FoxP3, reduced mTOR signaling, and dampened cellular activation, validating our *in vitro* findings *in vivo*. Importantly,

(H and I) FCA of (H) 2-NBDG uptake and (I) Glut-1 expression by *Gclc*$^{fl/fl}$ versus *Foxp3*^{cre}-*Gclc*$^{fl/fl}$ iTregs transduced with retrovirus expressing EV or Foxp3.
(J) Quantification of ECAR for the iTregs in (H) as determined in (B). For (H–J), data are the mean ± SEM (n = 3); 2 trials.
(K) Intracellular staining and FCA of pS6 in activated WT Tconv transduced with retrovirus expressing EV or FoxP3 as in (H) and treated with BSO for 48 h. Data are mean ± SEM (n = 3); 3 trials. *p < 0.05.

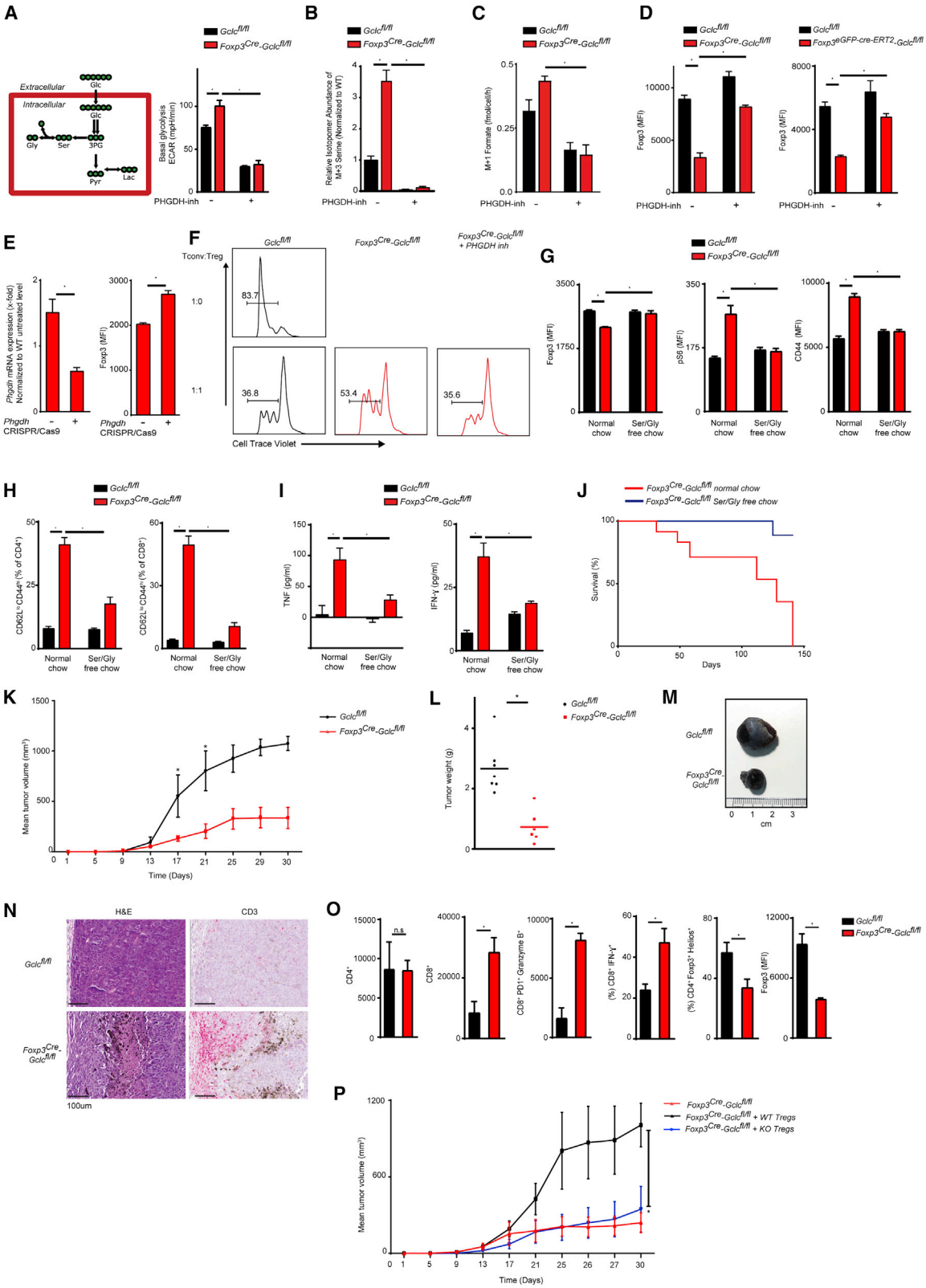

Figure 7. Glutathione Restricts *De Novo* Serine Synthesis and Enhances Anti-tumor Immune Responses

(A) Diagram of serine synthesis pathway (left) and quantification of ECAR of *Gclc*$^{fl/fl}$ and *Foxp3*^{cre}-*Gclc*$^{fl/fl}$ iTregs cultured with/without 10 μM PHGDH inhibitor (right). Data are mean ± SEM (n = 3); 2 trials.

(legend continued on next page)

our study shows that elucidating the exact metabolic and molecular basis of a disease allows potential correction of the metabolic abnormality via a special diet that is aligned with the delineated disease mechanism. Our study might thus be a first step toward personalized treatment of metabolic diseases.

mTOR activation relies mainly on glutamine and leucine (Hara et al., 1998; Nicklin et al., 2009). However, we found that the enhanced serine uptake in mutant Tregs elevated their mTOR activity, paralleling a previous study (Ye et al., 2012). mTOR drives the expression of methylenetetrahydrofolate dehydrogenase (MTHFD)-2 to stimulate 1CMet and purine synthesis (Ben-Sahra et al., 2016), suggesting a feed-forward loop. Such a mechanism might explain how the increased serine levels and mTOR activity in *Gclc*-deficient Tregs support 1CMet. That these pathways are interlinked is indicated by our finding that preventing serine accumulation and inhibiting increased mTOR in mutant Tregs restored their FoxP3 and suppressive function. We therefore propose that in normal Tregs, GSH limits serine uptake and *de novo* synthesis to keep mTOR in check and that this control is critical for Treg function (Figure S7L).

To avoid any effects of inflammation, we assessed FACS-sorted nTregs from non-inflamed female *Foxp3*^{cre}-*Gclc*$^{fl/fl}$ mice, iTregs in which *Gclc* deletion was 4-OHT induced, mutant iTregs subjected to retroviral *Gclc* reconstitution, and human iTregs subjected to pharmacological GCLC blockade. All of these experiments confirmed our findings in male *Foxp3*^{cre}-*Gclc*$^{fl/fl}$ mice. Furthermore, our hypothesis that GSH limits serine and blocks mTOR matches a report that proliferating WT Tregs exhibit stronger mTOR signaling and glycolysis but reduced suppressive capacity (Gerriets et al., 2016). Similarly, constitutive mTOR activation due to deletion of PTEN, PP2A, or TSC1 increases Treg numbers but impairs Treg-mediated suppression (Apostolidis et al., 2016; Huynh et al., 2015; Park et al., 2013; Shrestha et al., 2015). Again, all of these observations align with our findings that *Gclc*-deficient Tregs exhibit increased metabolic activity but are less functional, and that restriction of Treg metabolism reinstates a normal suppressive capacity.

Foxp3 expression in *Gclc*-deficient Tregs was increased by mTOR inhibition or Smad3 overexpression, in line with previous studies showing that mTOR blockade or genetic ablation favors Smad3-dependent induction of FoxP3$^+$ T cells over other Th subsets (Delgoffe et al., 2009; Delgoffe et al., 2011). While *Gclc* ablation in Tconv reduced mTOR activation (Mak et al., 2017), the same mutation has the opposite effect in Tregs, implying a subset-specific function of GSH. Treg identity is largely determined by FoxP3 (Rudensky, 2011), and FoxP3 expression in non-Treg T cells induces certain Treg properties (Fontenot et al., 2003; Hori et al., 2003; Khattri et al., 2003). We found that FoxP3 expression in activated T cells shifted responses to BSO from mTOR inhibition to mTOR activation. Thus, FoxP3 expression combined with pharmacological GCLC inhibition recapitulated results obtained using *Gclc*-deficient mice. It appears that lineage-specific transcription factors shape metabolic responses in a subset-specific way.

We demonstrated that *Gclc* ablation increases ROS in Tregs. Mitochondrial ROS are decreased in Tconv with genetic deletion of mitochondrial complex III (Sena et al., 2013). Loss of complex III in Tregs abrogates their suppressive activity but does so independently of FoxP3 (Weinberg et al., 2019). Although ROS levels were not determined in the latter study, it seems that too much or too little ROS is detrimental to Treg function and that multiple regulatory mechanisms can be engaged. Increased ROS triggers an NRF2 response (Kong and Chandel, 2018), as we observed in *Gclc*-deficient Tregs. A key NRF2 target is ASCT1 (Christensen, 1990; Fu et al., 2019; Hirotsu et al., 2012; Schäfer et al., 2010), which is upregulated when T cells grow in an oxidative environment (Yang et al., 2018). We showed that *SLC1A4* mRNA was upregulated in *Gclc*-deficient Tregs and that ROS scavenging decreased ASCT1 and serine uptake in these cells. In contrast, ASCT2 is not an NRF2 target and was equally expressed in control and *Gclc*-deficient Tregs. Inhibition of serine transport in mutant Tregs, or serine deprivation, increased FoxP3 and normalized their suppressive function. Thus, in Tregs, GSH controls ROS to limit NRF2 activation, which decreases ASCT1 and reduces serine import, thereby permitting full

(B) Mass isotopomer distribution of M+3 serine in the cells in (A) following incubation with [U-$^{13}C_6$]-glucose for 24 h.
(C) Mass isotopomer distribution of M+1 formate in the cells in (A) following incubation with [U-$^{13}C_6$]-glucose for 24 h.
(D) Intracellular staining and FCA of FoxP3 in *Gclc*$^{fl/fl}$ versus *Foxp3*^{cre}-*Gclc*$^{fl/fl}$ (left) and *Gclc*$^{fl/fl}$ versus *Foxp3*$^{eGPF\text{-}cre\text{-}ERT2}$-*Gclc*$^{fl/fl}$ (right) iTregs treated with/without PHGDH inhibitor. *Gclc*$^{fl/fl}$ versus *Foxp3*$^{eGPF\text{-}cre\text{-}ERT2}$-*Gclc*$^{fl/fl}$ iTregs were co-incubated with 4-OHT. Data are mean ± SEM (n = 3); 3 trials.
(E) *Phgdh* mRNA expression (left) and intracellular staining and FCA of FoxP3 (right) in *Gclc*$^{fl/fl}$ versus *Foxp3*^{cre}-*Gclc*$^{fl/fl}$ iTregs that were nucleofected with sgRNAs specific for *Phgdh* or controls. Data are mean ± SEM (n = 3); 2 trials.
(F) *In vitro* suppression assay of *Gclc*$^{fl/fl}$ versus *Foxp3*^{cre}-*Gclc*$^{fl/fl}$ iTregs treated with PHGDH inhibitor prior to incubation with CTV-labeled Tconv at the indicated ratios; 3 trials.
(G) Intracellular staining and FCA of FoxP3, pS6, and CD44 in splenic Tregs of *Gclc*$^{fl/fl}$ versus *Foxp3*^{cre}-*Gclc*$^{fl/fl}$ mice (12 weeks of age) fed with normal chow or a serine- and glycine- (Ser/Gly) free chow for 9 weeks. Data are mean ± SEM (n = 4–11); 2 trials.
(H) FCA and quantification of Teff (CD44^{hi}CD62L^{lo}) within CD4$^+$ (left) and CD8$^+$ (right) T cell populations in blood of the mice in (G). Data are mean ± SEM (n = 4–11); 2 trials.
(I) ELISA of IFNγ and TNF in serum of the mice in (G). Data are mean ± SEM (n = 4–11); 2 trials.
(J) Survival of *Foxp3*^{cre}-*Gclc*$^{fl/fl}$ mice on normal chow (n = 12) or a Ser/Gly- free chow (n = 9);
(K–N) *Gclc*$^{fl/fl}$ and *Foxp3*^{cre}-*Gclc*$^{fl/fl}$ mice (8 weeks of age) were transplanted s.c. with B16F10 melanoma cells.
(K) Mean tumor volumes determined at the indicated times.
(L) Quantification of tumor weights at time of sacrifice. Each dot represents an individual mouse.
(M) Representative macroscopic images of tumors from transplanted *Gclc*$^{fl/fl}$ and *Foxp3*^{cre}-*Gclc*$^{fl/fl}$ mice.
(N) Histology of tumor sections from the mice in (F) stained with H&E or αCD3. Scale bars, 100 μm. Results are representative of 4 mice/group; 2 trials.
(O) Quantification of the indicated TIL subsets in tumors of *Gclc*$^{fl/fl}$ and *Foxp3*^{cre}-*Gclc*$^{fl/fl}$ mice treated as in (K). Data are mean ± SEM (n = 5).
(P) Mean tumor volumes at the indicated times in *Foxp3*^{cre}-*Gclc*$^{fl/fl}$ mice (8 weeks of age) transplanted s.c. with B16F10 melanoma cells and injected intravenously with nTregs from *Gclc*$^{fl/fl}$ (WT) or *Foxp3*^{cre}-*Gclc*$^{fl/fl}$ (KO) mice at day 0. Data are mean ± SEM (n = 4); 2 trials. *p < 0.05.

FoxP3 expression. We propose that in Tregs, GSH is a stress sensor, and it routinely scavenges ROS to prevent redox imbalance. Without GSH, ROS accumulate and initiate an NRF2 stress response that increases serine import and synthesis in an effort to produce GSH. The intracellular accumulation of this serine fuels 1CMet driving Treg expansion but also stimulates mTOR, which reduces FoxP3 and dampens Tregs suppressive capacity (Figure S7L). Thus, there is a crucial stress-sensitive feedback loop between GSH and serine availability that controls Treg function.

In conclusion, we have shown that GSH is critical for maintaining Treg function crucial for immune homeostasis. This unexpected, subset-specific role for GSH in restraining serine metabolism in Tregs may offer novel opportunities to modulate their activities. In particular, our results may point the way to new therapies for cancers where subverted Tregs contribute to tumor progression.

Limitations of Study

(1) We observed that *Gclc* regulates Treg metabolism in a subset-specific way that is clearly distinct from its function in conventional T cells. However, it is difficult to postulate a mechanistic explanation. Notably, FoxP3 expression alters the response to GSH depletion, a finding that would be interesting to study in detail. (2) We validated our mouse data in FoxP3-expressing human Tregs, but additional human Treg subsets exist that do not rely on FoxP3. It will be important to investigate whether and how GSH affects the metabolism and function of these subsets. (3) Our study depends on GSH depletion achieved using *in vitro* and *in vivo* mouse and human models. We show that GSH depletion interferes with Treg metabolism and increases ROS and that ROS scavenging normalizes cellular serine concentrations. However, we cannot exclude the possibility that GSH-dependent, but ROS-independent, mechanisms might contribute to our findings.

STAR★METHODS

Detailed methods are provided in the online version of this paper and include the following:

SUPPLEMENTAL INFORMATION

Supplemental Information can be found online at https://doi.org/10.1016/j.cmet.2020.03.004.

ACKNOWLEDGMENTS

We thank S. Storn, A. Oudin (LIH, Luxembourg), and LIH's Animal Welfare Structure for animal services, and we are grateful to the Metabolomics Platform of Luxembourg Centre for Systems Biomedicine (LCSB). We also thank B. Camara (Univ. Marburg, Germany) for technical help; M. Brenner for general support; and Croix-Rouge Luxembourgeoise and all study blood donors. D.B. is supported by FNR-ATTRACT (A14/BM/7632103) and FNR-CORE grants (C15/BM/10355103) and (C18/BM/12691266). D.B., L.B., L.G., J.T., M.Z., and L.S.B are funded by FNR-PRIDE (PRIDE/11012546/NEXTIMMUNE) and D.B., A.E., and P.W. by (PRIDE17/11823097/MicrOH). D.B. and D.G.F. are supported by FNR-RIKEN (TregBar/11228353). V.V. holds grant NIH/NIAAA (5R24AA022057). J.T. was funded by FNR-CORE (C16/BM/11342695). M.L. and D.D.G. are funded by Deutsches Zentrum für Infektionsforschung and University Hospital Giessen Marburg. T.W.M. is funded by grants from the National Multiple Sclerosis Society and Canadian Institutes of Health Research. C.B.K.T. and R.T. are supported by DKH (110663, CBKT, RT) and BMBF (01ZX1401B, CBKT). J.M. is supported by FNR-ATTRACT (A18/BM/11809970) and INTER-BMBF grant (18/13399110).

AUTHOR CONTRIBUTIONS

D.B. and H.K.: study conception and manuscript writing. H.K., D.G.F., L.G., L.B., L.S.B., M.G., L.S., C.D., M.P.M., C.B., G.S.D., S.F., Y.N., J.H., D.D.G., and A.E.: data generation and analysis. R.T. and C.B.K.: histology. R.H. and P.W.: RNA sequencing. O.H.: bioinformatics. H.K., D.G.F., L.S.B., L.S., C.J., J.M., K.H., Y.N., and D.B.: metabolic analyses. T.W.M., M.L., I.S.H., Y.C., M.O., and V.V.: expert comments and reagents. D.B.: study supervision.

DECLARATION OF INTERESTS

The authors declare no competing interests.

Received: June 20, 2019
Revised: December 26, 2019
Accepted: March 2, 2020
Published: March 25, 2020

REFERENCES

Almeida, L., Lochner, M., Berod, L., and Sparwasser, T. (2016). Metabolic pathways in T cell activation and lineage differentiation. Semin. Immunol. *28*, 514–524.

Apostolidis, S.A., Rodríguez-Rodríguez, N., Suárez-Fueyo, A., Dioufa, N., Ozcan, E., Crispín, J.C., Tsokos, M.G., and Tsokos, G.C. (2016). Phosphatase PP2A is requisite for the function of regulatory T cells. Nat. Immunol. *17*, 556–564.

Battello, N., Zimmer, A.D., Goebel, C., Dong, X., Behrmann, I., Haan, C., Hiller, K., and Wegner, A. (2016). The role of HIF-1 in oncostatin M-dependent metabolic reprogramming of hepatic cells. Cancer & Metabolism *4*, 3.

Ben-Sahra, I., Hoxhaj, G., Ricoult, S.J.H., Asara, J.M., and Manning, B.D. (2016). mTORC1 induces purine synthesis through control of the mitochondrial tetrahydrofolate cycle. Science *351*, 728–733.

Bhattacharyya, S., and Saha, J. (2015). Tumour, oxidative stress and host T cell response: cementing the dominance. Scand. J. Immunol. *82*, 477–488.

Bothur, E., Raifer, H., Haftmann, C., Stittrich, A.B., Brüstle, A., Brenner, D., Bollig, N., Bieringer, M., Kang, C.H., Reinhard, K., et al. (2015). Antigen receptor-mediated depletion of FOXP3 in induced regulatory T-lymphocytes via PTPN2 and FOXO1. Nat. Commun. *6*, 8576.

Brenner, D., Brüstle, A., Lin, G.H., Lang, P.A., Duncan, G.S., Knobbe-Thomsen, C.B., St Paul, M., Reardon, C., Tusche, M.W., Snow, B., et al. (2014). Toso controls encephalitogenic immune responses by dendritic cells and regulatory T cells. Proc. Natl. Acad. Sci. USA *111*, 1060–1065.

Bröer, S., and Bröer, A. (2017). Amino acid homeostasis and signalling in mammalian cells and organisms. Biochem. J. *474*, 1935–1963.

Chen, Y., Yang, Y., Miller, M.L., Shen, D., Shertzer, H.G., Stringer, K.F., Wang, B., Schneider, S.N., Nebert, D.W., and Dalton, T.P. (2007). Hepatocyte-specific Gclc deletion leads to rapid onset of steatosis with mitochondrial injury and liver failure. Hepatology *45*, 1118–1128.

Christensen, H.N. (1990). Role of amino acid transport and countertransport in nutrition and metabolism. Physiol. Rev. *70*, 43–77.

Cossarizza, A., Chang, H.D., Radbruch, A., Acs, A., Adam, D., Adam-Klages, S., Agace, W.W., Aghaeepour, N., Akdis, M., Allez, M., et al. (2019). Guidelines for the use of flow cytometry and cell sorting in immunological studies (second edition). Eur. J. Immunol. *49*, 1457–1973.

Dang, E.V., Barbi, J., Yang, H.Y., Jinasena, D., Yu, H., Zheng, Y., Bordman, Z., Fu, J., Kim, Y., Yen, H.R., et al. (2011). Control of T(H)17/T(reg) balance by hypoxia-inducible factor 1. Cell *146*, 772–784.

Delgoffe, G.M., Kole, T.P., Zheng, Y., Zarek, P.E., Matthews, K.L., Xiao, B., Worley, P.F., Kozma, S.C., and Powell, J.D. (2009). The mTOR kinase differentially regulates effector and regulatory T cell lineage commitment. Immunity *30*, 832–844.

Delgoffe, G.M., Pollizzi, K.N., Waickman, A.T., Heikamp, E., Meyers, D.J., Horton, M.R., Xiao, B., Worley, P.F., and Powell, J.D. (2011). The kinase mTOR regulates the differentiation of helper T cells through the selective activation of signaling by mTORC1 and mTORC2. Nat. Immunol. *12*, 295–303.

Devadas, S., Zaritskaya, L., Rhee, S.G., Oberley, L., and Williams, M.S. (2002). Discrete generation of superoxide and hydrogen peroxide by T cell receptor stimulation: selective regulation of mitogen-activated protein kinase activation and fas ligand expression. J. Exp. Med. *195*, 59–70.

Ducker, G.S., and Rabinowitz, J.D. (2017). One-Carbon Metabolism in Health and Disease. Cell Metab. *25*, 27–42.

Dumont, F.J., and Su, Q. (1996). Mechanism of action of the immunosuppressant rapamycin. Life Sci. *58*, 373–395.

Fontenot, J.D., Gavin, M.A., and Rudensky, A.Y. (2003). Foxp3 programs the development and function of CD4+CD25+ regulatory T cells. Nat. Immunol. *4*, 330–336.

Foster, A.C., Rangel-Diaz, N., Staubli, U., Yang, J.Y., Penjwini, M., Viswanath, V., and Li, Y.X. (2017). Phenylglycine analogs are inhibitors of the neutral amino acid transporters ASCT1 and ASCT2 and enhance NMDA receptor-mediated LTP in rat visual cortex slices. Neuropharmacology *126*, 70–83.

Franchina, D.G., Dostert, C., and Brenner, D. (2018a). Reactive oxygen species: involvement in T cell signaling and metabolism. Trends Immunol. *39*, 489–502.

Franchina, D.G., He, F., and Brenner, D. (2018b). Survival of the fittest: Cancer challenges T cell metabolism. Cancer Lett. *412*, 216–223.

Francisco, L.M., Salinas, V.H., Brown, K.E., Vanguri, V.K., Freeman, G.J., Kuchroo, V.K., and Sharpe, A.H. (2009). PD-L1 regulates the development, maintenance, and function of induced regulatory T cells. J. Exp. Med. *206*, 3015–3029.

Fu, J., Xiong, Z., Huang, C., Li, J., Yang, W., Han, Y., Paiboonrungruan, C., Major, M.B., Chen, K.N., Kang, X., and Chen, X. (2019). Hyperactivity of the transcription factor Nrf2 causes metabolic reprogramming in mouse esophagus. J. Biol. Chem. *294*, 327–340.

Gerriets, V.A., Kishton, R.J., Nichols, A.G., Macintyre, A.N., Inoue, M., Ilkayeva, O., Winter, P.S., Liu, X., Priyadharshini, B., Slawinska, M.E., et al. (2015). Metabolic programming and PDHK1 control CD4+ T cell subsets and inflammation. J. Clin. Invest. *125*, 194–207.

Gerriets, V.A., Kishton, R.J., Johnson, M.O., Cohen, S., Siska, P.J., Nichols, A.G., Warmoes, M.O., de Cubas, A.A., MacIver, N.J., Locasale, J.W., et al. (2016). Foxp3 and Toll-like receptor signaling balance T_{reg} cell anabolic metabolism for suppression. Nat. Immunol. *17*, 1459–1466.

Goberdhan, D.C., Wilson, C., and Harris, A.L. (2016). Amino Acid Sensing by mTORC1: Intracellular Transporters Mark the Spot. Cell Metab. *23*, 580–589.

Gülow, K., Kaminski, M., Darvas, K., Süss, D., Li-Weber, M., and Krammer, P.H. (2005). HIV-1 trans-activator of transcription substitutes for oxidative signaling in activation-induced T cell death. J. Immunol. *174*, 5249–5260.

Hamilos, D.L., Zelarney, P., and Mascali, J.J. (1989). Lymphocyte proliferation in glutathione-depleted lymphocytes: direct relationship between glutathione availability and the proliferative response. Immunopharmacology *18*, 223–235.

Hara, K., Yonezawa, K., Weng, Q.P., Kozlowski, M.T., Belham, C., and Avruch, J. (1998). Amino acid sufficiency and mTOR regulate p70 S6 kinase and eIF-4E BP1 through a common effector mechanism. J. Biol. Chem. *273*, 14484–14494.

Henze, A.T., and Mazzone, M. (2016). The impact of hypoxia on tumor-associated macrophages. J. Clin. Invest. *126*, 3672–3679.

Herbig, K., Chiang, E.P., Lee, L.R., Hills, J., Shane, B., and Stover, P.J. (2002). Cytoplasmic serine hydroxymethyltransferase mediates competition between folate-dependent deoxyribonucleotide and S-adenosylmethionine biosyntheses. J. Biol. Chem. *277*, 38381–38389.

Hirotsu, Y., Katsuoka, F., Funayama, R., Nagashima, T., Nishida, Y., Nakayama, K., Engel, J.D., and Yamamoto, M. (2012). Nrf2-MafG heterodimers contribute globally to antioxidant and metabolic networks. Nucleic Acids Res. *40*, 10228–10239.

Hori, S., Nomura, T., and Sakaguchi, S. (2003). Control of regulatory T cell development by the transcription factor Foxp3. Science *299*, 1057–1061.

Huynh, A., DuPage, M., Priyadharshini, B., Sage, P.T., Quiros, J., Borges, C.M., Townamchai, N., Gerriets, V.A., Rathmell, J.C., Sharpe, A.H., et al. (2015). Control of PI(3) kinase in Treg cells maintains homeostasis and lineage stability. Nat. Immunol. *16*, 188–196.

Jackson, S.H., Devadas, S., Kwon, J., Pinto, L.A., and Williams, M.S. (2004). T cells express a phagocyte-type NADPH oxidase that is activated after T cell receptor stimulation. Nat. Immunol. *5*, 818–827.

Kaplan, E., Zubedat, S., Radzishevsky, I., Valenta, A.C., Rechnitz, O., Sason, H., Sajrawi, C., Bodner, O., Konno, K., Esaki, K., et al. (2018). ASCT1 (Slc1a4) transporter is a physiologic regulator of brain d-serine and neurodevelopment. Proc. Natl. Acad. Sci. USA *115*, 9628–9633.

Khattri, R., Cox, T., Yasayko, S.A., and Ramsdell, F. (2003). An essential role for Scurfin in CD4+CD25+ T regulatory cells. Nat. Immunol. *4*, 337–342.

Kim, H.J., Barnitz, R.A., Kreslavsky, T., Brown, F.D., Moffett, H., Lemieux, M.E., Kaygusuz, Y., Meissner, T., Holderried, T.A., Chan, S., et al. (2015). Stable inhibitory activity of regulatory T cells requires the transcription factor Helios. Science *350*, 334–339.

Kong, H., and Chandel, N.S. (2018). Regulation of redox balance in cancer and T cells. J. Biol. Chem. *293*, 7499–7507.

Labuschagne, C.F., van den Broek, N.J., Mackay, G.M., Vousden, K.H., and Maddocks, O.D. (2014). Serine, but not glycine, supports one-carbon metabolism and proliferation of cancer cells. Cell Rep. *7*, 1248–1258.

Lian, G., Gnanaprakasam, J.R., Wang, T., Wu, R., Chen, X., Liu, L., Shen, Y., Yang, M., Yang, J., Chen, Y., et al. (2018). Glutathione de novo synthesis but not recycling process coordinates with glutamine catabolism to control redox homeostasis and directs murine T cell differentiation. eLife *7*, e36158.

Locasale, J.W., Grassian, A.R., Melman, T., Lyssiotis, C.A., Mattaini, K.R., Bass, A.J., Heffron, G., Metallo, C.M., Muranen, T., Sharfi, H., et al. (2011). Phosphoglycerate dehydrogenase diverts glycolytic flux and contributes to oncogenesis. Nat. Genet. *43*, 869–874.

Lowther, D.E., Goods, B.A., Lucca, L.E., Lerner, B.A., Raddassi, K., van Dijk, D., Hernandez, A.L., Duan, X., Gunel, M., Coric, V., et al. (2016). PD-1 marks dysfunctional regulatory T cells in malignant gliomas. JCI Insight *1*, e85935.

Lu, S.C. (2009). Regulation of glutathione synthesis. Mol. Aspects Med. *30*, 42–59.

Ma, E.H., Bantug, G., Griss, T., Condotta, S., Johnson, R.M., Samborska, B., Mainolfi, N., Suri, V., Guak, H., Balmer, M.L., et al. (2017). Serine Is an Essential Metabolite for Effector T Cell Expansion. Cell Metab. *25*, 345–357.

Maddocks, O.D., Berkers, C.R., Mason, S.M., Zheng, L., Blyth, K., Gottlieb, E., and Vousden, K.H. (2013). Serine starvation induces stress and p53-dependent metabolic remodelling in cancer cells. Nature *493*, 542–546.

Maddocks, O.D.K., Athineos, D., Cheung, E.C., Lee, P., Zhang, T., van den Broek, N.J.F., Mackay, G.M., Labuschagne, C.F., Gay, D., Kruiswijk, F., et al. (2017). Modulating the therapeutic response of tumours to dietary serine and glycine starvation. Nature *544*, 372–376.

Mak, T.W., Grusdat, M., Duncan, G.S., Dostert, C., Nonnenmacher, Y., Cox, M., Binsfeld, C., Hao, Z., Brüstle, A., Itsumi, M., et al. (2017). Glutathione Primes T Cell Metabolism for Inflammation. Immunity *46*, 675–689.

Meiser, J., Tumanov, S., Maddocks, O., Labuschagne, C.F., Athineos, D., Van Den Broek, N., Mackay, G.M., Gottlieb, E., Blyth, K., Vousden, K., et al. (2016). Serine one-carbon catabolism with formate overflow. Sci. Adv. *2*, e1601273.

Meiser, J., Schuster, A., Pietzke, M., Vande Voorde, J., Athineos, D., Oizel, K., Burgos-Barragan, G., Wit, N., Dhayade, S., Morton, J.P., et al. (2018). Increased formate overflow is a hallmark of oxidative cancer. Nat. Commun. *9*, 1368.

Meister, A. (1983). Selective modification of glutathione metabolism. Science *220*, 472–477.

Nakagawa, H., Sido, J.M., Reyes, E.E., Kiers, V., Cantor, H., and Kim, H.J. (2016). Instability of Helios-deficient Tregs is associated with conversion to a T-effector phenotype and enhanced antitumor immunity. Proc. Natl. Acad. Sci. USA *113*, 6248–6253.

Nicklin, P., Bergman, P., Zhang, B., Triantafellow, E., Wang, H., Nyfeler, B., Yang, H., Hild, M., Kung, C., Wilson, C., et al. (2009). Bidirectional transport of amino acids regulates mTOR and autophagy. Cell *136*, 521–534.

Nüssing, S., House, I.G., Kearney, C.J., Vervoort, S.J., Beavis, P.A., Oliaro, J., Johnstone, R.W., Trapani, J.A., and Parish, I.A. (2019). Efficient CRISPR/Cas9 gene ablation in uncultured naïve mouse T cells for in vivo studies. bioRxiv. https://doi.org/10.1101/730812.

Park, Y., Jin, H.S., Lopez, J., Elly, C., Kim, G., Murai, M., Kronenberg, M., and Liu, Y.C. (2013). TSC1 regulates the balance between effector and regulatory T cells. J. Clin. Invest. *123*, 5165–5178.

Pearce, E.L., Poffenberger, M.C., Chang, C.H., and Jones, R.G. (2013). Fueling immunity: insights into metabolism and lymphocyte function. Science *342*, 1242454.

Pilipow, K., Scamardella, E., Puccio, S., Gautam, S., De Paoli, F., Mazza, E.M., De Simone, G., Polletti, S., Buccilli, M., Zanon, V., et al. (2018). Antioxidant metabolism regulates CD8+ T memory stem cell formation and antitumor immunity. JCI Insight *3*, 122299.

Possemato, R., Marks, K.M., Shaul, Y.D., Pacold, M.E., Kim, D., Birsoy, K., Sethumadhavan, S., Woo, H.K., Jang, H.G., Jha, A.K., et al. (2011). Functional genomics reveal that the serine synthesis pathway is essential in breast cancer. Nature *476*, 346–350.

Reardon, C., Lechmann, M., Brüstle, A., Gareau, M.G., Shuman, N., Philpott, D., Ziegler, S.F., and Mak, T.W. (2011). Thymic stromal lymphopoetin-induced expression of the endogenous inhibitory enzyme SLPI mediates recovery from colonic inflammation. Immunity *35*, 223–235.

Ren, W., Liu, G., Yin, J., Tan, B., Wu, G., Bazer, F.W., Peng, Y., and Yin, Y. (2017). Amino-acid transporters in T-cell activation and differentiation. Cell Death Dis. *8*, e2655.

Ron-Harel, N., Santos, D., Ghergurovich, J.M., Sage, P.T., Reddy, A., Lovitch, S.B., Dephoure, N., Satterstrom, F.K., Sheffer, M., Spinelli, J.B., et al. (2016). Mitochondrial biogenesis and proteome remodeling promote one-carbon metabolism for T cell activation. Cell Metab. *24*, 104–117.

Rubtsov, Y.P., Rasmussen, J.P., Chi, E.Y., Fontenot, J., Castelli, L., Ye, X., Treuting, P., Siewe, L., Roers, A., Henderson, W.R., Jr., et al. (2008). Regulatory T cell-derived interleukin-10 limits inflammation at environmental interfaces. Immunity *28*, 546–558.

Rudensky, A.Y. (2011). Regulatory T cells and Foxp3. Immunol. Rev. *241*, 260–268.

Sabharwal, S.S., and Schumacker, P.T. (2014). Mitochondrial ROS in cancer: initiators, amplifiers or an Achilles' heel? Nat. Rev. Cancer *14*, 709–721.

Schäfer, M., Dütsch, S., auf dem Keller, U., Navid, F., Schwarz, A., Johnson, D.A., Johnson, J.A., and Werner, S. (2010). Nrf2 establishes a glutathione-mediated gradient of UVB cytoprotection in the epidermis. Genes Dev. *24*, 1045–1058.

Sena, L.A., and Chandel, N.S. (2012). Physiological roles of mitochondrial reactive oxygen species. Mol. Cell *48*, 158–167.

Sena, L.A., Li, S., Jairaman, A., Prakriya, M., Ezponda, T., Hildeman, D.A., Wang, C.R., Schumacker, P.T., Licht, J.D., Perlman, H., et al. (2013). Mitochondria are required for antigen-specific T cell activation through reactive oxygen species signaling. Immunity *38*, 225–236.

Shi, L.Z., Wang, R., Huang, G., Vogel, P., Neale, G., Green, D.R., and Chi, H. (2011). HIF1alpha-dependent glycolytic pathway orchestrates a metabolic checkpoint for the differentiation of TH17 and Treg cells. J. Exp. Med. *208*, 1367–1376.

Shrestha, S., Yang, K., Guy, C., Vogel, P., Neale, G., and Chi, H. (2015). Treg cells require the phosphatase PTEN to restrain TH1 and TFH cell responses. Nat. Immunol. *16*, 178–187.

Suthanthiran, M., Anderson, M.E., Sharma, V.K., and Meister, A. (1990). Glutathione regulates activation-dependent DNA synthesis in highly purified normal human T lymphocytes stimulated via the CD2 and CD3 antigens. Proc. Natl. Acad. Sci. USA *87*, 3343–3347.

Tibbetts, A.S., and Appling, D.R. (2010). Compartmentalization of Mammalian folate-mediated one-carbon metabolism. Annu. Rev. Nutr. *30*, 57–81.

Tone, Y., Furuuchi, K., Kojima, Y., Tykocinski, M.L., Greene, M.I., and Tone, M. (2008). Smad3 and NFAT cooperate to induce Foxp3 expression through its enhancer. Nat. Immunol. *9*, 194–202.

Wang, Q., Liberti, M.V., Liu, P., Deng, X., Liu, Y., Locasale, J.W., and Lai, L. (2017). Rational design of selective allosteric inhibitors of PHGDH and serine synthesis with anti-tumor activity. Cell Chem. Biol. *24*, 55–65.

Weinberg, S.E., Singer, B.D., Steinert, E.M., Martinez, C.A., Mehta, M.M., Martinez-Reyes, I., Gao, P., Helmin, K.A., Abdala-Valencia, H., Sena, L.A., et al. (2019). Mitochondrial complex III is essential for SC of regulatory T cells. Nature *565*, 495–499.

Wing, K., and Sakaguchi, S. (2010). Regulatory T cells exert checks and balances on self tolerance and autoimmunity. Nat. Immunol. *11*, 7–13.

Yamamoto, T., Nishizaki, I., Nukada, T., Kamegaya, E., Furuya, S., Hirabayashi, Y., Ikeda, K., Hata, H., Kobayashi, H., Sora, I., and Yamamoto, H. (2004). Functional identification of ASCT1 neutral amino acid transporter as the predominant system for the uptake of L-serine in rat neurons in primary culture. Neurosci. Res. *49*, 101–111.

Yang, X., Xia, R., Yue, C., Zhai, W., Du, W., Yang, Q., Cao, H., Chen, X., Obando, D., Zhu, Y., et al. (2018). ATF4 regulates $CD4^+$ T cell immune responses through metabolic reprogramming. Cell Rep. *23*, 1754–1766.

Ye, J., Mancuso, A., Tong, X., Ward, P.S., Fan, J., Rabinowitz, J.D., and Thompson, C.B. (2012). Pyruvate kinase M2 promotes de novo serine synthesis to sustain mTORC1 activity and cell proliferation. Proc. Natl. Acad. Sci. USA *109*, 6904–6909.

Ye, J., Fan, J., Venneti, S., Wan, Y.W., Pawel, B.R., Zhang, J., Finley, L.W., Lu, C., Lindsten, T., Cross, J.R., et al. (2014). Serine catabolism regulates mitochondrial redox control during hypoxia. Cancer Discov. *4*, 1406–1417.

Yi, J.S., Holbrook, B.C., Michalek, R.D., Laniewski, N.G., and Grayson, J.M. (2006). Electron transport complex I is required for CD8+ T cell function. J. Immunol. *177*, 852–862.

STAR★METHODS

KEY RESOURCES TABLE

REAGENT or RESOURCE	SOURCE	IDENTIFIER
Antibodies		
CD4-PE Clone GK1.5 (1:200)	Biolegend	Cat #100408; RRID:AB_312693
CD25-PE Clone PC61 (1:200)	Biolegend	Cat #102008; RRID:AB_312857
IRF4-PE Clone IRF4.3F4 (1:200)	Biolegend	Cat #646404; RRID:AB_2563005
F4/80-PE Clone BM8 (1:200)	Biolegend	Cat #123110 ;RRID:AB_893486
CD185-PE Clone L138D7 (1:200)	Biolegend	Cat #145504; RRID:AB_2561968
CD90.1-PE Clone HIS51 (1:200)	Thermo Fisher	Cat #12-0900-81; RRID:AB_465773
CD45RB-PE Clone C363-16A (1:200)	Biolegend	Cat #103308; RRID:AB_313015
Ki-67-PE Clone 16A8 (1:200)	Biolegend	Cat #652404; RRID:AB_2561525
TGF-β1,-β2,-β3-PE Clone 1D11 (1:200)	R&D Systems	Cat #IC1835P; RRID:AB_884508
Tbet-PE/Cy7 Clone 4B10 (1:200)	Biolegend	Cat #644824; RRID:AB_2561761
F4/80-PE/Cy7 Clone BM8 (1:200)	Biolegend	Cat #123114; RRID:AB_893478
Bcl6-PE/Cy7 Clone 7D1 (1:200)	Biolegend	Cat #358512; RRID:AB_2566196
Helios-PE/Cy7 Clone 22F6 (1:200)	Biolegend	Cat #137236; RRID:AB_2565990
pSTAT5-PE/Cy7 Clone SRBCZY (1:200)	Thermo Fisher	Cat #25-9010-42; RRID:AB_2573534
CD8a-APC Clone 53-6.7 (1:200)	Biolegend	Cat #100712; RRID:AB_312751
IFN-γ-APC Clone XMG1.2 (1:200)	Biolegend	Cat #505810; RRID:AB_315404
Foxp3-APC Clone FJK-16 s (1:200)	Thermo Fisher	Cat #17-5773-82; RRID:AB_469457
pS6-APC Clone cupk43k (1:200)	Therno Fisher	Cat #17-9007-42; RRID:AB_2573270
GL7-APC Clone GL7 (1:200)	Biolegend	Cat #144606; RRID:AB_2562185
I-A/I-E-APC Clone M5/114.15.2 (1:200)	Biolegend	Cat #107614; AB_313329
CD98-APC Clone RL388 (1:200)	Biolegend	Cat #128210; RRID:AB_2254922
pS473-APC Clone M89-61 (1:200)	BD Biosciences	Cat #560343; RRID:AB_1645397
Granzyme B-APC Clone NGZB (1:200)	Thermo Fisher	Cat #50-8898-82; RRID:AB_11219679
IgG (H+L)-APC (1:500)	Thermo Fisher	Cat #A21244; RRID:AB_141663
CD3ε-APC-Cy7 Clone 145-2C11(1:200)	Biolegend	Cat #100330; RRID:AB_1877170
CD86-FITC Clone GL-1 (1:200)	Biolegend	Cat #105006; RRID:AB_313149
Perforin-FITC Clone eBioOMAK-D (1:200)	Thermo Fisher	Cat #11-9392-82; RRID:AB_465447
RORγT-BV421 Clone Q31-378 (1:200)	BD Biosciences	Cat #562894; RRID:AB_2687545
CD95-BV421 Clone Jo2 (1:200)	BD Biosciences	Cat #562633; RRID:AB_2737690
CD152-BV421 Clone UC10-4B9 (1:200)	Biolegend	Cat #106312; RRID:AB_2563063
CD134-BV421 Clone OX-86 (1:200)	Biolegend	Cat #119411; RRID:AB_10962569
CD62L-Pacific Blue Clone MEL-14 (1:200)	Biolegend	Cat #104424; RRID:AB_493380
CD25-Pacific Blue Clone PC61 (1:200)	Biolegend	Cat #102022; RRID:AB_493643
TNF-α-Pacific Blue Clone MP6-XT22 (1:200)	Biolegend	Cat #506318; RRID:AB_893639
pmTOR-Pacific Blue Clone MRRBY (1:200)	Biolegend	Cat #48-9718-42; RRID:AB_2574127
c-Myc-Pacific Blue Clone D84C12 (1:200)	Cell Signaling	Cat #14426; RRID:AB_2798478
Foxp3-V450 Clone MF23 (1:200)	BD Biosciences	Cat #561293; RRID:AB_10611728
CD44-PerCP/Cy5.5 Clone IM7 (1:200)	Biolegend	Cat #103032; RRID:AB_2076204
CD86-PerCP Clone GL-1 (1:200)	Biolegend	Cat #105026; RRID:AB_893417
CD45R/B220-BV510 Clone RA3-6B2 (1:200)	Biolegend	Cat #103248; RRID:AB_2650679
CD69-BV605 Clone H1.2F3 (1:200)	Biolegend	Cat #104530; RRID:AB_2563062
IL-17A-BV605 Clone TC11-18H10 (1:200)	BD Biosciences	Cat #564169; RRID:AB_2738640
CD279-BV605 Clone 29F.1A12 (1:200)	Biolegend	Cat #135220; RRID:AB_2562616
CD4-BV785 Clone GK1.5 (1:200)	Biolegend	Cat #100453; RRID:AB_2565843

(*Continued on next page*)

Continued

REAGENT or RESOURCE	SOURCE	IDENTIFIER
CD19-BV785 Clone 6D5 (1:200)	Biolegend	Cat #115543; RRID:AB_11218994
Glut1-Alexa Fluor®488 Clone EPR3915 (1:200)	Abcam	Cat #ab195359; RRID:AB_2714026
pSMAD3 Ser423, Ser425	Thermo Fisher	Cat #44-246G; RRID:AB_2533615
pAMPK alpha-1,2 (Thr172)	Thermo Fisher	Cat #44-1150G; RRID:AB_2533585
Purified anti-mouse CD3ϵ Clone 145-2C11	Biolegend	Cat #100340; RRID:AB_11149115
Purified anti-mouse CD28 Clone	Biolegend	Cat #102112; RRID:AB_312877
Human CD3/CD28 T Cell activator	StemCell Technologies, Inc.	Cat #10911 10971; RRID:AB_2827806
Anti-Mouse IFN-γ Clone XMG1.2	BD Biosciences	Cat #554408; RRID:AB_395373
Biological Samples		
Healthy control buffy coat	Croix-Rouge Luxembourgeoise	N/A
Chemicals, Peptides, and Recombinant Proteins		
RPMI 1640 (without L-Glutamine)	Lonza	#BE12-167F
RMPI 1640 (without glucose, serine, glycine)	Teknova	#50-190-8105
DMEM (with glucose and L-Glutamine)	Lonza	#BE12-604F
Hank's Balanced Salt Solutions	Lonza	#BE10-543F
SILAC RPMI 1640 Flex Media	GIBCO	#15347143
Seahorse XF base medium without phenol red	Agilent Technologies	#103335-100
PBS	Lonza	#BE17-516F
FBS	Sigma-Aldrich	#TMS-013-B
Penicillin/Streptomycin	GIBCO	#11548876
L-Glutamine	Sigma-Aldrich	#G3126-100G
2-mercaptoethanol	GIBCO	#11508916
Sodium pyruvate	GIBCO	#12539059
Recombinant human TGF-β	R&D Systems	#240-B-002
recombinant human IL-2	Miltenyi Biotec	#130-120-333
2-Deoxy-D-glucose	Sigma-Aldrich	#D6134-1G
D-(+)-glucose	Sigma-Aldrich	#G8270-5KG
Oligomycin A	Sigma-Aldrich	#75351-5MG
FCCP	Sigma-Aldrich	#C2920-10MG
Antimycin A	Sigma-Aldrich	#A8674-25MG
Rotenone	Sigma-Aldrich	#R8875-1G
Phorbol 12-myristate 13-acetate (PMA)	Sigma-Aldrich	#P8139-1MG
Calcium Ionophore	Sigma-Aldrich	#C7522-1MG
N-Acetyl-L-cysteine	Sigma-Aldrich	#A7250-50G
L-Glutathione reduced	Sigma-Aldrich	#G4251-10G
Rapamycin	Invivogen	#tlrl-rap
Rapamycin	LC Laboratories	N/A
L−(+)-α-Phenylglycine	Sigma-Aldrich	#237647-25G
4-Hydroxytamoxifen	Sigma-Aldrich	#H6278-10MG
PKUMDL-WQ-2101	Sigma-Aldrich	#SML1970-5MG
L-buthionine-sulfoximine	Sigma-Aldrich	#B2515-1G
SHIN1	Aobious	#AOB36697
Thymidine, [6-3H]-, 5mCi (185MBq)	Perkin Elmer	# NET355005MC
SYBR™ Fast Green Master Mix	Applied Biosystems	# 10459604
Corning™ Cell-Tak Cell and Tissue Adhesive	Thermo Fisher	# 10317081
$^{13}C_6$-glucose	Cambridge Isotope Lab	# CLM-1396
$^{13}C_5$-L-Glutamine	Cambridge Isotope Lab	# CLM-1822-H
$^{13}C_3$-serine	Cambridge Isotope Lab	#CLM-1574-H
GolgiPlug™	BD Biosciences	#555029

(*Continued on next page*)

Continued

REAGENT or RESOURCE	SOURCE	IDENTIFIER
Cell Trace Violet	Thermo Fisher	#C34557
Mitotracker Deep Red	Thermo Fisher	# M22426
Molecular Probes™ Carboxy-H2DCFDA	Thermo Fisher	#11500146
Molecular Probes™ 2-NBDG	Thermo Fisher	#11569116
Zombie NIR™ Fixable Viability Kit	Biolegend	#423106
Saponin	Sigma-Aldrich	#S4521-25G
Formaldehyde	Sigma-Aldrich	#252549-1L
HEPES	Sigma-Aldrich	#H4034-100G
EDTA	Sigma-Aldrich	#E9884-100G
Polyethylene glycol	Sigma-Aldrich	#P1458-50ML
Ethanol	VWR	#20821330
Tween 80	Sigma-Aldrich	#P1754-1L
Methanol	Sigma-Aldrich	#1060351000
Chloroform	Sigma-Aldrich	#34854-1L-M
Trichloroacetic acid	Sigma-Aldrich	#T6399-100G
DNase I	Sigma-Aldrich	#10104159001
Liberase	Sigma-Aldrich	#5401020001
Percoll®	Sigma-Aldrich	#GE17-0891-01
HiSep™ LSM 1077	HiMedia Laboratory	#LS001-500ML
Critical Commercial Assays		
Naive $CD4^+$ T Cell Isolation Kit	Miltenyi Biotec	#130-104-453
CD4+ T Cell Isolation Kit	Miltenyi Biotec	#130-104-454
CD90.1 Microbeads	Miltenyi Biotec	#130-094-523
$CD4^+$ $CD25^+$ Regulatory T Cell Isolation Kit	Miltenyi Biotec	#130-091-041
Tumor Dissociation Kit	Miltenyi Biotec	#130-096-730
CD45 (TIL) Microbeads	Miltenyi Biotec	#130-110-618
Naive CD4+ T Cell Isolation Kit II, human	Miltenyi Biotec	#130-094131
Seahorse XFe96 Fluxpak	Agilent Technologies	#102416-100
Foxp3/Transcription Factor Staining Buffer Set	Thermo Fisher	#15151976
Fixation/Permeabilization solution kit	BD Biosciences	#554701
Lyse/Fix Buffer 5x	BD Biosciences	#558049
Perm buffer III	BD Biosciences	#558050
QuantiTect Reverse Transcription Kit	QIAGEN	#205314
RNA 6000 Nano Kit	Agilent Technologies	#5067-1511
NucleoSpin RNA 250	Macherey-Nagel	#740 955 250
IFN gamma Mouse Uncoated ELISA Kit	Thermo Fisher	#88-7314-88
TNF alpha Mouse Uncoated ELISA Kit	Thermo Fisher	#88-7324-88
Invitrogen ™ IL-2 Mouse Uncoated ELISA Kit	Thermo Fisher	#15520997
Experimental Models: Cell Lines		
B16F10	Dr. Philipp Lang	N/A
MC38	ATCC	N/A
Experimental Models: Organisms/Strains		
$Gclc^{fl/fl}$: B6	Mak et al., 2017	N/A
$Foxp3^{YFP\text{-}Cre}$: B6	The Jackson laboratory	#016959
$Foxp3^{eGFP\text{-}Cre\text{-}ERT2}$: B6	The Jackson laboratory	#016961
$Rag1^{-/-}$: B6	The Jackson laboratory	#002216
$IFN\gamma^{-/-}$: B6	The Jackson laboratory	#002287

(*Continued on next page*)

Continued

REAGENT or RESOURCE	SOURCE	IDENTIFIER
Deposited Data		
RNA-Seq	This paper	N/A
Oligonucleotides		
Gclc: F:GGCTCTCTGCACCATCACTT R:GTTAGAGTACCGAAGCGGGG	This paper	N/A
Foxp3: F:CCCATCCCCAGGAGTCTTG R:ACCATGACTAGGGGCACTGTA	This paper	N/A
Slc1a4: F:TGCTCTGGCGTTCATCATCA R:AGTGAATGCGGCAACCACAA	This paper	N/A
Slc1a5: F:TGGCCAGCAAGATTGTGGAGAT R:TTTGCGGGTGAAGAGGAAGT	This paper	N/A
HPRT: F:TCAGTCAACGGGGGACATAAA R:GGGGCTGTACTGCTTAACCAG	This paper	N/A
TBP: F:GAAGAACAATCCAGACTAGCAGCA R:CCTTATAGGGAACTTCACATCACAG	This paper	N/A
PHGDH: F:ATGGCCTTCGCAAATCTGC R:AGTTCAGCTATCAGCTCCTCC	This paper	N/A
sgRNA Phgdh C*U*U*GCCUUGCCUUGCCCAUG G*G*C*AAGAGCUCACCUUCUUC U*U*C*UUACAGGCAGAUUCCCC	Synthego	N/A
sgRNA Slc1a4 A*C*C*AGGCUGCAAACCACCAG G*C*A*UCUCGCCCGGGAAGGCC C*C*U*CAGCGCCGCGCCCAUGC	Synthego	N/A
Recombinant DNA		
pMIT-Foxp3-CD90.1	Dr. Michael Lohoff	N/A
pMIT-CD90.1	Dr. Michael Lohoff	N/A
pMIG-RI-STAT5-CA	Dr. Michael Lohoff	N/A
pMIG-RI	Dr. Russell Jones	N/A
pMIG-RI-Gclc	This paper	N/A
pMIG-RI-Smad3	This paper	N/A
Software and Algorithms		
FlowJo Software	Tree Star	N/A
Graphpad Prism	GraphPad Software, Inc	N/A
Wave Software	Agilent	N/A
Adobe Illustrator	Adobe systems	N/A

LEAD CONTACT AND RESOURCE SHARING

Further information and requests for resources or reagents should be directed to and will be made available upon reasonable request by the Lead Contact, Dirk Brenner (dirk.brenner@lih.lu).

EXPERIMENTAL MODEL AND SUBJECT DETAILS

Primary Cell Culture

Natural regulatory T cells (nTregs), naive $CD4^+$ T cells, and $CD4^+$ and $CD8^+$ Tconv were isolated from mouse spleen and LN by magnetic bead sorting (Miltenyi Biotec). To induce regulatory T cells (iTregs), 2×10^5 naive T cells were cultured for four days in the

presence of plate bound anti-CD3 antibody (αCD3; 5 μg/mL, Biolegend), soluble anti-CD28 antibody (αCD28; 1 μg/mL, Biolegend), recombinant human TGF-β1 (4 ng/mL, Bio-Techne), IL-2 (50U/mL, Miltenyi Biotec) and anti-IFNγ antibody (αIFNγ; 5 μg/mL, BD Biosciences). Naive T cells were cultured in T cell media consisting of RPMI-1640 medium supplemented with 10% FCS (Sigma), 1% Penicillin/Streptomycin (GIBCO), 1% L-Glutamine (Sigma), and 55μM β-mercaptoethanol (GIBCO). To isolate nTregs, the cells were labeled using the $CD4^+CD25^+$ Regulatory T cells isolation kit (Miltenyi Biotec) and magnetically sorted using the autoMACS® Pro Separator (Miltenyi Biotec) according to the manufacturer's protocol. nTregs were cultured in T cell media in the presence of plate bound anti-CD3 antibody (αCD3; 5 μg/mL, Biolegend), soluble anti-CD28 antibody (αCD28; 5 μg/mL, Biolegend), IL-2 (500U, Miltenyi Biotec). To induce acute Gclc deletion, naive $CD4^+$ T cells were differentiated into iTregs *in vitro* in the presence of vehicle or 100 nM 4-hydroxytamoxifen (4-OHT) (Sigma) for 4 days.

For the human studies, buffy coats from healthy donors were provided by Croix-Rouge Luxembougeoise. The experimental setup was approved by the Croix-Rouge Luxembourgeoise (LIH-2019-0006). Human PBMCs were isolated using the Ficoll separation (HiSep™ LSM 1077, HiMedia Laboratory GmbH). Human naive $CD4^+$ T cells were isolated using the Human Naive $CD4^+$ T cells isolation kit II (Miltenyi Biotec). 2×10^5 naive $CD4^+$ T cells were cultured for six days with ImmunoCult™ Human CD3/CD28 T cell activator (StemCell Technologies, Inc.), according to the manufacturer's instructions. IL-2 (100U/mL) and TGF-β1 (4 ng/mL, Bio-Techne) were supplemented. The cells were differentiated in T cell media containing RPMI-1640 medium supplemented with 10% FCS (Sigma), 1% Penicillin/Streptomycin (GIBCO), 1% L-Glutamine (Sigma), and 100μM sodium pyruvate (GIBCO).

Mouse Models

Gclc$^{fl/fl}$ mice have been previously described (Chen et al., 2007) and were crossed to *Foxp3*^{cre}-expressing mice [B6.129(Cg)-*Foxp3*$^{tm4(YFP/icre)Ayr}$/J] and *Foxp3*$^{tm9(EGFP/cre/ERT2)Ayr}$/J (Jackson Laboratory). B6.129S7-Ifng^{tm1Ts}/J mice were obtained from The Jackson Laboratory. C57BL/6 and *Rag1*$^{-/-}$ mice were originally purchased from The Jackson Laboratory and bred in the SPF facility of the Luxembourg Institute of Health (LIH). Male and age-matched mice (6-12 weeks old) were used for all experiments unless otherwise indicated. For the serine- and glycine-free chow experiments, the mice were fed with normal or serine- and glycine-free chow as of 3 weeks of age (post weaning). The food was purchased from Special Diets Services (SDS, diet code 827030).

METHOD DETAILS

Cell Sorting and Flow Cytometry

To stain extracellular surface molecules, the cells were incubated in FACS buffer (PBS with 1% FCS and 5mM EDTA pH 8.0) together with specific antibodies for at least 30 min at 4°C protected from light. To detect intracellular phosphoproteins, the cells were fixed in 2% formaldehyde and permeabilized in 0.01% saponin. To identify transcription factors and intracellular nuclear proteins, the cells were fixed using the eBioscience Foxp3/Transcription Factor Fixation kit and permeabilized using the respective permeabilization buffer, according to the manufacturer's protocol. For cytokine stainings, the cells were fixed using the BD Cytofix/Cytoperm solution according to the manufacturers instructions. To stain intracellular ROS, the cells were incubated with dichlorofluorescein diacetate (DCF-DA, Sigma) for 30 min at 37°C in RPMI medium (non-supplemented). To measure NBDG uptake, the cells were incubated with 50 μM2-NBDG (Thermo Fisher Scientific) for 2 h at 37°C in glucose free RPMI (non-supplemented). For cell sorting, the cells were sorted using Aria II (BD Biosciences). Experiments were done in accordance with the guidelines for flow cytometry and cell sorting (Cossarizza et al., 2019).

Treg Suppression Assay

Purified nTregs ($CD4^+CD25^+$) and Tconv (Tconv; $CD4^+$ $CD25^-$) were magnetically sorted using a $CD4^+CD25^+$ Regulatory T cell Isolation Kit (Miltenyi Biotec). Tconv were labeled with CellTrace™ Violet Cell Proliferation (ThermoFisher Scientific) and cultured with irradiated antigen-presenting cells plus αCD3, with or without Tregs at various Tconv:Treg ratios. After 72 h, the proliferation of Teff cells was analyzed by flow cytometry.

T Cell Transfer-Induced Colitis

Rag1$^{-/-}$ mice were adoptively transferred with 4×10^5 WT Teffs ($CD4^+CD45RB^{hi}$), either alone or in combination with 2×10^5 Tregs ($CD4^+CD45RB^{low}$) from *Gclc*$^{fl/fl}$ or *Foxp3*^{cre}-*Gclc*$^{fl/f}$ mice. To this end, cells were purified by FACS sorting (Aria II, BD) prior to intravenous (i.v.) injection into mice. Recipient mice were weighed and examined every day for signs of disease. Cells from mesenteric LN were subjected to flow cytometric analysis. Colonic tissues were fixed and stained with H&E and αCD3 Ab and subjected to histological analyses.

Isotopic Labeling

Tregs were incubated for 24 h in RPMI 1640 containing [U-$^{13}C_6$]-glucose (11.1 mmol/L; Cambridge Isotope Laboratories) or [U-^{13}C]-glutamine (2 mmol/L; Cambridge Isotope Laboratories), both conjugated to bovine serum albumin (Sigma). For serine tracing, cells were cultured for 24 h in serine/glycine-free medium (Teknova) supplemented with 0.01 g/l glycine plus 400μM [U-$^{13}C_3$]-serine (Eurisotop (CLM-1574-H). Extraction of intracellular metabolites, GC-MS measurement, MID calculations, determinations of fractional carbon contributions, and substractions of natural isotope abundance were performed as described (Battello et al., 2016) using the MetaboliteDetector software package. Glucose, lactate and amino acid concentrations were determined using an YSI 2950D

Biochemistry Analyzer (YSI Incorporated). Formate quantification was performed following MCF derivatization and GC-MS analysis as previously described (Meiser et al., 2016).

Tumor Model and Treg Adoptive Transfer

B16F10 melanoma cells (2x10^5; ATCC) in 100 μl sterile PBS were injected subcutaneously into the shaved left flank of each mouse. Tumor volume was calculated daily: tumor volume = $\frac{length*diameter^2}{2}$. Mice were sacrificed at day 30 or when tumor volume exceeded 1.2 cm^3. For the Treg transfers, 1x10^6 of *Gclc*$^{fl/fl}$ and *Foxp3*^{cre}-*Gclc*$^{fl/fl}$ Tregs were magnetically sorted using the $CD4^+CD25^+$ Regulatory T cells isolation kit (Miltenyi Biotec) and magnetically sorted using the autoMACS® Pro Separator (Miltenyi Biotec) according to the manufacturer's protocol. Purified Tregs were intravenously injected prior B16 melanoma inoculation at experimental day 0.

TILs Isolation

Isolated tumors were cut into small pieces and digested with enzymes A, D, and R obtained from the Mouse Tumor Dissociation Kit (Miltenyi Biotec) according to the manufacturer's protocol. The digestion was followed by tumor dissociation using GentleMACS Octo Dissociator (37C_m_TDK_1). The cells were then filtered through 70 μm filter and washed with RPMI. The TILS were isolated using CD45 (TIL) Microbeads (Miltenyi Biotec) according to the manufacturer's protocol. The TILs were analyzed by flow cytometry or stimulated by PMA/Ionomycin for cytokine analysis.

In Vivo Rapamycin Treatment

Rapamycin was prepared in 100% ethanol and diluted in vehicle (5% polyethylene glycol and 5% Tween 80). Male *Gclc*$^{fl/fl}$ and *Foxp3*^{cre}-*Gclc*$^{fl/fl}$ mice of age 6 weeks were intraperitoneally injected with 100μg rapamycin (LC Laboratories) or vehicle every other day for 30 days. Mice were sacrificed at day 30 and organs extracted for analysis.

Expression Plasmids and Retroviral Transduction

The plasmids pMIT-Foxp3-CD90.1, pMIT-CD90.1 and pMig-RI-STAT5-CA (constitutively active) were provided by M. Lohoff (University of Marburg, Germany) (Bothur et al., 2015). pMigRI-GFP was provided by R. Jones (Van Andel Institute, USA). Murine full length cDNA of *Gclc* and *Smad3* were synthesized into pMigRI-GFP using the EcoRI restriction site (GeneCust, France). For retroviral transduction, retroviral supernatants were added to *in vitro*-differentiated iTreg cells whose culture medium had been stored. Cells and viral supernatants were centrifuged at 2700 rpm for 1.5 h at 37°C to achieve spin infection. Infected cells were re-cultured in the stored culture medium for 72 h before MACS-sorting to identify CD90.1 co-expression or fluorescence based FACS cell sorting. Infected iTreg cells were used for experiments as described in the main text.

Cytokine Quantification

To induce intracellular cytokine expression, T cells were restimulated *in vitro* with phorbol 12-myristate 13-acetate (PMA; Sigma, 50ng/mL) plus calcium ionophore A23187 (Ionomycin; Sigma, 750ng/mL) for 6 h. The cells were analyzed with flow cytometry. Serum concentrations of IL-2, TNF, IFNγ, and immunoglobulins were quantified by ELISA using the appropriate kits and protocols from eBioscience.

CRISPR/Cas9 Genomic Editing

1x10^6 enriched naive CD4 T cells were cultured in Treg skewing media for 48 h prior transfection with sgRNAs. sgRNAs targeting murine *Asct1* and *Phgdh* were obtained from Synthego (CRISPRevolution sgRNA EZ Kit, Synthego). sgRNAs were electroporated as described previously (Nüssing et al., 2019). Briefly, 1 μl of 0.3 nmol sgRNAs were incubated with 0.3 μl Cas9 Nuclease to a final volume of 5 μl for 10 min at room temperature. Pre differentiated CD4 regulatory T cells were resuspended in 95 μl P3 buffer (P3 primary cell 4D-Nucleofector™ system, mixed with the pre-prepared sgRNA/Cas9 solution, and subjected to electroporation. The cells were transferred to 1ml RPMI containing 10% FCS, glutamine, pen/strep and 100U IL-2 and cultured for 72 h before further analysis.

Quantitative PCR

RNA was isolated using a NucleoSpin RNA Kit (Macherey-Nagel) and cDNA was prepared using a QuantiTect Rev. Transcription Kit (QIAGEN). RT-PCR was carried out using Sybrgreen Master Mix (ABI) and the primers listed under 'Oligonucleotides'. Reactions were run on an ABI 7500HT Fast qRT-PCR instrument. Data were normalized to GAPDH transcription and analyzed using the ΔΔCt method as previously described (Mak et al., 2017).

Histology and Immunohistochemistry

Specimens for histology and immunohistochemistry analyses were prepared and examined as previously described (Brenner et al., 2014).

GSH, GSSG, and Formate Determination

The GSH content of 2x10^5 Treg cells/well was measured by GSH-Glo (Promega). Formate release into culture medium was quantified using a formate assay kit (Sigma). Intracellular GSH and GSSG was quantified as reported by (Meiser et al., 2016). Briefly, 2 million Treg cells were harvested and washed with 0.9% saline solution before adding 100 μl ice-cold MilliQ water with 20 μg/mL labeled

GSH (13C2, 15N; Cambridge Isotope Laboratories) as internal standard, followed by an equal volume of ice-cold 5% trichloroacetic acid. Cells were shaken at 1400 rpm at 4°C for 10 min and subsequently centrifuged at 21.000xg and 4°C for 5 min. 150 μl of the supernatant were transferred into a 2-ml-LC vial with micro insert. 10 μl of the extract were injected into an Agilent 1290 Infinity II equipped with a Waters Acquity UPLC HSS T3 (100 × 2.1 mm, 1.8 μm). Mobile phase A was composed of 0.1% formic acid and B was composed of methanol with 0.1% formic acid. The system was operated at 0.45 mL/min. The total run time of the method was 20 min starting with 1% B for 10 min, then increasing to 99% B at 12 min, which was held for 2 min. B was reduced to 1% after 15 min and kept for the rest of the run. Mass spectra were acquired in positive mode using a Bruker maXis.

Lamina Propria Isolation

Colons were cut longitudinally and incubated for 10 min at 37°C in Hank's Balanced Salt Solution (HBSS) containing 15mM HEPES, 10% FCS and 5mM EDTA. The colonic tissue was recovered in a 100 μM strainer and transferred again in HBSS (15mM HEPES, 10% FCS, 5mM EDTA) to re-incubate once more. After collection in a 100 μM strainer, the tissue was washed in RPMI containing 15mM HEPES, 10% FCS for 5 min at 37°C. Then the tissue was cut into small pieces, and digested for 30 min at 37°C in 10ml RPMI containing 0.1 mg/mL DNase I (Roche) and 0.083 mg/mL Liberase (Roche). Tissue suspensions were passed through a 40 μM strainer, pelleted, and overlayed on a 40%–75% Percoll gradient. After centrifugation at 800 g for 20 min at 20°C (without break), lamina propria lymphocytes (LPLs) were collected at the 40%–75% Percoll interface, washed, and resuspended in RPMI containing 10% FCS. Lamina propria lymphocytes were identified by flow cytometric analysis.

Metabolic Phenotyping

iTreg cells were seeded XF Seahorse DMEM medium in a density of 3×10^5 cells/well. The extracellular acidification rate (ECAR) and oxygen consumption rate (OCR) were determined using the XF Glycolytic Stress Test and XF Cell Mitochondrial Stress Test kits, respectively, according to the manufacturer's protocol (Agilent).

RNA-Sequencing

Libraries were prepared with 500 ng total RNA using the Total RNA TruSeq mRNA Stranded Library Prep Kit (Illumina) according to the manufacturer's protocol. Briefly, mRNA pulldown was performed using an oligodT primer attached to magnetic beads. To preserve strandness information, the second strand synthesis was performed using dUTP incorporation, ensuring that only the first strand was PCR-amplified. The libraries were quantified using the Qubit dsDNA HS assay kit (Thermofisher) and an Agilent 2100 Bioanalyzer. The pooled library was sequenced on an Illumina NextSeq500 instrument according to the manufacturer's instructions.

Transcriptomic and Data Analyses

Demultiplexing of the sequenced libraries was performed using bcl2fastq (v2.18.0.12). Mapping was performed using star aligner (v 2.5.2b), and the count matrix was produced using the featureCounts function from the subread package (v 1.5.2) using mouse annotation v GRCm38.87. *Foxp3*^{cre}-*Gclc*$^{fl/fl}$ and *Gclc*$^{fl/fl}$ mRNA data were analyzed using R statistical software (3.5.1) and DESeq2 (v 1.14.1) with default parameters to detect differential gene expression. We selected 1163 genes as having significant differences in expression based on a minimum log2 fold change of 0.58 and an adjusted p value < 0.05. Gene Set Enrichment Analysis on KEGG gene sets was performed using Bioconductor (v 3.7) and clusterProfiler (v 3.9.2). The Signaling Pathway Impact Analysis tool SPIA was used to identify activated or inhibited pathways.

QUANTIFICATION AND STATISTICAL ANALYSIS

Data are represented as the mean ± SEM and have at least n = 3 per group (refer to figure legend to detailed information), with p values determined by unpaired Student's t test or two-way ANOVA test using Prism 7.0 (GraphPad). P values were indicated with asterisks * and p values $\leq$0.05 were considered significant.

DATA AND CODE AVAILABILITY

The GEO accession number for the RNA-seq data from control and FoxP3-deficient Tregs file in this paper is GEO: GSE145311

nature microbiology

BRIEF COMMUNICATION

https://doi.org/10.1038/s41564-021-01046-z

Induction of robust cellular and humoral immunity against SARS-CoV-2 after a third dose of BNT162b2 vaccine in previously unresponsive older adults

Addi J. Romero-Olmedo[1,5], Axel Ronald Schulz[2,5], Svenja Hochstätter[3], Dennis Das Gupta[1], Iiris Virta[2], Heike Hirseland[2], Daniel Staudenraus[1], Bärbel Camara[1], Carina Münch[3], Véronique Hefter[3], Siddhesh Sapre[3], Verena Krähling[3], Helena Müller-Kräuter[3], Marek Widera[4], Henrik E. Mei[2,6], Christian Keller[3,6] and Michael Lohoff[1,6] ✉

Here we compared SARS-CoV-2-specific antibody and T-cell responses between older adults (>80 years old, *n* = 51) and a younger control group (20–53 years old, *n* = 46) after receiving two doses of BNT162b2. We found that responses in older adults were generally lower, and we identified 10% low-/non-responders. After receiving a third vaccination with BNT162b2, 4 out of 5 low-/non-responders showed antibody and T-cell responses similar to those of responders after two vaccinations.

Vaccination protects against fatal courses of SARS-CoV-2 infection, also in older adults[1,2]. Induction of neutralizing serum antibodies was observed after two intramuscular applications of the BNT162b2 mRNA COVID-19 vaccine in people >80 years of age[3]. However, recent outbreaks among older vaccinees[4] and antibody responses inferior to those observed in younger vaccinees[3] have prompted discussion on the necessity of a third vaccination.

Here we compared vaccine-induced humoral and cellular immune responses to SARS-CoV-2 in 51 individuals aged >80 years (older adults) and in 46 control individuals (young) (45 individuals aged 20–44 years (Table 1 and Supplementary Table 1) plus one 53-year-old woman, not included in the mean age calculation in Table 1, but included in all figures, accordingly. All participants were randomly recruited, COVID-19-naïve and not acutely ill; they were vaccinated twice, at day 0 and day 21, with BNT162b2 in a vaccination centre (older adults) or a doctor's practice (young) in Marburg, Germany, March–May 2021. Analysis of spike-specific IgG, neutralization capacity against SARS-CoV-2 and SARS-CoV-2-reactive CD4 T cells (positive for the markers CD40L and IFNγ) in peripheral blood revealed strong induction of humoral and cellular immunity in response to vaccination (Fig. 1a–c). Notably, the neutralization capacity after two BNT162b2 doses increased even against the delta variant (B.1.617.2), although reactivity towards the wild type (B.1) was higher (Fig. 1b). This finding confirms previous data on antibodies[3]. As for spike-specific CD4 T cells, our data vary from this report[3], as young and older groups demonstrated a further increase (10-fold average) between first and second dose (Fig. 1c, day 21 versus day 35). This was previously not noted[3], potentially due to the different method used for their quantification (FluoroSpot), as compared to the herein applied multi-parameter flow cytometry (Extended Data Fig. 1).

Several important differences were noted between young and old vaccinees' immune responses. First, the overall antibody and CD4 T-cell response was lower in older vaccinees at a high level of significance (Fig. 1a–c, day 35), as also shown by the stimulation index (Extended Data Fig. 2a). Second, while responses were comparable across young donors, substantial heterogeneity was observed in older donors, both in antibody and CD4 T-cell responses, whereby several older adults showed scarce or even no reaction. Third, some older adults had high frequencies of responding CD4 T cells before vaccination (Fig. 1c, day 0), probably reflecting cross-reactive activities gained during previous encounters with other coronaviruses, as demonstrated before[5,6].

By combining results for antibodies and CD4 T cells for each vaccinee (Fig. 2a,b), we identified five older adults retaining very low levels of specific serum IgG together with almost an absence of spike-reactive CD4 T cells (Fig. 2b, red triangles). Remarkably, these older adults were potentially not protected by the previous two doses of the vaccine. Among them, donor #31 received methotrexate for rheumatoid arthritis, while no history of immune modulating medication or disease was evident in the remaining four (Supplementary Table 1). Additionally, no evident difference between responders and low-/non-responders was identified by age and the Charlson comorbidity index (CCI; Extended Data Fig. 3a,b and Supplementary Table 1). Furthermore, there was no significant difference ($P = 0.15$ by Fisher's exact test) in the distribution of male and female participants between groups (Table 1).

No similar non-responder was found in the young cohort (Fig. 2a). Notably, our local authorities (Regional Council of Giessen, Hesse, Germany) informed us about breakthrough infections in several retirement homes. These infections occurred between 1 and 3 months after the second vaccination with BNT162b2 and 5 out of 45 infected residents >80 years succumbed to infection.

[1]Institute of Medical Microbiology and Hospital Hygiene, Philipps-University Marburg, Marburg, Germany. [2]Deutsches Rheumaforschungszentrum Berlin, Leibniz Institute, Berlin, Germany. [3]Institute of Virology, Philipps-University, Marburg, Germany. [4]Institute of Medical Virology, University Hospital, Goethe University, Frankfurt, Germany. [5]These authors contributed equally: Addi J. Romero-Olmedo and Axel Ronald Schulz. [6]These authors contributed equally: Henrik E. Mei, Christian Keller, Michael Lohoff. ✉e-mail: lohoff@med.uni-marburg.de

Table 1 | Donor characteristics

Group	Total donors	Sex	Age range	Age mean ± s.d.	Low-/non-responders, $n = 5$	Age range	Age mean ± s.d.
Older adults	$n = 51$	female: 31 (61%)	80–97 years	84.1 ± 3.8	female: 1 (20%)	81–95 years	85.2 ± 5.7
		male: 20 (39%)			male: 4 (80%)		
Young	$n = 46$	female: 29 (63%)	20–53 years	30.5 ± 5.9	female: 0	N/A	N/A
		male: 17 (37%)			male: 0		

N/A, not applicable.

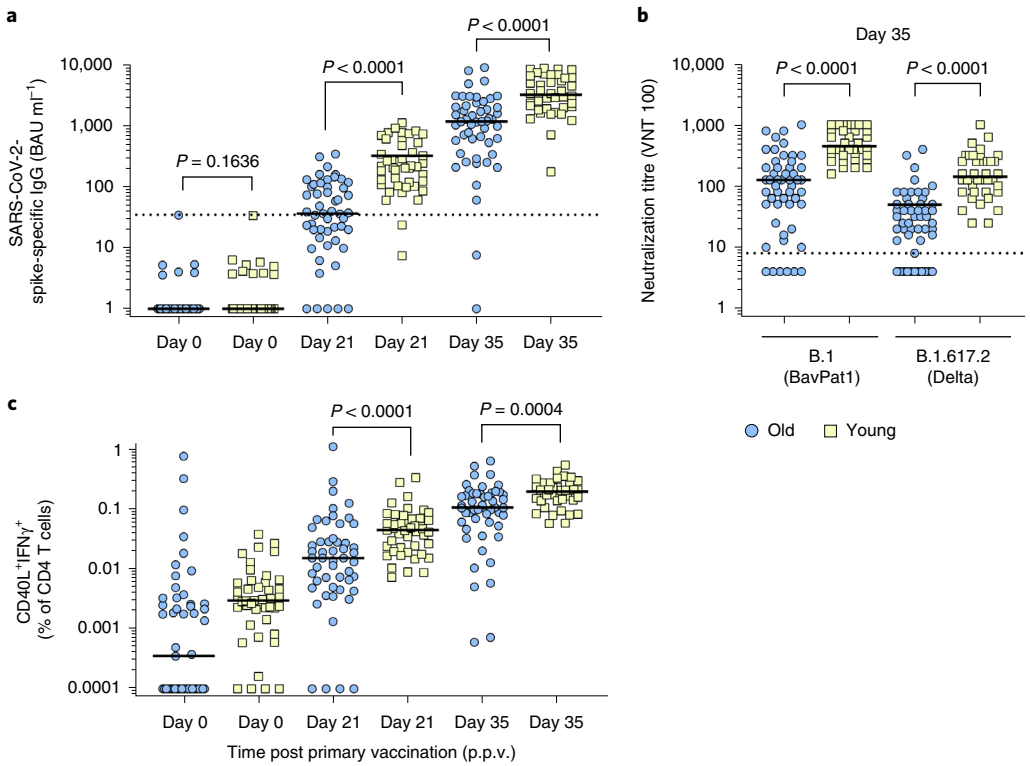

Fig. 1 | Humoral and cellular SARS-CoV-2 immunity in >80- and 20–53-year-old study participants vaccinated with the BNT162b2 vaccine. **a**–**c**, SARS-CoV-2-spike-specific serum IgG antibody titres (**a**), serum titres of 100% virus neutralization (VNT 100) for SARS-CoV-2 wild type (B.1) or its delta variant (B.617.2) (**b**) and percentages of SARS-CoV-2-spike-specific CD4 T cells (**c**) were analyzed in 51 donors aged >80 years (blue symbols) and 46 donors aged 20–53 years (yellow symbols) before (day 0; **a**,**c**), 21 d after the first (**a**,**c**) and 14 d after the second BNT162b2 (Pfizer-Biontech) vaccination (day 35; **a**–**c**). Each symbol represents one donor. Horizontal lines indicate medians, dotted lines indicate the cut-off for antibody positivity at 35.2 BAU ml^{-1} (**a**) and 8 (reciprocal titre) for VNT (**b**). A cut-off value for determining reactive T cells could be considered at 0.01% as shown previously[6] (**c**). *P* values determined by two-tailed Mann–Whitney test.

Thus, the lethality of these breakthrough infections is remarkably similar to the frequency of low-/non-responders in our older-adults study cohort. No COVID-19 infections were recorded in our cohorts until August 2021.

Aiming to enhance SARS-CoV-2 immunity, all 5 low-/non-responders received a third dose of the BNT162b2 mRNA vaccine during week 16 after the first dose. At that day, blood analyses demonstrated absence of specific immunity to SARS-CoV-2 (Fig. 2c–e). The third vaccination was well tolerated. Most importantly, 2 weeks later, 4 out of 5 vaccinees, including donor #31, demonstrated robust spike-specific T-cell and antibody responses comparable with those detectable in responders after two-dose vaccination (Fig. 2c–e and Extended Data Figs. 1 and 2b). In donor #54, a healthy man without obvious morbidities, SARS-CoV-2-specific immunity also increased, although only to low levels. He was meanwhile vaccinated a fourth time, again with BNT162b2, which unfortunately still yielded an insufficient response (46.97 BAU ml^{-1}).

Our data show that older adults initially hardly responding to two-dose vaccination can mount a virus-specific adaptive immune response after a third BNT162b2 dose. While the reason for primary unresponsiveness in our older-adults cohort remains unclear, BNT162b2 unresponsiveness in older adults is not fixed, and can be overcome by repeated vaccination. To confirm overall intact adaptive immune competence in low-/non-responders, we tested for antibody and CD4 T-cell reactivity towards control pathogens unrelated to SARS-CoV-2. Measles virus (MV)- or varicella-zoster virus (VZV)-specific IgG did not differ between low-/non-responsive donors and all other aged donors at baseline (day 0, Extended Data

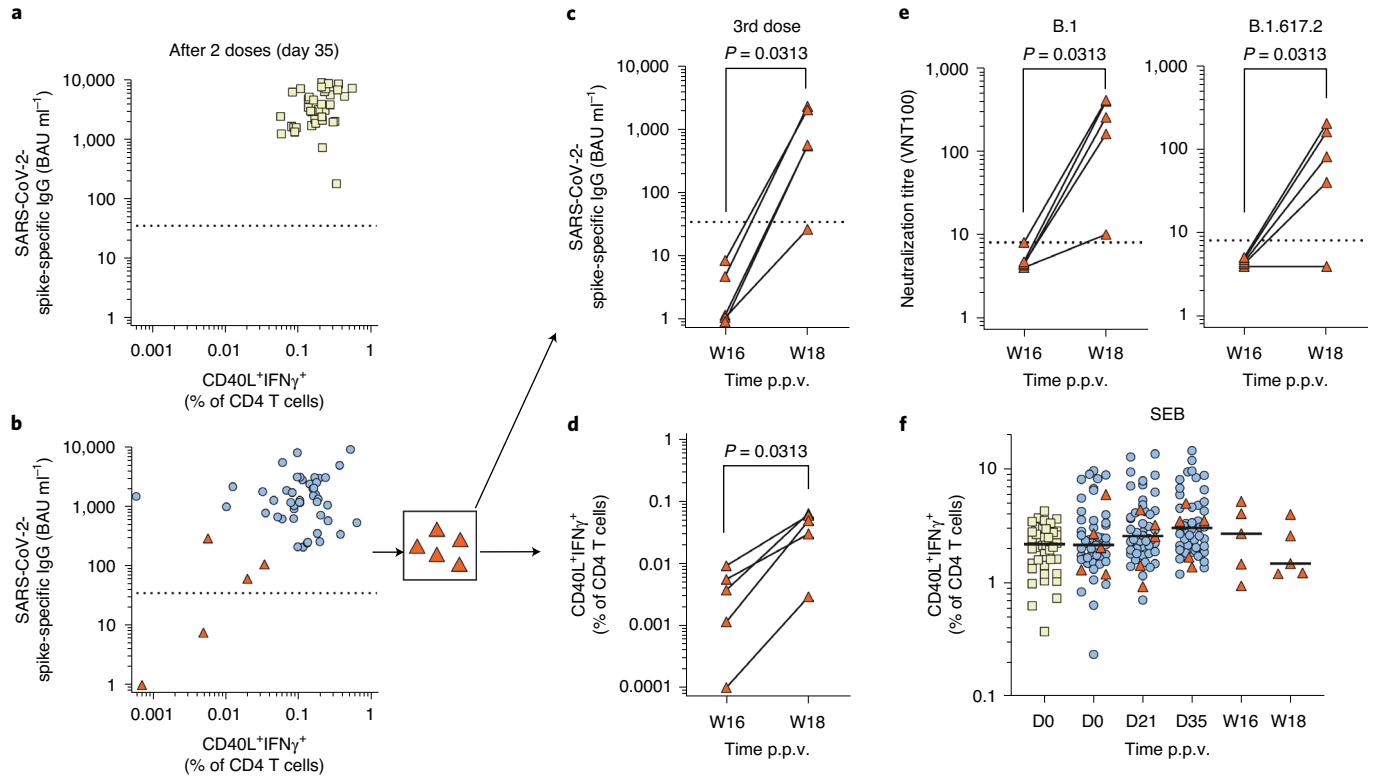

Fig. 2 | Humoral and cellular SARS-CoV-2 immunity in >80-year-old initial low-/non-responders is rescued after a third dose of the BNT162b2 mRNA vaccine. a–**e**, Combined presentation per person of the SARS-CoV-2-spike-specific serum IgG antibody and percentages of SARS-CoV-2-spike-specific CD4 T cells at day 35 in young (**a**) and aged donors (**b**). Five individuals (red triangles) mounted only low or no specific antibody and T-cell responses (**b**), and were vaccinated a third time in week 16 (W16) after the first dose (**c**–**e**). SARS-CoV-2-spike-specific serum IgG antibody titre (**c**), percentages of SARS-CoV-2-spike-specific CD4 T cells (**d**) and serum titre of 100% virus neutralization (VNT 100) for SARS-CoV-2 wild type (B.1) or its delta variant (B.1.617.2) (**e**) were measured in week 18 (W18). (**f**) T-cell response to SEB of the young and older participants measured at the indicated days or weeks after the first dose. Each dot, square and triangle represents one donor. Blue dots: aged responders; red triangles: initial low-/non-responders to the SARS-CoV-2 spike glycoprotein; yellow squares: young donors. Horizontal lines indicate medians, dotted lines indicate the cut-off for antibody positivity at 35.2 BAU ml^{-1} for SARS-CoV-2-spike-specific IgG (**a**,**c**) and 8 (reciprocal titre) for VNT (**e**). *P* values determined by one-tailed Wilcoxon matched-pairs signed-rank test (**c**–**e**).

Fig. 4). Additionally, the T-cell responsiveness towards staphylococcal enterotoxin B (SEB) was comparable to that seen in the other older vaccinees throughout the observation period (Fig. 2f and Extended Data Fig. 1). A similar response was observed in the young cohort (exemplified by their data on day 0), or in older adults (>80 years) who have recovered from COVID-19 infection several months before (Extended Data Fig. 1). These results demonstrate that the kinetics of T-cell activation in our assay conditions are similar throughout participants and evaluated timepoints. Furthermore, even if our cohort is small, we demonstrate that initial unresponsiveness to vaccination is not indicative of an overall lack of immune competence; consequently, older adults who previously did not respond or responded poorly to vaccination, will probably benefit from repeated vaccination with BNT162b2. Accordingly, in very recent studies of patients after allogeneic hematopoietic stem-cell transplantation or on haemodialysis, only a subgroup of vaccinees reacted by an increase in antibody levels after a third vaccination, while T-cell reactivity was not analysed[7,8]. A third vaccination was recently shown to increase protection against COVID-19 in people >60 years[9]. This effect probably combines overcoming of the herein described primary non-responsiveness, and a booster effect in primary responders whose antibody titre may have gradually declined.

Overall, we show lower immune responses against SARS-CoV-2 in aged versus young vaccinees, a finding which is also reflected in the antibody neutralization capacity against the SARS-CoV-2 delta variant. Nevertheless, 90% of individuals aged >80 years established adaptive SARS-CoV-2-specific immunity after receiving two doses of the BNT162b2 mRNA vaccine. However, low-/non-responders can be identified. Therefore, our data are suggestive of the importance of routine screening for spike-specific immunity in this population at risk, to assess the extent of immunity after two doses of BNT162b2. Screening should be unbiased and not limited to conditions of immunodeficiency or targeted immunosuppression. Should such tests reveal lack of specific immunity, re-vaccination should be considered.

Methods

Our research complies with all relevant ethical regulations. The study of patients with COVID-19 and vaccinations against COVID-19 was approved by the ethics committee of the medical faculty of the Philipps University Marburg (study number 40/21-12032021) and participants gave written informed consent according to the Consensus-based Clinical Case Reporting Guideline (CARE) guidelines and in compliance with the Declaration of Helsinki principles.

Study participants. Blood samples were obtained from older adults aged >80 years by venipuncture before and at additional timepoints indicated in Fig. 1 after primary and secondary vaccination by injection of Tozinameran (BNT162b2 vaccine, Comirnaty) in the deltoid muscle, at a vaccination centre in Marburg, Germany (Extended Data Table 1). On the basis of the lack of appropriate response to routine vaccination, the vaccination centre decided to vaccinate 5 individuals a third time with BNT162b2 vaccine 16 weeks after day 0, and blood samples were again obtained immediately before and 2 weeks after the third vaccination.

Analyses were performed between March and May 2021 and in August 2021 for third vaccination candidates. In May 2021 the study also obtained samples from unvaccinated elderlies >80 years of age living in a retirement home who have recovered from COVID-19 after an outbreak with SARS-CoV-2 variant B.1.221 in January 2021. All donors provided informed consent to participate in the study. Charlson comorbidity index[10] was calculated according to https://www.mdcalc.com/charlson-comorbidity-index-cci#evidence.

Sample processing and clinical lab. Blood serum was isolated from Serum Separator Clot Activator tubes (Greiner Bio-One, Germany) according to the manufacturer's instructions and stored at −80 °C until analysis.

Peripheral blood mononuclear cells (PBMCs) were isolated from fresh heparinized whole blood by density gradient centrifugation over Pancoll human (Pan Biotech) after dilution with an equal volume of PBS at room temperature. PBMCs were washed twice (500 × *g*, 10 min, 4 °C) in cold PBS supplemented with 0.2% BSA, counted manually, and resuspended in RPMI 1640 media (Gibco, Life Technologies) supplemented with penicillin, streptomycin and 10% human AB serum (all from Sigma) at 5×10^6 cells per ml.

Assessment of antigen-specific T cells. Antigen-reactive T-cell responses were analysed using a protocol based on previous work[11]. A detailed protocol is given in the Supplementary Information. Briefly, 5×10^6 PBMCs were stimulated with either SARS-CoV-2 spike protein peptide mix (wild type, Miltenyi Biotec), SEB (0.7 µg ml^{-1}, kindly provided by Prof. Bernhard Fleischer, Bernhard Nocht Institute of Tropical Medicine, Hamburg, Germany), or with an equal volume of water as a control, in the presence of anti-CD28 (5 µg ml^{-1}) and monensin (1 µg ml^{-1}) for 12 h. Brefeldin A (1 µg ml^{-1}) was added 2 h after the start of the stimulation. The stimulation was stopped by adding 2 nM EDTA. Dead-cell labelling was performed by resuspending the cell pellet in 500 µl PBS supplemented with 1:1,000 amine reactive Zombie Aqua Fixable Viability dye (Biolegend), and PBMCs were fixed for 20 min using 2% formaldehyde solution (Thermo Scientific). Thereafter, cells were stained with a cocktail of antibodies as detailed in the supplementary section. Acquisition was performed on a MACSQuant 16 flow cytometer (Miltenyi Biotec).

FlowJo version 10 (BD) and OMIQ.ai were used for analysing flow cytometry data. Flow cytometry standard files underwent quality control and, where applicable, anomaly removal by FlowAI[12].

Quantification of SARS-CoV-2-specific antibodies. Serum antibodies against the recombinantly expressed S1 subunit of the SARS-CoV-2 spike protein were quantified using the Anti-SARS-CoV-2-QuantiVac-ELISA run on the automated EuroLab Workstation (Euroimmun, Germany), following the manufacturer's protocol. Sera exceeding the detection range of the assay were pre-diluted 1:10 or 1:100 and measured again. Results obtained in relative units per ml were converted into binding antibody units (BAU) per ml by multiplication with the factor 3.2, according to the manufacturer's instructions. Results in BAU ml^{-1} were calibrated against the 'First WHO International Standard for anti-SARS-CoV-2 immunoglobulin (NIBSC code: 20/136)'. The lower cut-off for this assay is at 35.2 BAU ml^{-1}.

SARS-CoV-2 neutralization tests (VNT 100). Human sera were heat-inactivated for 30 min at 56 °C and diluted in a two-fold dilution series in 96-well cell culture plates (1:4 to 1:512). One hundred plaque-forming units (PFU) of SARS-CoV-2 were added in the same volume to the serum dilutions. The following SARS-CoV-2 virus isolates were used: German isolate BavPat1/2020; European Virus Archive Global #026 V-03883 (Genbank: MZ558051.1) and the Delta variant, B.1.617.2. The sequence of the viruses was confirmed. Following incubation at 37 °C for 1 h, approximately 20,000 Vero C1008 cells (ATCC, Cat. no. CRL-1586, RRID: CVCL_0574) were added. Plates were then incubated at 37 °C with 5% CO_2, and cytopathic effects were evaluated at day 4 or day 6 (Delta variant) post infection. Neutralization was defined as the absence of cytopathic effects in the serum dilutions. The reciprocal neutralization titre was calculated from the highest serum dilution without cytopathic effects as a geometric mean based on three replicates. The lower detection limit of the assay is 8 (reciprocal titre), corresponding to the first dilution of the respective serum. Two positive controls were used as inter-assay neutralization standards and quality control for each test. Neutralization assays were performed in the BSL-4 laboratory of the Institute of Virology at Philipps University Marburg, Germany.

Virus-specific antibodies. IgG antibodies against measles and VZV were quantified using the commercial Siemens Enzygnost IgG ELISA kit that was run on an automated Siemens BEPIII system. Values were quantified using the alpha method, according to the manufacturer's instructions. The cut-off for VZV-specific IgG was 50 mIU ml^{-1}, and 150 mIU ml^{-1} for measles-specific IgG.

Statistical analysis and reproducibility. Prism version 9 (GraphPad software) was used to display data, and perform descriptive statistics and significance testing.

To determine differences between the two cohorts (older adults vs young), a two-tailed Mann–Whitney test was applied to evaluate the level of significance. For assessing donor-specific responses over time (5 low-/non-responders), the one-tailed Wilcoxon matched-pairs signed-rank test was used. To test for differences in age, CCI and sex between responders and low-/non-responders, we applied the unpaired two-tailed *t*-test, the Wilcoxon rank-sum test with continuity correction and the Fisher's exact test, respectively. No statistical method was used to predetermine sample size.

Assessment of T cells after antigen-specific stimulation was performed in a total of 29 independent batches, with up to 30 donor samples per batch. Data of a SEB-stimulated control sample included in each batch showed consistent results across all batches. Quantification of SARS-CoV-2-specific antibodies was run according to clinical routine standards, including all required calibrators and controls. Data from 5 vaccinees were excluded, on the basis of their decision to decline study participation, death (not related to the study) or previous COVID-19 infection. Only age-group assignment was available to the investigators during experiments and outcome assessment. Moreover, the experiments and analyses were performed in three independent laboratories. The experiments were not randomized regarding age of the vaccinees.

Reporting Summary. Further information on research design is available in the Nature Research Reporting Summary linked to this article.

Data availability statement

The datasets generated and/or analysed during the current study are available from the corresponding author on reasonable request. Source data are provided with this paper.

Received: 13 September 2021; Accepted: 9 December 2021;
Published online: 10 January 2022

References

1. Haas, E. J. et al. Impact and effectiveness of mRNA BNT162b2 vaccine against SARS-CoV-2 infections and COVID-19 cases, hospitalisations, and deaths following a nationwide vaccination campaign in Israel: an observational study using national surveillance data. *Lancet* **397**, 1819–1829 (2021).
2. Polack, F. P. et al. Safety and efficacy of the BNT162b2 mRNA Covid-19 vaccine. *N. Engl. J. Med.* **383**, 2603–2615 (2020).
3. Collier, D. A. et al. Age-related immune response heterogeneity to SARS-CoV-2 vaccine BNT162b2. *Nature* **596**, 417–422 (2021).
4. Brosh-Nissimov, T. et al. BNT162b2 vaccine breakthrough: clinical characteristics of 152 fully-vaccinated hospitalized COVID-19 patients in Israel. *Clin. Microbiol. Infect.* https://doi.org/10.1016/j.cmi.2021.06.036 (2021).
5. Braun, J. et al. SARS-CoV-2-reactive T cells in healthy donors and patients with COVID-19. *Nature* **587**, 270–274 (2020).
6. Loyal, L. et al. Cross-reactive CD4+ T cells enhance SARS-CoV-2 immune responses upon infection and vaccination. *Science* https://doi.org/10.1126/science.abh1823 (2021).
7. Redjoul, R., Bouter, A. L., Parinet, V., Fourati, S. & Maury, S. Antibody response after third BNT162b2 dose in recipients of allogeneic HSCT. *Lancet Haematol.* https://doi.org/10.1016/s2352-3026(21)00274-x (2021).
8. Ducloux, D., Colladant, M., Chabannes, M., Yannaraki, M. & Courivaud, C. Humoral response after three doses of BNT162b2 mRNA COVID-19 vaccine in patients on hemodialysis. *Kidney Int.* **100**, 702–704 (2021).
9. Bar-On, Y. M. et al. Protection of BNT162b2 vaccine booster against Covid-19 in Israel. *N. Engl. J. Med.* **385**, 1393–1400 (2021).
10. Charlson, M., Szatrowski, T. P., Peterson, J. & Gold, J. Validation of a combined comorbidity index. *J. Clin. Epidemiol.* **47**, 1245–1251 (1994).
11. Schulz, A. R. et al. Low thymic activity and dendritic cell numbers are associated with the immune response to primary viral infection in elderly humans. *J. Immunol.* **195**, 4699–4711 (2015).
12. Monaco, G. et al. flowAI: automatic and interactive anomaly discerning tools for flow cytometry data. *Bioinformatics* **32**, 2473–2480 (2016).

Acknowledgements

This study was supported in part by grants from the Government of Hesse, Germany; the Else-Kroener-Fresenius-Stiftung, Germany; the Senate of Berlin; and the Deutsche Forschungsgemeinschaft (DFG), grant LO 396/8-1 to M.L. We thank the European Virus Archive Global (EVAg) for providing virus isolates used in this study (details in Methods); Prof. H.-R. Chung for providing help in statistical analysis; all participating donors; and the vaccination centre in Marburg, Germany, especially its Chief Manager K. Oerder, for excellent support throughout this study.

Author contributions

A.J.R.-O. and A.R.S. organized and performed experiments, and analysed data. A.J.R.-O., A.R.S., D.D.G., C.K. and S.H. created the figures. D.D.G., C.K., S.H. and V.H. collected blood. I.V. and H.H. performed flow cytometry analysis. D.S., B.C., A.J.R.-O. and S.H. prepared cells. S.H., C.M., C.K. and S.S. were involved in antibody analyses. V.K., H.M.-K. and M.W. performed virus neutralization assays. H.E.M., C.K. and M.L.

designed the study and recruited the study population. H.E.M., C.K., A.J.R.-O., A.R.S., D.D.G. and M.L. critically discussed the data. M.L. wrote the manuscript. H.E.M., C.K., A.J.R.-O. and A.R.S. revised the manuscript.

Competing interests

The funders had no role in the design or conduct of the study, or in the decision to submit the manuscript for publication. The authors declare no competing interests.

Additional information

Extended data is available for this paper at https://doi.org/10.1038/s41564-021-01046-z.

Supplementary information The online version contains supplementary material available at https://doi.org/10.1038/s41564-021-01046-z.

Correspondence and requests for materials should be addressed to Michael Lohoff.

Peer review information *Nature Microbiology* thanks Xiaowang Qu and the other, anonymous, reviewer(s) for their contribution to the peer review of this work.

Reprints and permissions information is available at www.nature.com/reprints.

Publisher's note Springer Nature remains neutral with regard to jurisdictional claims in published maps and institutional affiliations.

5 Morris DE, Cleary DW, Clarke SC. Secondary bacterial infections associated with influenza pandemics. *Front Microbiol* 2017; **8:** 1041.

Published **Online**
April 6, 2022
https://doi.org/10.1016/S1473-3099(22)00219-5

See **Online** for appendix

Dynamics of humoral and T-cell immunity after three BNT162b2 vaccinations in adults older than 80 years

A third mRNA-based booster vaccination is the currently favoured strategy to maintain protection against SARS-CoV-2 infection. Yet, significant waning of specific immunity within 6 months after two doses,[1] along with a higher incidence of breakthrough infections associated with the time elapsed since the second dose,[2,3] raise concerns regarding the durability of immunity also after the booster vaccination.

We compared the specific humoral and cellular responses (figure; appendix pp 10–13) after three versus two BNT162b2 (Pfizer-BioNTech) doses in a cohort of adults older than 80 years (median age 83 years [IQR 81–86]; appendix pp 3–4) at risk for severe COVID-19 and immune senescence. Our data demonstrate the induction of marginally higher spike S1-specific blood IgG concentrations 2 weeks after three than after two doses (appendix p 5). By contrast, functionally relevant receptor binding domain-specific IgG (figure A) and SARS-CoV-2-neutralising antibody (appendix p 5) titres were substantially increased after three compared with two doses, reflecting enhanced antibody production or affinity maturation.

By contrast, spike-specific CD4 T-cell frequencies reached similar levels after two and three doses (figure B; appendix p 5). After the respective acute response, frequencies returned to approximately pre-third vaccination levels, with no significant differences in the rate of decline after the second and third vaccinations (figure B; appendix p 6). Quantified cytoplasmic expression of the effector cytokine interferon γ (IFNγ) indicated functional enhancement of spike-specific T cells upon second but not further upon third vaccination, while more cytoplasmic IFNγ was found in spike-specific CD4 T cells from adults older than 80 years who had recovered from COVID-19 (appendix p 5). Thus, even a third BNT162b2 dose failed to induce durably enhanced quantities of spike-specific T cells and a functional quality reached after natural infection. Neither age nor comorbidities were significantly correlated with the observed immune response, perhaps due to the limited size of our cohort (appendix pp 7–9).

Concentrations of S1-specific IgG and neutralising antibodies also declined from the acute responses at weeks 5 and weeks 26, but at a lower rate and with an extended half-life after the third (week 40) compared with the second (week 24) dose (figure A; appendix pp 5–6), yielding more persistent, enhanced IgG quantity or quality after the third than after the second vaccination.

We conclude that a third dose of BNT162b2 in older adults, while establishing immunity in primary non-responders,[4] induces a durably escalated humoral response in the bulk of vaccinees for at least 3 months, indicating longer lasting humoral immunity. In a younger cohort, this boost also led to a strong increase of neutralising antibodies against the omicron (B.1.1.529) variant and protection from infection with the omicron variant.[5,6] Although neutralising antibody data for omicron are not yet available for our cohort, the strong rise in titres of neutralising antibodies against the BavPat1/2020 isolate used in our neutralisation assay (appendix p 5) suggests better neutralisation against omicron by the booster dose than for the second dose, as also demonstrated by others,[7] at least

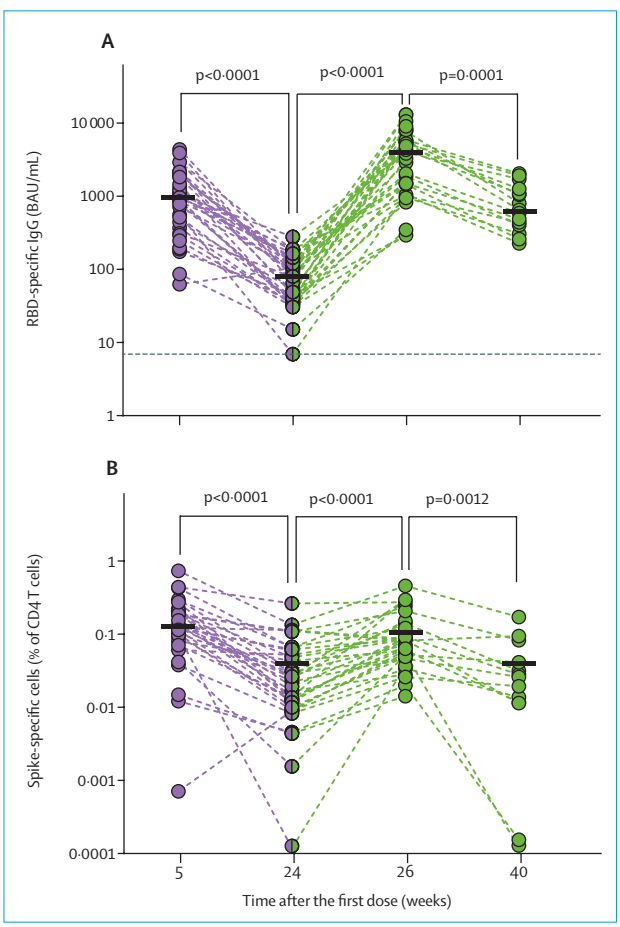

Figure: **Humoral and cellular SARS-CoV-2 immunity in donors older than 80 years after two and three doses of BNT162b2**
Immune response kinetics were followed in older adults in the course of vaccinations with BNT162b2 (second vaccination occurred 3 weeks and third vaccination occurred a median of 24 weeks [IQR 23–25] after first vaccination). Green indicates data related to the third dose of BNT162b2. Each symbol represents data of one donor at one timepoint. Horizontal lines indicate median values of datapoints in each column. p values were determined by two-tailed Wilcoxon matched-pairs signed rank test. (A) SARS-CoV-2 RBD-specific serum IgG levels; for weeks 5, 24, 26, and 40, number of participants was 35, 36, 34, and 15, respectively. The dotted horizontal line indicates the cutoff for antibody positivity at 7·1 BAU/mL. (B) Frequencies of SARS-CoV-2 spike-specific CD4 T cells identified as CD40 ligand-positive, interferon γ-positive CD4 T cells after overnight stimulation of peripheral blood mononuclear cells with SARS-CoV-2 spike peptides; for weeks 5, 24, 26, and 40, number of participants was 34, 35, 33, and 13, respectively. RBD=receptor-binding domain. BAU=binding antibody units.

in the short term. The level of T-cell immunity to SARS-CoV-2 in peripheral blood required for protection is still not established, although peripheral T cells induced by BNT162b2 apparently react well against the omicron variant.[8] As for our cohort, our data show two important aspects of a third compared with a second dose—namely, peak virus-specific T-cell frequencies were not further increased by a third dose, and average per-cell production of IFNγ remained unaltered and was still remarkably lower than in recovered donors of a similar age. Thus, at least in older adults, the durability and quality of vaccine-induced immunity should be considered in the recommendation of booster vaccinations, in addition to the severity of breakthrough SARS-CoV-2 infections caused by current and future viral mutants.

We declare no competing interests. This research was supported in part by grants from the Government of Hesse (Pandemie Netzwerk), Germany, by the Else-Kroener-Fresenius-Stiftung, Germany, by the Senate of Berlin, by the Deutsche Forschungsgemeinschaft (grant LO 396/8-1 to ML), and by the German Center for Infection Research, Section Emergency Vaccines (FKZ:8033801809 to VK). AJR-O and ARS contributed equally. HEM, CK, and ML contributed equally as senior authors.

*Addi J Romero-Olmedo, Axel Ronald Schulz, Svenja Hochstätter, Dennis Das Gupta, Heike Hirseland, Daniel Staudenraus, Bärbel Camara, Kirsten Volland, Véronique Hefter, Siddhesh Sapre, Verena Krähling, Helena Müller-Kräuter, Ho-Ryun Chung, Henrik E Mei, Christian Keller, *Michael Lohoff*

lohoff@med.uni-marburg.de

Institute of Medical Microbiology and Hospital Hygiene (AJR-O, DDG, DS, BC, ML), Institute of Virology (SH, KV, VH, SS, VK, HM-K, CK), and Institute of Medical Bioinformatics and Biostatistics (H-RC), Philipps-University Marburg, Marburg 35043, Germany; Deutsches Rheumaforschungszentrum Berlin, a Leibniz Institute, Berlin, Germany (ARS, HH, HEM); German Center for Infection Research, partner site Gießen–Marburg–Langen, Marburg, Germany (VK, HM-K)

1 Tober-Lau P, Schwarz T, Vanshylla K, et al. Long-term immunogenicity of BNT162b2 vaccination in older people and younger health-care workers. *Lancet Respir Med* 2021; **9:** e104–05.

2 Barda N, Dagan N, Cohen C, et al. Effectiveness of a third dose of the BNT162b2 mRNA COVID-19 vaccine for preventing severe outcomes in Israel: an observational study. *Lancet* 2021; **398:** 2093–100.

3 Bar-On YM, Goldberg Y, Mandel M, et al. Protection of BNT162b2 vaccine booster against COVID-19 in Israel. *N Engl J Med* 2021; **385:** 1393–400.

4 Romero-Olmedo AJ, Schulz AR, Hochstatter S, et al. Induction of robust cellular and humoral immunity against SARS-CoV-2 after a third dose of BNT162b2 vaccine in previously unresponsive older adults. *Nat Microbiol* 2022; **7:** 195–99.

5 Yu J, Collier AY, Rowe M, et al. Comparable neutralization of the SARS-CoV-2 omicron BA.1 and BA.2 variants. *medRxiv* 2022; published online Feb 7. https://doi.org/10.1101/2022.02.06.22270533 (preprint).

6 Tai CG, Maragakis LL, Connolly S, et al. Booster protection against omicron infection in a highly vaccinated cohort. *medRxiv* 2022; published online Feb 26. https://doi.org/10.1101/2022.02.24.22271347 (preprint).

7 Vanshylla K, Tober-Lau P, Gruell H, et al. Durability of omicron-neutralising serum activity after mRNA booster immunisation in older adults. *Lancet Infect Dis* 2022; **22:** 445–46.

8 Gao Y, Cai C, Grifoni A, et al. Ancestral SARS-CoV-2-specific T cells cross-recognize the omicron variant. *Nat Med* 2022; **28:** 472–76.

Antibody durability at 1 year after Sputnik V vaccination

Antibody waning against SARS-CoV-2 over time after vaccination, together with the emergence of new viral variants, pose great challenges for ending the pandemic. To our knowledge, no previous work has assessed the long-term prevalence of anti-SARS-CoV-2 antibodies in individuals vaccinated with Sputnik V (Gam-COVID-Vac).[1] We assessed the persistence of anti-spike IgG antibodies and their neutralising capacity against the original SARS-CoV-2 lineage (B.1) and a local isolate of the BA.1 lineage of the omicron (B.1.1.529) variant in a longitudinal cohort during 1 year after Sputnik V vaccination in Argentina.

We used 400 paired serum samples (100 samples at each timepoint, including at baseline before vaccination) from 100 volunteers who received two doses of Sputnik V that were obtained between Jan 1, 2021, and Jan 15, 2022. Participants with current or previous SARS-CoV-2 infection, determined by assessing seropositivity to nucleocapsid protein, were excluded from the analysis. The geometric mean (GM) of international units of IgG anti-spike antibodies[2] per mL (IU/mL) were 994 (95% CI 769–1285) at 42 days, 80 (60–106) at 180 days, and 36 (27–47) at 360 days after completion of the two-dose vaccination scheme (figure A; appendix p 2). Overall, a 27-fold reduction in IgG was observed 1 year after Sputnik V vaccination.

We assessed the GM half-maximal neutralising titre (GMT, IC_{50}) using a pseudotyped vescicular stomatitis virus carrying the spike of a viral isolate from Wuhan at the early stage of the pandemic (appendix p 4). The GMT at 42 days after vaccination was 133 (95% CI 92–193), at 180 days was 28 (19–39), and at 360 days was 11 (8–16; figure B).

Considering previous studies indicating that antibody responses undergo a maturation process,[3,4] we analysed the serum neutralising activity over time against the omicron variant. To this aim, we assessed the neutralising activity elicited by the Sputnik V vaccine[5] using the original B.1 isolate and a local isolate of BA.1 omicron. For this analysis, we used 60 samples (20 samples per timepoint) with the highest neutralising GMT for the original B.1 virus. For all timepoints analysed, we found a substantial decrease in the serum neutralising capacity against the omicron variant compared with the B.1 lineage (64-fold reduction at 42 days, 32-fold reduction at 180 days, and 28-fold reduction at 360 days after vaccination; appendix p 2). Six (30%) of the 20 immunised individuals remained positive for neutralising antibodies against omicron at 42 days after vaccination. This proportion increased to 45% (nine of 20) at 360 days. Similar results have been obtained using other vaccines

Published **Online** March 16, 2022 https://doi.org/10.1016/S1473-3099(22)00176-1

See **Online** for appendix